Primary Cu_6Sn_5 formation in soldering and its influence on the shear impact properties of solder joints

Zhenqi Li

Imperial College London

December 2017

Submitted in part fulfilment of the requirements for the degree of Doctors of Philosophy in Materials Science and Engineering at Imperial College London

Abstract

Intermetallic compounds (IMCs) play an important role in determining the reliability of solder joints in electronic systems. In lead free (Pb-free) solder joints such as Sn-0.7wt%Cu on Cu substrates, the as-soldered microstructure is a combination of the formation of interfacial Cu_6Sn_5 and Cu_3Sn layers, primary Cu_6Sn_5, and βSn during soldering. This thesis explores the evolution of Cu_6Sn_5 IMC in the microstructures of Sn-x wt%Cu / Cu joints (x = 0 – 2 wt% Cu) and their influence on the impact shear properties of solder joints.

Cu_6Sn_5 is the most common IMC in electronics and usually forms as a reaction layer and a primary phase during solidification of industrial Pb-free solder joints. In this thesis, the influence of the soldering process parameters i.e. peak soldering temperature, holding time at peak temperature and cooling rate on the volume fraction and morphology of primary Cu_6Sn_5 has been investigated in Sn-0.7wt%Cu/Cu joints. It is shown that with higher peak soldering temperature, longer holding time, and faster cooling rate, the Cu_6Sn_5 volume fraction increases and the morphology of primary Cu_6Sn_5 changes from faceted rods to non-faceted dendrites, undergoing an interface roughening process. Large primary Cu_6Sn_5 crystals are shown to grow from the interfacial Cu_6Sn_5 layer and grow to fill the whole joint. At high cooling rate and high peak temperature, primary Cu_6Sn_5 had a faceted to non-faceted transition with growth distance from the Cu_6Sn_5 layer which is discussed in terms of crystal growth into a negative temperature gradient. A quantitative study of copper substrate dissolution due to the diffusion of Cu into the liquid and the growth of IMC layers is used to discuss

the relative importance of these two factors. It is shown that the growth of IMC layers is the main contributor to Cu substrate dissolution when the peak temperature is low and when the liquid has become saturated in Cu.

The nucleation and growth of primary Cu_6Sn_5 has been explored by in-situ X-ray imaging at the SPring8 synchrotron for CP Sn/Cu, Sn-0.7wt%Cu/Cu, and Sn-2wt%Cu/Cu (with large and small initial primary Cu_6Sn_5 size) preform joints. No primary Cu_6Sn_5 was observed in CP Sn/Cu joint which is explained based on the Nernst-Brunner effect, while in Sn-0.7wt%Cu/Cu joint, although it is a hypoeutectic composition, the primary Cu_6Sn_5 nucleated and grew from both pre-existing Cu_6Sn_5 layer and in the bulk solder due to Cu substrate dissolution. In situ imaging confirmed that the size of primary Cu_6Sn_5 can be controlled by using a composition and peak temperature for which the primary Cu_6Sn_5 do not fully remelt. However, small primary Cu_6Sn_5 are shown to settle under gravity to the Cu_6Sn_5 layer at the bottom of the joint, while large primary Cu_6Sn_5 tend to remain in the bulk liquid.

Using the primary Cu_6Sn_5 size tailoring method, the influence of primary Cu_6Sn_5 size on shear impact properties is then studied while keeping all other microstructural features near constant. Using ball shear testing of ball grid array (BGA) joints, it is shown that larger primary Cu_6Sn_5 particles have a clear negative effect on the shear impact properties. Macroscopic fracture occurred by a combination of the brittle fracture of embedded primary Cu_6Sn_5 rods and ductile fracture of the βSn matrix. Cleavage of the Cu_6Sn_5 rods occurred mostly along (0001) or perpendicular to (0001) with some crack deflection between the two. The deterioration of shear impact

properties with increasing Cu_6Sn_5 size is attributed to (i) the larger microcracks introduced by the brittle fracture of larger embedded Cu_6Sn_5 crystals; and (ii) the less numerous and more widely spaced rods when Cu_6Sn_5 are larger which makes them poor strengtheners.

Table of Contents

Abstract 2

Declaration of originality 9

Copyright declaration 10

Acknowledgements 11

List of Tables 12

List of Figures 13

Chapter 1. Introduction 23

1.1 Introduction 23

1.2 Aim and objects 27

1.3 Thesis structure 28

Chapter 2. Literature review 29

2.1 The Cu_6Sn_5 phase 29

2.1.1 Crystallography of the Cu_6Sn_5 polymorphs 32

2.2 Nucleation 37

2.2.1 Homogeneous nucleation theory 37

2.2.2 Homogeneous nucleation rate 43

2.2.3 Heterogeneous nucleation theory 46

2.2.4 Prediction of potent heterogeneous nucleation sites 48

2.2.5 Nucleation of Cu_6Sn_5 during soldering.....49

2.3 Growth of Crystal in liquid.....57

2.3.1 The morphology of solid liquid interface (S-L) interface.....57

2.3.2 Growth of non-faceted S-L interfaceas.....59

2.3.3 Growth of faceted S-L interfaces.....60

2.3.4 Growth of interfacial intermetallic compounds during soldering.....62

2.3.5 Growth and morphology of primary Cu_6Sn_5 in liquid solder.....81

2.4 Role of intermetallic compounds in the fracture of solder joints.....86

2.4.1 Fracture classification and cleavage fracture.....86

2.4.2 Ductile tearing.....90

2.4.3 Fracture of primary Cu_6Sn_5 and its influence on the solder joints.....91

2.4.4 Fracture of primary Ag_3Sn and its influence on the solder joints.....100

Chapter 3. Influence of reflow process parameters on primary Cu_6Sn_5 morphologies 103

3.1 Introduction.....103

3.2 Experimental Methods.....103

3.2.1 Producing solder balls.....103

3.2.2 Reflow soldering.....104

3.2.3 Measurement of solder composition after reflow.....106

3.2.4 Microscopy.....106

3.3 Results and Discussion 108

3.3.1 Influence of holding time at peak reflow temperature 108

3.3.2 Influence of peak temperature 118

3.3.3 The morphologies of primary Cu_6Sn_5 122

3.3.4 Dependence of Cu_6Sn_5 morphology on Cu dissolution and cooling rate 125

3.4 Conclusions 135

Chapter 4. Real-time imaging of primary Cu_6Sn_5 evolution during the reflow soldering of Sn-xCu/Cu joints 137

4.1 Introduction 137

4.2 Experimental Methods 138

4.2.1 Sample preparation. 138

4.2.2 Synchrotron X-ray Imaging. 139

4.2.3 X-ray image processing 140

4.3 Results and Discussion 142

4.4 Conclusions 149

Chapter 5. The influence of primary Cu_6Sn_5 size on the shear impact properties of Sn-Cu/Cu BGA joints 151

5.1 Introduction 151

5.2 Experimental Methods 151

5.3 Results and Discussion 156

5.3.1 Undeformed microstructures 156

5.3.2 Impact shear properties 164

5.3.3 Deformed microstructures 168

5.4 Conclusions 176

Chapter 6 Conclusions and Future Work 178

6.1 Conclusions 178

6.2 Further Research 183

References 185

Declaration of originality

I, Zhenqi Li, hereby this thesis and associated research are my own work and that all sources I have used or quoted have been indicated and acknowledged by means of complete referencing. Permissions to reuse my own published work are granted from the publisher.

Parts of this thesis have been published in:

Li, Z.Q, S.A.Belyakov, J.W.Xian, C.M.Gourlay, The Influence of Primary Cu6Sn5 Size on the Shear Impact Properties of Sn-Cu/Cu BGA Joints. Journal of Electronic Materials, 2017

Copyright declaration

The copyright of this thesis rests with the author and is made available under a Creative Commons Attribution Non-Commercial No Derivatives licence. Researchers are free to copy, distribute or transmit the thesis on the condition that they attribute it, that they do not use it for commercial purposes and that they do not alter, transform or build upon it. For any reuse or redistribution, researchers must make clear to others the licence terms of this work.

Acknowledgements

I would like to give my deepest appreciate to my supervisor Dr. Christopher M. Gourlay for his invaluable supervision, great help and patient on my whole project especially during the hard time. I would like to express my deepest thanks to my family for their love and support of my studying and living in the UK.

I will also thank Prof. T.C.Lindley for valuable discussions, and my colleagues for their helps.

List of Tables

Table 1 summary of data of Sn 44

Table 2 summary of S-L interface stability in pure metal and alloy[70, 95].....59

Table 3 Reported growth exponent values for different alloy systems on Cu substrate 79

Table 4 different morphologies of primary Cu_6Sn_5. 82

Table 5. Growth directions of different morphologies primary Cu_6Sn_5 83

Table 6 The influence of trace elements and external reinforcement on IMCs size and morphology 84

Table 7. The composition of the as-cast alloy 104

Table 8. ICP tested mean compositions of bulk solder joints at five different holding time 110

Table 9 mean thickness of Cu pad dissolution, interfacial Cu6Sn5 layer, interfacial Cu3Sn layer and primary Cu6Sn5 area fraction 111

Table 10 parameters for Sn, Cu, Cu_6Sn_5 and Cu_3Sn.....116

Table 11 measurements of thicknesses of Cu_6Sn_5 and Cu_3Sn layer, area fraction of primary Cu_6Sn_5 and the thickness of Cu substrate dissolution. 118

List of Figures

Fig. 1 hierarchy inside iphone 4(a) Apple iphone 4 [5] (b) cross section view of ARM processor and RAM package of iphone 4 [6] (c) front and back of apple A4 chip [6] (d) solder joint (e) primary C_6Sn_5 (f) IMCs layer.....23

Fig. 2 Sn-Cu phase diagram by National Institute of Standards and Technology [51]30

Fig. 3 Sn-Cu phase diagram [52].....31

Fig. 4 Cu-Sn phase diagram [53].....32

Fig. 5 unit cell of high temperature η- Cu_6Sn_5 (generated in Crystal Maker) [54].....33

Fig. 6 Important planes, corresponding atomic locations and stacking sequences in η-Cu_6Sn_5 [11].....34

Fig. 7 unit cell of low temperature η′ - Cu_6Sn_5 (generated in Crystal Maker) [55] 35

Fig. 8. Gibbs Energy curves for solid and liquid around equilibrium melting point T_m 39

Fig. 9 free energy change and energy fluctuation during nucleation [70]. (a)-(c) are interface Gibbs energy, volumetric Gibbs energy and total Gibbs energy change of the system versus the radius r of the atom cluster at different temperature (d) is random addition of atoms onto the atom cluster.....41

Fig. 10 the homogeneous nucleation rate versus undercooling for βSn.....45

Fig. 11 Critical nuclei size r^* and the maximum size a nuclei can form r_{max} versus undercooling [71].....46

Fig. 12 model of heterogeneous nucleation: a spherical cap nucleates on the flat wall [71].....46

Fig. 13 Top views of interfacial Cu_6Sn_5 layer after fully etched Sn (a) on polycrystalline Cu substrate (b) on single crystalline (001) Cu [88].....49

Fig. 14 Morphologies of prism interfacial Cu_6Sn_5 on (001) single crystal Cu substrate at 260 ℃ for 60s (a), on (111) single Cu substrate at 260 ℃ for 60s (b) [89] 50

Fig. 15 schematic drawing of planner lattice match of $(010)Cu6Sn5\ with\ (001)Cu$ and $(010)Cu6Sn5\ with\ (111)Cu$ (Generated in Crystal Maker) [55].....52

Fig. 16 enlarged area of blue circle in Fig. 15. Blue represents Cu atoms on Cu_6Sn_5 while red represents Cu atoms on Cu. (generated in Crystal Maker) 52

Fig. 17 in-situ observation of soldering reaction of Sn-0.7wt%Cu paste/Cu at (a) 0 s, (b) 10 s, (c) 11 s, (d)112 s, (e) 118 s, (f) 123 s, (g) 130 s, and (i) 143s [91].....54

Fig. 18 image sequences of the formation of primary Cu_6Sn_5 in SAC305/Cu joint from synchrotron radiography (modified from [27]).....55

Fig. 19 Backscatter images of Cu_xAl_y with increasing growth distance in (a)-(d) in Sn-4Cu-0.2Al where the primary Cu_6Sn_5 were attached on. (e) Cu_6Sn_5 grew on $Cu_{33}Al_{17}$. [13].....55

Fig. 20 (a)(c) Schematic representation of OR1 and OR2 between Cu_6Sn_5 and βSn. (b)(d) Planar lattice match for OR1 and OR2 [92]. 56

Fig. 21 (a) faceted interface and (b) non-faceted interface [70] 58

Fig. 22 different positions that liquid atoms can join on the S-L interface of a cubic crystal [95] 60

Fig. 23 the defects for faceted crystals (a) screw dislocation (b) twining (c) twisted boundary [95].....61

Fig. 24 (a) whole Sn-Cu phase diagram [51] (b) Sn rich part data from Thermo-Calc [97].....62

Fig. 25 general interfacial reactions during soldering between Sn-xCu solder and Cu substrate (modified from [109]).....65

Fig.26 Schematic drawing of an ith Cu_6Sn_5 grain and a mean size Cu_6Sn_5 grain on the interface, and the concentration gradient between them [86]. 66

Fig. 27 effect of different curvature undercoolings on the corresponding composition at isothermal reaction temperature.....70

Fig. 28 dendrites formed during directional solidification (left), neighboring secondary arms in the white box and composition gradient between them [83]. 71

Fig. 29. Schematic representation of equiaxed Cu_6Sn_5 scallop [106].....75

Fig. 30 schematic drawing of how to calculate f, the fraction of available grain boundary area for grain boundary diffusion 76

Fig. 31 different primary Cu_6Sn_5 morphologies in 2D and 3D (a) hexagonal rods [49] (b) grooved rod [11] (c) in-plane branched facets [11] (d) 'v'-shape [124] (e) dendrite [11] (f) 'I'-shape, 'bird'-shape [20] (g) 'X'-shape [125] (H) 'H'-shape [124] (I) 'Y'-shape [13].....82

Fig. 32 Different types of fracture [129].....87

Fig. 33 infinite plate under remote tensile stress, containing through thickness crack [134].....88

Fig. 34 stress elements around crack tip [134] 89

Fig. 35 schematic drawing of stress propagation by ductile tearing [138] 91

Fig. 36 the primary Cu6Sn5 rod, with hollow rod morphology in 60Sn-40Pb/joint [50] 92

Fig. 37 (a) stress-strain curves for 60Sn-40Pb with and without intermetallics at -196,20,125℃. SEM fractographs of 60Sn-40Pb with intermetallics at (b)-196℃ (c) 20℃ and (d)125℃ (modified from [50]).....93

Fig. 38 (a) stress-strain curves of Cu_6Sn_5 single crystals, showing the strain bursts (b-c) top view and side view of cleavage fractured Cu_6Sn_5, corresponding to the strain bursts. (d) schematically presenting the nanoindentation process according to the stress-strain curve [139]. 94

Fig. 39 The stress-strain curve from nanoindentation and corresponding in-situ SEM micrographs [140]. 95

Fig. 40 (a) micropillar compression stress-strain curve of single Cu_6Sn_5 (b) before test (c) after failure [141].....96

Fig. 41 (a) SEM micrograph of slip trace appeared during micropillar compression (b) FIB cross section view of the Cu_6Sn_5 pillar [141]. 96

Fig. 42 Fracture strength, fracture strain and Young's modulus versus misorientation to c-axis [140] 97

Fig. 43 Comparison of mechanical properties versus misorientation angle from c-axis of Cu_6Sn_5 crystal (modified from [142]). 98

Fig. 44 (a) primary crack formed perpendicular to c-axis 30mN (b) secondary crack formed parallel to c-axis 40mN [143].....98

Fig. 45 tensile test with increased deformation (a) 0% (b) 4.6% (c) 11.5% and (d) 16.9% [144].....99

Fig. 46 large Ag_3Sn blades in Sn3.9Ag0.6Cu/Cu joint [49].....100

Fig. 47 The crack propagation routes on the interface between Ag_3Sn and Sn matrix (modified from [49]).....101

Fig. 48 decohesion at the interface boundary between Ag_3Sn blades and βSn during (a) thermal cycling [145] and (b) during three point bending test [149].....101

Fig. 49 (a) typical reflow profile (b) Cooling parts of reflow profiles 105

Fig. 50 (a) Variation of Cu content in bulk solder joint after aging for different times at 300°C. Datapoints are ICP-AES measurements. (b) Partial Sn-Cu phase diagram at the Sn rich part [97]. 109

Fig. 51(a)-(d) solder joints that were held at 300°C for 10s, 30s, 5min and 30min before being cooled at ~30 K/s. Top row: full cross-sections showing primary Cu_6Sn_5. Middle row: Cu_6Sn_5 layers after deep etching. Bottom row: dissolved Cu substrate. 110

Fig. 52 (a) Blue data point: area fraction of primary Cu_6Sn_5 in solder joints held at 300°C for 10s, 30s, 1min, 2min, 5min and 30min. Red data point: volume fraction of primary Cu_6Sn_5 calculated from equilibrium phase diagram with the compositions measured by ICP-AES and were shown in Table 8. (b) IMC layer thickness versus the square root of aging time. 112

Fig. 53 Schematic diagram of the key features BGA soldering 112

Fig. 54 Cu mass gained in each of IMCs and Cu mass lost from Cu pad with time .117

Fig. 55 (a)-(e) solder joints that were held for five minutes at 240°C, 270°C, 300°C, 350°C and 390°C before being cooled at ~2.6 K/s. Top row: full cross-sections showing primary Cu_6Sn_5. Middle row: Cu_6Sn_5 layers after deep etching. Bottom row: dissolved Cu substrate.....118

Fig. 56 (a) Measured area fraction of primary Cu_6Sn_5 versus peak temperature (black cross) compared with predictions of the volume fraction of primary Cu_6Sn_5 versus peak

temperature for three values of βSn nucleation undercooling (coloured curves). (b) Sn-Cu phase diagram from ref [97] indicating the saturated liquid compositions for the five peak temperatures (c) Mass fraction of primary Cu_6Sn_5 as a function of temperature for uniformly saturated liquid cooled from the five peak temperatures (calculated using ref [97])....120

Fig. 57 Cu mass gained in the Cu_3Sn layer (green), Cu_6Sn_5 layer (brown) and primary Cu_6Sn_5 (pink), along with the Cu mass lost from the Cu pad versus time. Black crosses are from the measured thickness of dissolved Cu. Blue data are the sum of the mass lost to the Cu_3Sn layer, Cu_6Sn_5 layer and primary Cu_6Sn_5 121

Fig. 58 typical micrographs of primary Cu6Sn5 from shallow etched Sn-0.7wt%Cu/Cu solder joints. (a) hexagonal rod (b) grooved rod (c) in-plane branched and (d) dendrite 124

Fig. 59 (a)-(d) typical 2D optical micrographs of Sn-0.7wt%Cu/Cu solder joints held at 300°C for 10s, 30s, 5min and 30min and secondary election images of primary Cu6Sn5 with typical features corresponding to each holding time. 126

Fig. 60 (a) typical cross section of a solder joint which has been held at 300°C for 5min within which Sn has been fully etched off (b) a typical large primary Cu_6Sn_5 grown from the layer. 128

Fig. 61 description of primary Cu_6Sn_5 morphology transformation from hexagonal rod to dendrite. 130

Fig. 62 (a)-(e) solder joints that were held for five minutes at 240°C, 270°C, 300°C, 350°C and 390°C before being cooled at ~2.6 K/s. Left side: full cross-sections showing primary Cu_6Sn_5. Right side: the typical 3D morphology of primary Cu_6Sn_5 after deep etching. 131

Fig. 63 morphologies of primary Cu_6Sn_5 cooling at (a) ~0.67K/s (b) ~2.6K/s (c) ~30K/s after holding for 5 min at five different peak temperatures. Each column represents same peak temperature, and micrographs in each row share the same scale bar.....132

Fig. 64 primary Cu_6Sn_5 morphology map. Black data points: primary Cu_6Sn_5 in large free standing samples [11]. Red data points: primary Cu_6Sn_5 in ~500μm Sn-0.7wt%Cu/Cu solder joints. 133

Fig. 65: Schematic diagram of in situ soldering specimen cell. (a) fluxed solder foil on a Cu substrate. (b) Individual parts of the sample cell. (c) Assembled parts of the sample cell. Note that the image is not to scale. 138

Fig. 66 schematic drawing of synchrotron hutch with apparatus [12].....139

Fig. 67 selected image (frame 600) from image sequences of Sn-2wt%Cu/Cu with small primary Cu_6Sn_5, showing (a) after flatfield correction (b) flatfield corrected image after Gaussian blurred (c) normalized image 141

Fig. 68 (a) Thermal profile of soldering CP Sn onto Cu substrate, dashed line indicates melting temperature of pure Sn 232℃. Typical frames were selected from synchrotron radiography of 1 frame per second (b) frame 340 (c) frame 400 (d) frame 439 (e) frame 520.....143

Fig. 69(a) Thermal profile of soldering Sn-0.7Cu onto Cu substrate, dashed line indicates the eutectic temperature 227 ℃. Typical frames were selected from synchrotron radiography of 1 frame per second (b) frame 382 (c) frame 440 (d) frame 487(e) frame 498 (f) frame 520. (black arrow: primary Cu_6Sn_5 nucleated in the bulk solder, red arrows: primary Cu_6Sn_5 grew from pre-existing interfacial Cu_6Sn_5 crystals) 144

Fig. 70 (a) Thermal profile of soldering Sn-2wt%Cu containing small primary Cu_6Sn_5 onto Cu substrate, dashed line indicates the eutectic temperature 227℃. Typical frames

were selected from synchrotron radiography of 1 frame per second (b) frame 330 (c) frame 379 (d) frame 403 (e) frame 470 (f) frame 528 (g) frame 590. (black arrow: primary Cu_6Sn_5 nucleated in the bulk solder).....146

Fig. 71 (a) Thermal profile of soldering Sn-2wt%Cu containing large primary Cu_6Sn_5 onto Cu substrate, dashed line indicates the eutectic temperature 227℃. Typical frames were selected from synchrotron radiography of 1 frame per second (b) frame 195 (c) frame 280 (d) frame 316 (e) frame. (black arrow: primary Cu_6Sn_5 pre-existed in solder foil, red arrows: primary Cu_6Sn_5 nucleated and grew in the bulk solder). 147

Fig. 72 cross section of Sn-2wt%Cu/Cu containing manipulated large primary Cu_6Sn_5 148

Fig. 73 (a) Thermal profile used for reflow soldering. (b) Sn-Cu phase diagram [42] highlighting the initial solder composition and the peak reflow temperature (c) Mass fraction of primary Cu_6Sn_5 as a function of temperature in Sn-2Cu [42].....153

Fig. 74 Set up of shear impact testing on a DAGE4000.....155

Fig. 75 Overview of primary Cu_6Sn_5 in Sn-2Cu/Cu joints made with four sizes of primary Cu_6Sn_5, with increasing size of primary Cu6Sn5 from (a) to (d). The first and second columns are EBSD IPF-y maps and BSE-SEM images. The third and fourth columns are deep etched SE-SEM images of the primary Cu_6Sn_5 at two magnifications. Each column has a common scale bar. 157

Fig. 76 Summary of microstructural measurements for each batch of Sn-2Cu/Cu joints. Bars are mean values, error bars are standard deviations. (a) Number of primary Cu6Sn5 per unit area. (b) Number of eutectic Cu6Sn5 particles per unit area, and number of βSn orientations per joint. (c)-(f) typical BS-SEM micrographs used to count eutectic Cu_6Sn_5 number in joints with increasing size of primary Cu_6Sn_5.....158

Fig. 77 Overview of βSn in Sn-2Cu/Cu joints, with increasing size of primary Cu6Sn5 from (a) to (d). The first column are EBSD IPF-y maps of typical joints. The middle column are {001} pole figures made by combining ≥4 EBSD maps for each microstructure condition. The third column are misorientation (MO) histograms, compiled from ≥4 joints for each microstructure condition. Mackenzie curves are superimposed on the MO distributions 160

Fig. 78 Interfacial Cu_6Sn_5 in solder joints with increasing primary Cu_6Sn_5 size from (a)-(d) prior shear impact test 163

Fig. 79 Typical force-displacement curves from shear impact testing, with increasing size of primary Cu6Sn5 from (a) to (d). 164

Fig. 80 Impact shear properties (maximum force and energy absorbed) of Sn-2wt%Cu/Cu with different size of primary Cu_6Sn_5. 165

Fig. 81 (a) Width of fractured primary Cu_6Sn_5 on fracture surfaces for each microstructure condition. Bars are mean values, error bars are standard deviations. (b) The same data summarised in box plots. (c) Maximum force versus the width of fractured primary Cu_6Sn_5. (d) Energy absorbed versus the width of fractured primary Cu_6Sn_5. (e) Maximum force versus the number density of primary Cu_6Sn_5. (f) Energy absorbed versus the number density of primary Cu_6Sn_5..... 166

Fig. 82 Cross sections of fractured joints, with increasing size of primary Cu6Sn5 from top to bottom. (a)-(d) typical examples of the whole cross-section. (e)-(h): higher magnification images of primary Cu_6Sn_5 on and beneath the fracture surfaces..... 168

Fig. 83 Shear impact test interrupted at ~150μm. (a) BSE-SEM image of a cross-section. (b) EBSD IPF-y map of the same cross-section. (c)-(e) examples of decohesion between Cu_6Sn_5 and the βSn matrix, brittle fracture of primary Cu_6Sn_5, and the propagation of microcracks into the βSn. 170

Fig. 84 Fracture surfaces of solder joints from batches with increasing size of primary Cu6Sn5 from (a) to (d). Typical examples of the varying Cu_6Sn_5 size are given in (e)-(h). (i)-(k) show typical features found at different locations of the fracture surfaces: (i) brittle fractured primary Cu_6Sn_5 at the 'front part' of the surface near to the initial hammer impact, (j)-(k) primary Cu_6Sn_5 fragments at the 'bottom part' of the surface. 172

Fig. 85 (a)-(b) Typical Cu_6Sn_5 brittle fracture surfaces that are close to the plane of the macroscopic fracture surface. (c) EBSD IPF-z map of 11 Cu_6Sn_5 fracture surfaces from different samples compiled into a single map. (d) hexagonal IPF colour scale. (e) IPF-z for the 11 Cu_6Sn_5 crystals in (c). (f) and (g) examples of crack deflection from basal to prism fracture paths. 174

Fig. 86 deflected fracture path in primary Cu_6Sn_5 in Sn-2wt%Cu during shear impact testing.....184

Chapter 1. Introduction

1.1 Introduction

In the electronics manufacturing industry e.g. mobile phones and computers, soldering is the most common process used to join two metallic conductors together by reflowing and solidifying a lower melting temperature solder between them. Traditional electronics solder alloys were based on tin (Sn) and lead (Pb). However, from 2006, Pb containing solder alloys have been banned in the European Union by the Restriction of Hazardous Substances directive (RoHS) [1, 2] , because Pb is hazardous to human health and can introduce serious environmental problems [3, 4].

An example of solder joints in an electronic product is shown in the hierarchy inside an iphone 4 mobile phone in Fig. 1.

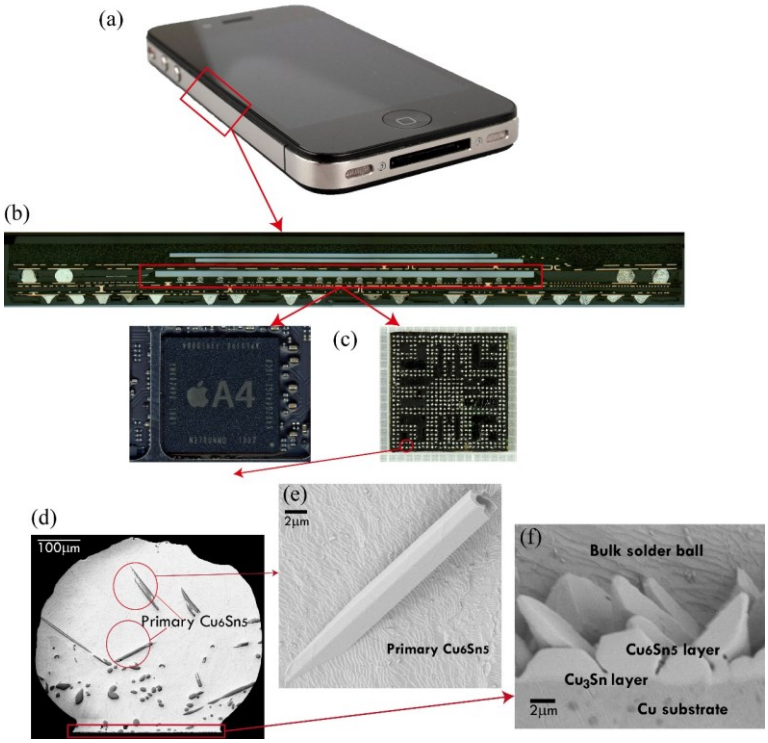


Fig. 1 hierarchy inside iphone 4(a) Apple iphone 4 [5] (b) cross section view of ARM processor and RAM package of iphone 4 [6] (c) front and back of apple A4 chip [6] (d) solder joint (e) primary C_6Sn_5 (f) IMCs layer

Fig. 1 (b) shows the processor in the centre interconnected to a printed circuit board (PCB) with solder joints. The solder joints connect copper tracks that are clearly visible from their reflectivity and colour. Fig. 1 (c) shows the front and back sides of the A4 chip used in the iphone, where the shining dots on the back side of the chip are solder joints used to adhere the chip to the PCB and conduct electricity. Fig. 1 (d) is the cross section of one solder joint containing primary Cu_6Sn_5 in the bulk solder, Fig. 1(e), and a Cu_6Sn_5 layer at the interface between the Cu and solder, Fig. 1(f).

Cu_6Sn_5 is a common intermetallic compound (IMC) in most Pb-free solders, which can form both in the bulk solder and as a reaction layer between the bulk solder and the copper substrate. Due to the increasing demand to minimize the size of solder joints, the volume fraction (vol%) of IMCs is increasing [7, 8]. For example, ball grid array (BGA) solder joints typically have up to ~2 vol% of primary Cu_6Sn_5 crystals in the bulk after solidification and Cu_6Sn_5 rods can span nearly the entire diameter of the ball [9, 10]. As the joint size decreases, the fraction of Cu_6Sn_5 increases until, in 10-30 μm microbumps, the entire joint can become Cu_6Sn_5. Therefore, Cu_6Sn_5 is increasingly important to the reliability of electronic devices since solder joints are one of the weakest parts of an electronic system, e.g. during drop impacts or thermo-mechanical fatigue etc. To optimise joints containing a higher volume fraction of Cu_6Sn_5, it is necessary to deepen the understanding of the factors that control the morphology and size of Cu_6Sn_5 and to understand how these microstructural features affect solder joint reliability.

A large body of research has focused on the morphology development of the

interfacial Cu_6Sn_5 reaction layer for different thermal histories. Many fewer studies have focused on the formation of primary Cu_6Sn_5 in the bulk solder. Those studies that have been performed have either been fundamental studies on the Cu_6Sn_5 growth transition from faceted rods to nonfaceted dendrites [11]; or have studied the role of trace element additions including Al [9, 12, 13], Zn and Ni [14-19], and La [20]; or have explored the influence of reinforcements e.g. SiC [21-23]，Al_2O_3 [24], and TiO2 [25, 26] on the Cu_6Sn_5 microstructure. However, it is also important and necessary to gain a deeper understanding about the influence of reflow process parameters on the size and morphology of primary Cu_6Sn_5 i.e. peak reflow soldering temperature, the holding time at that peak temperature and the cooling rate.

In recent years, there have been major developments in the real time *in situ* synchrotron X-ray radiography of alloy solidification [27-35] that enable investigations of the dynamic development microstructure and the detailed quantitification of kinetics. These synchrotron imaging approaches have been applied recently to solder solidification of primary Cu_6Sn_5 during soldering [27]. There is now an opportunity to use real time *in situ* synchrotron X-ray radiography to gain deeper insights into primary Cu_6Sn_5 development as a function of process parameters and other variables.

A large body of research has considered how the interfacial Cu_6Sn_5 reaction layer [36-39] affects the performance of solder joints where it has been found that, if fracture occurs through the Cu_6Sn_5 layer, the thickness influences the fracture toughness and generally the thicker the interfacial layer, the lower the fracture toughness [40-48]. However, much less research has explored the role of primary Cu_6Sn_5 crystals on solder

joint performance and has generally focused on the role of primary Cu_6Sn_5 in tensile fracture. For primary Cu_6Sn_5 with long rod morphology some researchers have reported no apparent influence on the mechanical properties [43, 49], while other research reported the its influence depends on the temperature [50]. Therefore, it is needed to research how the size of primary Cu_6Sn_5 influences the mechanical behaviour to understand the optimum primary Cu_6Sn_5 size and morphology to improve the reliability of solder joints.

To address the demands pointed out above, this thesis focuses on the (i) the influence of solder process parameters on the primary Cu_6Sn_5 morphology and volume fraction (ii) *in situ* real time imaging of the influence of Cu content and pre-existing primary Cu_6Sn_5 on solder joint microstructure formation, and (iii) the influence of primary Cu_6Sn_5 size on the shear impact properties of BGA solder joints.

1.2 Aim and objects

The aim of this work is to achieve a deeper understanding of the formation of primary Cu_6Sn_5, and to explore the influence of primary Cu_6Sn_5 size on the shear impact properties of ball grid array solder joints.

These aims led to the following objectives:

(1) Understand the influence of soldering process parameters i.e. peak reflow temperature, holding time under peak temperature and cooling rate on the morphology and volume fraction of primary Cu_6Sn_5 and the amount of interfacial Cu_6Sn_5 formed.

(2) Investigate the relationship between Cu dissolution from the Cu substrate and the Cu gained by interfacial IMCs layer and primary Cu_6Sn_5 during reflow soldering.

(3) Dynamically observe the formation of Cu_6Sn_5 during soldering of various Sn-Cu solders on Cu substrates by in-situ real time synchrotron radiography to explore the effect of Cu content and Cu_6Sn_5 size on microstructure development.

(4) Develop a method to manipulate the mean primary Cu_6Sn_5 size in solder alloys and solder joints while keeping other microstructure features (βSn and eutectic) near constant to enable a study of primary Cu_6Sn_5 size on mechanical performance.

(5) Use the method developed in objective (4) and conduct ball shear testing on BGAs to investigate the influence of primary Cu_6Sn_5 size on the impact shear properties of BGA joints.

The objectives above are approached with the following experimental characterization techniques: imaging by optical microscopy and scanning electron microscopy, electron backscatter diffraction (EBSD), synchrotron radiography, and ball shear testing

1.3 Thesis structure

Chapter 2 is a literature review overviewing the background theories and published papers about Cu_6Sn_5, with a focus on Cu_6Sn_5 nucleation, growth of Cu_6Sn_5 crystals in liquid, and the fracture of brittle and ductile crystals.

Chapter 3 investigates the influence of reflow soldering process parameters i.e. peak soldering temperature, holding time under peak temperature and cooling rate on the morphology of primary Cu_6Sn_5 in solder joints.

Chapter 4 is a real time X-ray observation study of primary Cu_6Sn_5 formation in solder joints by in situ synchrotron radiography. This Chapter also details the development of a method to manipulate the primary Cu_6Sn_5 size in solder joints.

Chapter 5 involves manipulating the primary Cu_6Sn_5 size in BGA joints while keeping other microstructures near constant and investigating the influence of primary Cu_6Sn_5 size on the impact shear properties using ball shear of BGAs.

Chapter 6 concludes on the main findings of the whole work and suggests future research directions.

Chapter 2. Literature review

2.1 The Cu_6Sn_5 phase

The most common solder alloys used in the electronics industry are Sn-rich alloys soldered onto Cu substrates. The peak reflow soldering temperature is typically in the range ~230-300℃ and solder joints can be expected to operate at -70 to 120 °C. From the phase diagram in Fig. 2 [51], the corresponding stable phases are βSn, high temperature Cu_6Sn_5 phase (η- Cu_6Sn_5), low temperature Cu_6Sn_5 phase (η′- Cu_6Sn_5) and Cu_3Sn. βSn usually occupies the largest volume fraction of as-soldered joint due to the shape of the phase diagram; Cu_6Sn_5 can form both a layer at the interface between the solder and Cu substrate, large crystals in the bulk solder as a primary solidification phase [27], and smaller eutectic particles in the βSn matrix; and Cu_3Sn usually appears as a thin layer between Cu_6Sn_5 layer and the Cu substrate during soldering or subsequent solid state aging. Primary Cu_6Sn_5 will form for most solder alloys soldered onto Cu substrates, due to the dissolution of Cu into the solder which will increase the liquid composition into the hypereutectic region (the primary Cu_6Sn_5 phase field). The eutectic point is ~0.89wt%Cu and 227℃, so the eutectic mixture contains ~98% βSn and only ~2% Cu_6Sn_5.

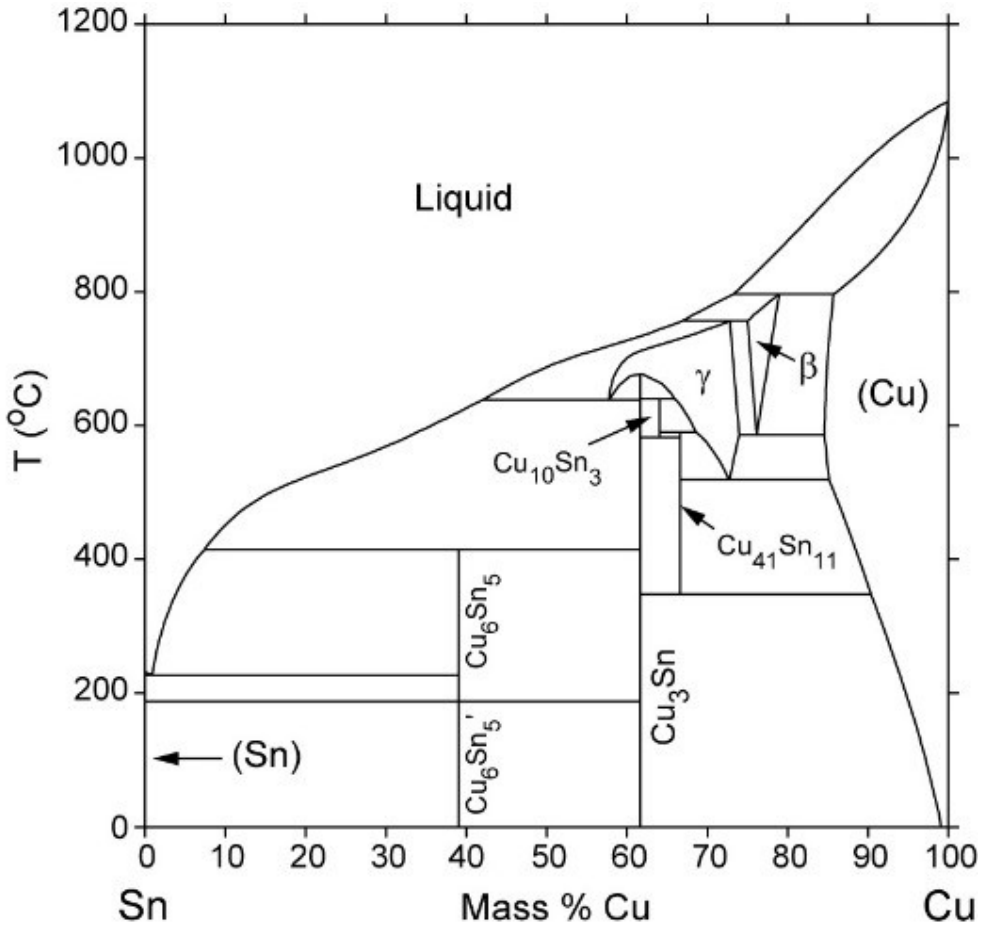


Fig. 2 Sn-Cu phase diagram by National Institute of Standards and Technology [51]

Fig. 2 considers the compositions of η- Cu_6Sn_5 and η′- Cu_6Sn_5 as fixed at ~38.5wt%Cu (a line compound). However, it is more accurate to give them composition ranges. Fig. 3 shows the phase diagram from ASM handbook [52] which gives the composition ranges for η- Cu_6Sn_5 to be 59-60.9wt%Sn and for η′- Cu_6Sn_5 to be 60.1-60.9wt%Sn. Note that the composition of the eutectic point in Fig. 3 is 0.7 wt%Cu which, in more recent thermodynamic work has been corrected to 0.89 wt%Cu [51].

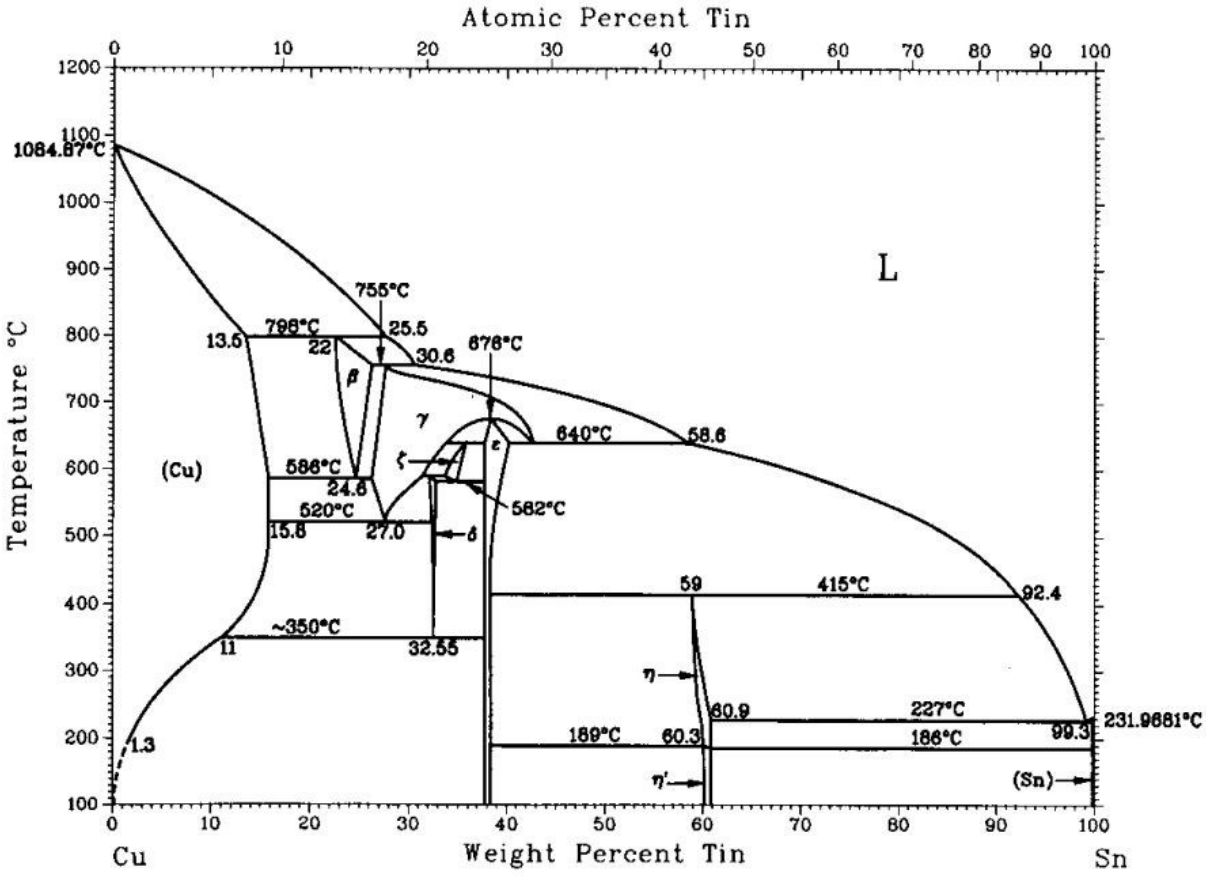


Fig. 3 Sn-Cu phase diagram [52]

Fig. 4 gives the composition for η- Cu_6Sn_5 and η′- Cu_6Sn_5 are 43.4-44.6 at% Sn [53]. Both Fig. 3 and Fig. 4 are based on experimental results.

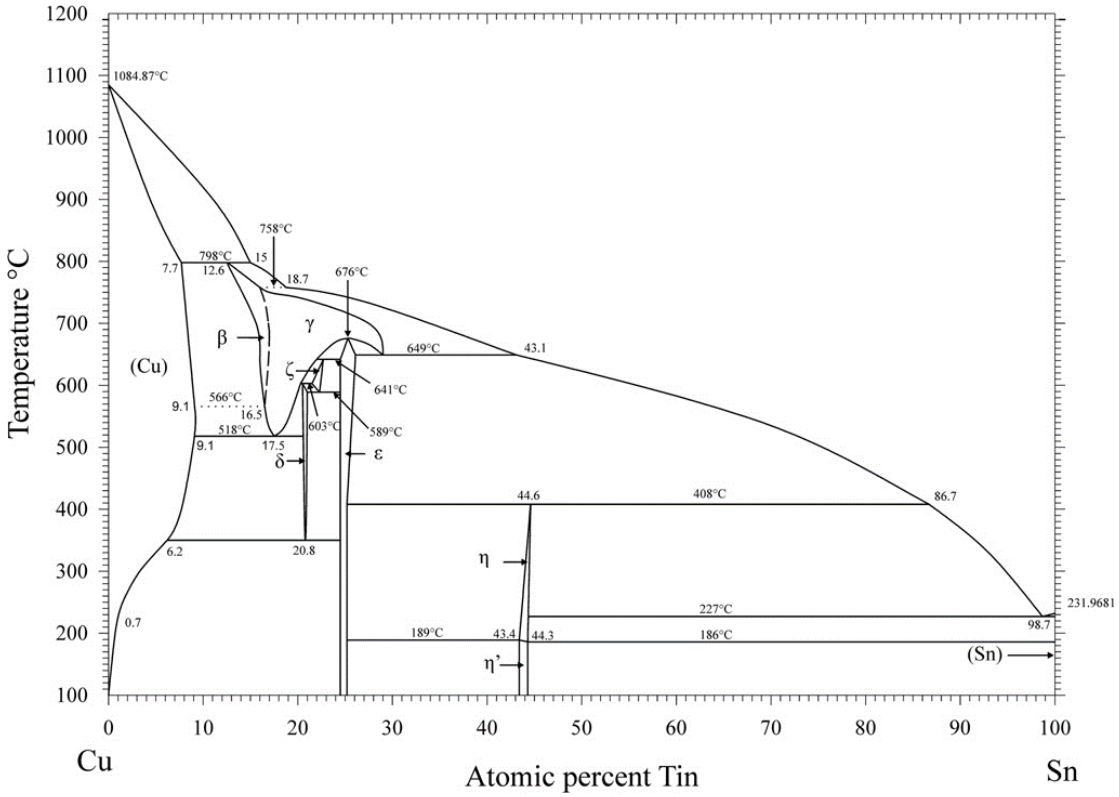


Fig. 4 Cu-Sn phase diagram [53]

2.1.1 Crystallography of the Cu_6Sn_5 polymorphs

The high temperature η- Cu_6Sn_5 phase has a hexagonal unit cell (Fig. 5) with lattice parameters: $a_{hex} = b = 4.19Å$ and $c = 5.086Å$ [54]. The black spheres represent positions fully occupied by Cu, while the mixed black-white spheres are positions 20% occupied by Cu and 80% vacancies. Red spheres are positions is fully occupied by Sn. Thus, the Cu_6Sn_5 composition comes from three lattice sites occupied $Cu_1Cu_{0.2}Sn_1$ giving $Cu_{1.2}Sn$.

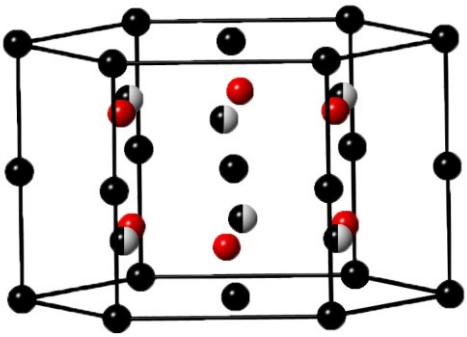


Fig. 5 unit cell of high temperature η- Cu_6Sn_5 (generated in Crystal Maker) [54]

The c/a ratio of hexagonal η-Cu_6Sn_5 is 1.214 which is smaller than many hexagonal crystals. Cu_6Sn_5 can be considered to be pseudo-cubic since it can be represented by a rhomobohedral unit cell with parameters $a_{rho} = 2.954\text{Å}$ and $\alpha = 90.34°$ with the transformation formula [13]:

$$a_{rho} = \sqrt{\frac{1}{9}(3a_{hex}^2 + c^2)}, \quad \alpha = \cos^{-1}\left(\frac{2c^2 - 3a_{hex}^2}{2c^2 + 6a_{hex}^2}\right)$$

Fig. 6 is reproduced from the work of Xian et al. [11]. It summarizes the important atomic planes in η- Cu_6Sn_5 (first column), with corresponding atom locations (second column) with the planar atomic density written below [11]. It can be seen that the $\{11\bar{2}0\}$ planes have the highest atomic density. The third column presents the stacking sequence according to the planes in the first column and most of the planes having stacking sequence as 'ababab', while the atoms on the 1st order pyramidal planes have a complex zig-zag structure.

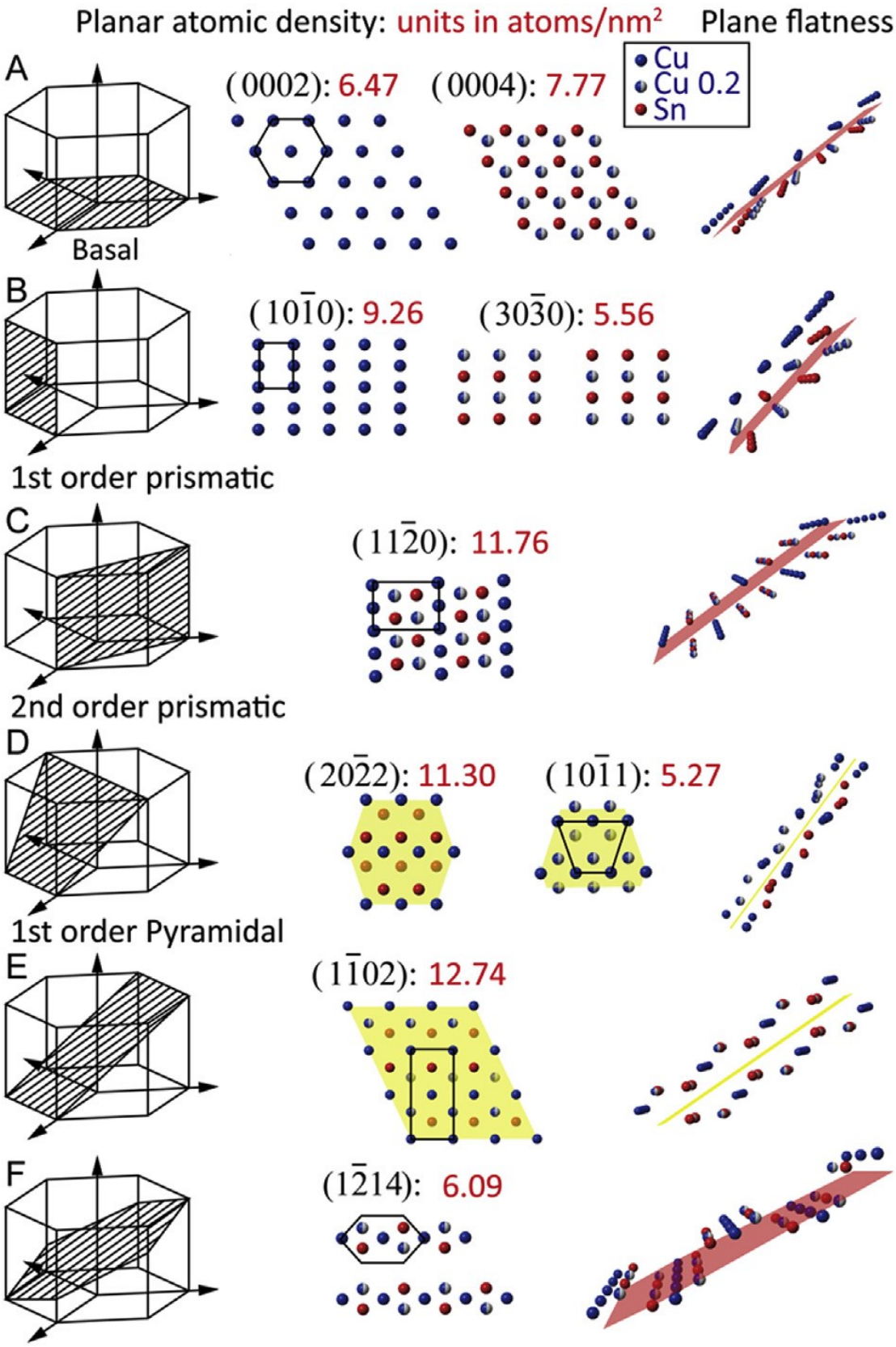


Fig. 6 Important planes, corresponding atomic locations and stacking sequences in η-Cu_6Sn_5 [11]

Fig. 7 shows the monoclinic unit cell for low temperature η'- Cu_6Sn_5 phase where the lattice parameters are $a = 11.022Å, b = 7.282Å, c = 9.827Å, \alpha = 90°, \beta = 98.84°, \gamma = 90°$ [55].

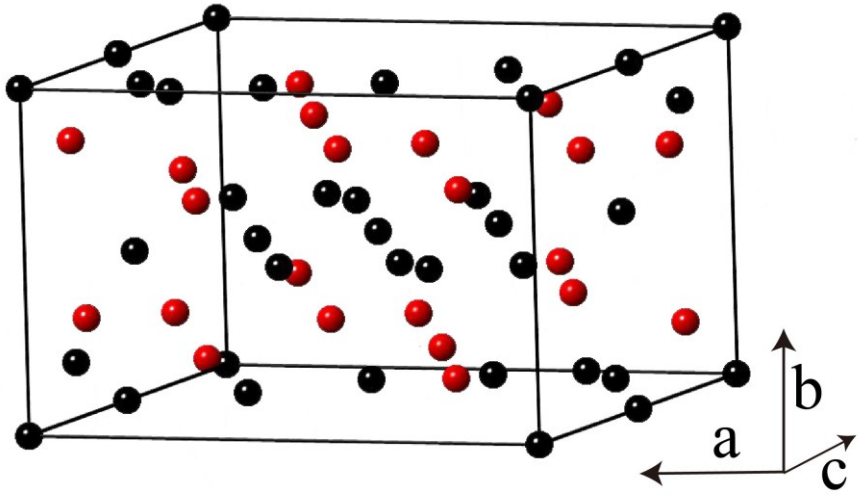


Fig. 7 unit cell of low temperature η'- Cu_6Sn_5 red ball: Sn atom, black ball: Cu atom (generated in Crystal Maker) [55]

η'- Cu_6Sn_5 is stable below ~186℃ [56]. The transformation from η- Cu_6Sn_5 to η'- Cu_6Sn_5 can be during cooling or in the service of electronic devices due to ordering of Cu atoms at previous 20% occupation Cu sites which reduces the symmetry of the crysta [57-59]. However, three more low temperature Cu_6Sn_5 phase structures have been reported which are η^{4+1} ($a = 9.224Å, b = 7.311Å, c = 9.88Å, \alpha = 90°, \beta = 118.95°, c = 90°$) [60], η^6 ($a = 12.6Å, b = 7.27Å, c = 10.2Å, \alpha = 90°, \beta = 90°, c = 90°$) [61] and η^8 ($a = 9.921Å, b = 7.352Å, c = 9.921Å, \alpha = 90°, \beta = 117.46°, c = 90°$) [62].

The $\eta - \eta'$ transformation is not desired, because it is accompanied by a 2.15% expansion [58] which can introduce internal stress and cause the formation of microcracks in the solder joints [63]. Therefore, many researchers have focused on

adding trace elements to stabilize η-Cu_6Sn_5 and prevent or slow down the $\eta - \eta'$ transformation at room temperature. Nogita and Nishimura found that Ni additions form $(Cu,Ni)_6Sn_5$ that stabilises the η phase [64]. Zn can occupy the Sn site in $Cu_6(Sn,Zn)_5$ and up to 0.8-2.1 at% of Zn can stabilize η phase [65]. Au has been reported to have two opposite effects from two intermetallic compounds: $(Cu,Au)_6Sn_5$ can stabilise the η phase, while Au in Sn-Ag-Cu (SAC) solder the formation of $(Cu,Au,Ag)_6Sn_5$ will be unstable [66]. Sb has been found to occupy Sn sites to form $Cu_6(Sn,Sb)_5$ and only a small amount can stabilize the η^8 phase [63].

2.2 Nucleation

The reliability of solder joints has been shown to depend on the microstructure of the solder joints after solidification e.g. the size of intermetallic compounds in the joint [67], and the number and orientations of βSn grains [68]. Since solder joints are small droplets, the most important factor that determines microstructure formation is the nucleation of βSn [69] and Cu_6Sn_5. Other manipulation methods e.g. heat treatment or work hardening processes are not suitable to adjust the performance of joints since joints are used in the as-soldered condition. Therefore, it is very important to control the nucleation events during soldering.

The nucleation of a crystal is the first step of solidification and involves the formation of embroys, which are metastable, of atoms of that crystal usually on the surface of a nucleant particle in the liquid. Embroys with a size larger than the critical size become stable nuclei and grow [70].

In this section, the theory of homogeneous nucleation and heterogeneous nucleation is reviewed followed by the nucleation of Cu_6Sn_5.

2.2.1 Homogeneous nucleation theory

Homogeneous nucleation is a process that the long-range ordered stable solid phase crystals formed from a short-range ordered unstable cluster of atoms in the impurity free liquid [70]. This transformation requires fluctuation of energy and an undercooling below the equilibrium melting temperature to compensate for the formation of new solid-liquid interface. This undercooling can be considered a curvature undercooling or

Gibbs-Thomson undercooling due to the capillarity effect [70]. As an initially formed crystal has the size that is similar to the atomic level, having very large curvature, the pressure difference is built between two phases due to the curvature, and the smaller the crystal the larger the undercooling required and the lower the melting point [70]. This undercooling can be expressed in Equation 1

$$\Delta T_r = \kappa\Gamma \qquad \text{Equation 1}$$

where κ is the curvature and Γ is Gibbs-Thomson coefficient and it is defined as if the curvature is into the liquid the undercooling is positive and the melting point is lower than the equilibrium melting point, the expression for κ and Γ are

$$\kappa = \frac{dA}{dV} = \frac{1}{r_1} + \frac{1}{r_2} \qquad \text{Equation 2}$$

$$\Gamma = \frac{\gamma}{\Delta s_f} \qquad \text{Equation 3}$$

where r_1 and r_2 are maximum and minimum radii of curvature on the surface, γ is the interface energy between liquid and solid phases and Δs_f is the volumetric entropy of solidification. The influence of γ is large when the crystal size is below 10nm e.g. nucleation events.

Assume there is a certain amount of liquid with Gibbs energy G_L, when temperature reduces below the equilibrium melting temperature T_m, there are some stable clusters of atoms form as the nucleus with volume V_s and Gibbs energy G_S, while the remaining

volume of liquid is V_L and the interface formed between the liquid and nucleus has the interface area A_{SL}. G_L and G_S can be expressed as:

$$G_L = (V_S + V_L) \times G_V^L \qquad \text{Equation 4}$$

$$G_s = V_S \times G_V^S + V_L \times G_V^L + A_{SL} \times \gamma_{SL} \qquad \text{Equation 5}$$

where G_V^L and G_V^S are the volumetric Gibbs energy for liquid and solid phases and γ_{SL} is the interfacial energy between solid and liquid phases.

From From Equation 4 and Equation 5, the change in Gibbs free energy during nucleation:

$$\Delta G = G_S - G_L = V_s\left(G_v^s - G_v^l\right) + A_{sl}\gamma_{sl} \qquad \text{Equation 6}$$

$$= V_s \Delta G_v + A_{sl}\gamma_{sl}$$

where ΔG_v is $G_v^s - G_v^l$, having a negative value when T<Tm, which is the volumetric Gibbs energy difference between solid phase and liquid phase and can be understood from Fig. 8.

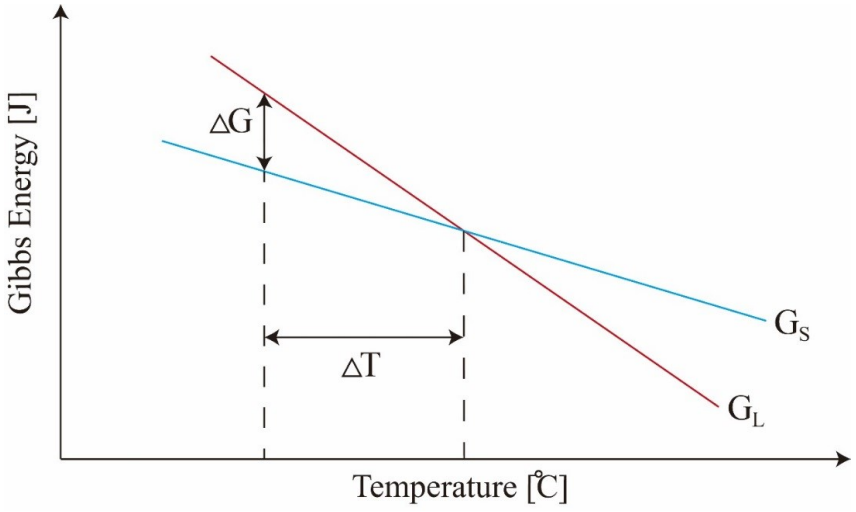


Fig. 8. Gibbs Energy curves for solid and liquid around equilibrium melting point T_m

Fig. 8 shows the Gibbs energy change of liquid phase, G_L, and solid phase, G_S, as a function of Temperature. The Gibbs energy curves have been treated as straight line for simplicity. The difference between the Gibbs energy of two phases, ΔG, represents the driving force of the phase transformation.

$$\Delta G = G_s - G_L = \Delta H - T\Delta S \qquad \text{Equation 7}$$

where H is enthalpy and ΔS_f is entropy of fusion. At T_m, ΔG equals to 0, therefore, Equation 7 can be written as

$$\Delta S_f = \frac{\Delta H}{T_m} = \frac{L}{T_m} \qquad \text{Equation 8}$$

where L is the latent heat of fusion, and as the system release heat during solidification, therefore, L is negative. L_V is the latent heat of fusion per unit volume which can also be expressed by entroy of fusion ΔS_f, $L_V = \rho \Delta S_f T_m$. Substituting Equation 8 into Equation 7:

$$\begin{aligned} \Delta G &= \Delta H - T\Delta S = L - T \times \frac{L}{T_m} \\ &= L \times \left(\frac{T_m - T}{T_m}\right) = \frac{L \times \Delta T}{T_m} \end{aligned} \qquad \text{Equation 9}$$

where ΔT is undercooling. Therefore, the driving force for liquid-solid phase transformation of pure metal depends on the undercooling, the larger the undercooling gives the larger driving force. Therefore, $\Delta G_v = \rho \Delta S_f \Delta T$.

Returning to Equation 6, assuming the nuclei has the sphere morphology with radius r, and Equation 6 can be expressed as

$$\Delta G = -\frac{4}{3}\pi r^3 \Delta G_v + 4\pi r^2 \gamma_{sl} \qquad \text{Equation 10}$$

if there are n nuclei in the liquid, Equation 10 will be change to

$$\Delta G_{hom} = -\frac{4}{3}\pi r^3 \Delta G_v n + 4\pi r^2 \gamma_{sl} n \qquad \text{Equation 11}$$

In Equation 11, the first term is to the power of three and is negative and the second term is to the power of two and is positive, when r is very small, the second term dominants so with the increasing r, ΔG increases. When r reaches the critical value, the first term dominants, therefore, ΔG decreases with increasing r. Therefore ΔG has a maximum value Fig. 9 (c). The critical value is r^*, if r<r^*, the decreasing in r gives the reduction in Gibbs energy of the system, while r>r^*, the increasing of r gives the reduction of Gibbs energy.

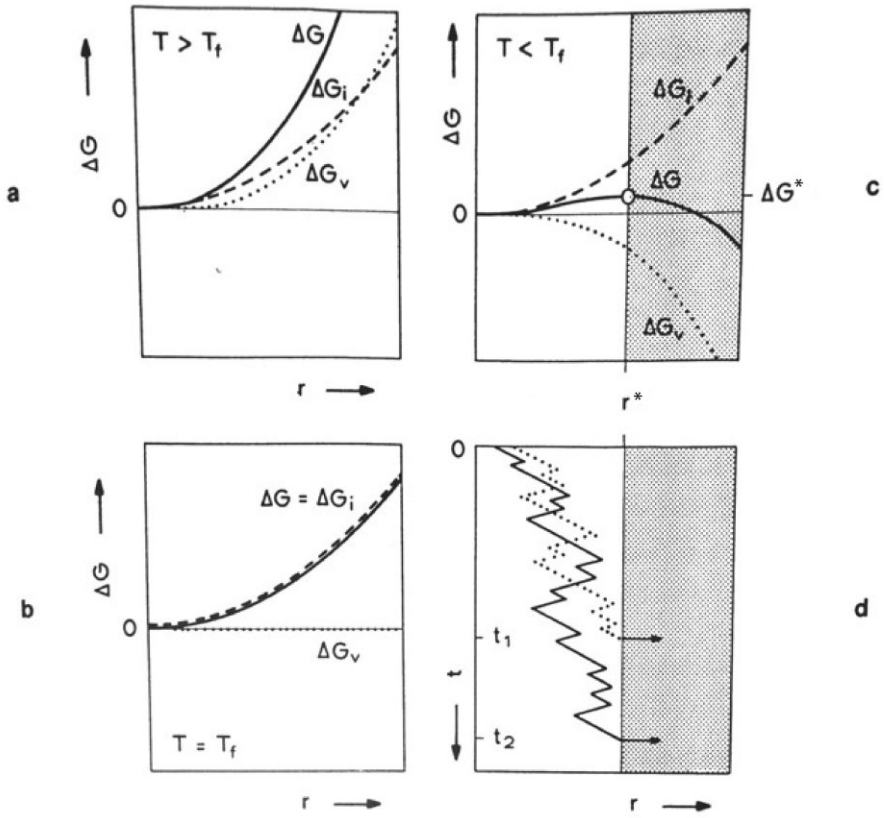


Fig. 9 free energy change and energy fluctuation during nucleation [70]. (a)-(c) are interface Gibbs energy, volumetric Gibbs energy and total Gibbs energy change of the system versus the radius r of the atom cluster at different temperature (d) is random addition of atoms onto the atom cluster

Therefore, the clusters of atoms having radius less than r^* will have larger probability to be dissolved than that of growing, while the clusters having radius larger than r^* will have larger probability to grow.

At r = r^*, turning point can be found by setting the differential of Equation 11 to zero:

$$-4\pi {r^*}^2 n\Delta G_V + 8\pi r^* n\gamma_{SL} = 0$$

$$r^* = \frac{2\gamma_{SL}}{\Delta G_V} = \frac{2\gamma_{SL}}{\rho \Delta S_f \Delta T} \qquad \text{Equation 12}$$

substituting Equation 12 into Equation 11, the activation barrier is:

$$\Delta G^*_{hom} = \frac{4}{3}\pi\left(-\frac{2\gamma_{SL}}{\Delta G_V}\right)^3 n\Delta G_V + 4\pi\left(\frac{2\gamma_{SL}}{\Delta G_V}\right)^2 n\gamma_{SL}$$

$$= -\frac{32}{3}\pi n\frac{{\gamma_{SL}}^3}{{\Delta G_V}^2} + 16\pi n\frac{{\gamma_{SL}}^3}{{\Delta G_V}^2} \qquad \text{Equation 13}$$

$$= \frac{16}{3}\pi n\frac{{\gamma_{SL}}^3}{{\Delta G_V}^2} = \frac{16}{3}\pi n\frac{{\gamma_{SL}}^3}{(\rho \Delta S_f \Delta T)^2} \qquad \text{Equation 14}$$

It can be seen that ΔG^*_{hom} is $1/3$ of the interfacial energy (second term in Equation 13), which means the volumetric Gibbs energy only consume $2/3$ of the interfacial energy, the remaining energy peak, ΔG^*_{hom}, requires the fluctuation of system energy to overcome which can be explained by Fig. 9 (d) which depicts that the liquid atoms will randomly add on or leave the solid nuclei, and the continuous growth of the nuclei requires the fluctuation to make the nuclei larger than the critical size.

2.2.2 Homogeneous nucleation rate

The nucleation rate is defined as the number of nuclei formed in unit time in unit volume. If one nuclei has critical size r^*, the possibility for it to grow larger or dissolve is the same, as in both way the Gibbs energy will be reduced. Therefore, the nucleation rate depends on two factors: one is the amount of atoms clusters, C^*, having size r^*, the second is amount of atoms, f_0, attached to one cluster in the unit time. Therefore the nucleation rate can be expressed as [71]:

$$\dot{N} = f_0 \times C^*$$

C^* depends on the homogeneous nucleation energy ΔG^*_{hom} and has the relation:

$$C^* = C_0 \times \exp(-\frac{\Delta G^*_{hom}}{k_B T})$$

where C_0 is the total amount of atoms in liquid in a unit volume ~$10^{29}/m^3$ [71], k_B is Boltzman constant.

The rate of attachment of liquid atoms onto clusters with critical size, f_0, is a complex term and it depends on the number of neighbouring liquid atoms to the solid atom clusters, the vibration frequency of liquid atoms, the activation energy for liquid atoms jumping out of original positions and the probability for the clusters to accept the liquid atoms. f_0 is sufficient to treat as ~10^{11} [71]

Therefore, the nucleation rate can be expressed as

$$\dot{N} = f_0 \times C^* = f_0 C_0 \exp[-\left(\frac{\Delta G^*_{hom}}{k_B T}\right)]$$

substituting Equation 14:

$$\dot{N} = f_0 \times C^* = f_0 C_0 \exp[-\frac{16\pi {\gamma_{SL}}^3}{3k_B T} \frac{1}{(\rho \Delta S_f \Delta T)^2}]$$

Therefore, $\dot{N} \propto \exp(\frac{-1}{\Delta T^2})$, which means with increasing the undercooling, the nucleation rate increases dramatically.

Some parameters of pure Sn have been summarized in Table 1 and Fig. 10 shows the homogeneous nucleation rate versus undercooling for βSn. Some parameters can be taken are: T_m is 505K, Boltzmann's constant is $1.38 \times 10^{-23} m^2 kg s^{-2} K^{-1}$, $\rho \Delta S_f = 8.4 \times 10^5 J m^{-3} K^{-1}$, and γ_{SL} can be taken as the average from the values in Table 1 which is 0.0595Jm^{-2}.

Table 1 summary of data of Sn

System	T_M/K	$\gamma_{SL}(\times 10^{-3})$/ J/m^2	Reference
Sn	505		[72]
Sn	505	70.6	[73]
Sn	505	54.5	[74]
Sn	505	65	[75]
Sn	505	59.3	[76]
Sn	505	49	[77]
Sn	505	77	[78]
Sn	505	62	[79]
Sn	505	53.6	[76]
Sn	505	60	[80]
Sn	505	44	[81]
Sn	505	66	[80]
Sn	505	62	[76]
Sn	505	50	[82]

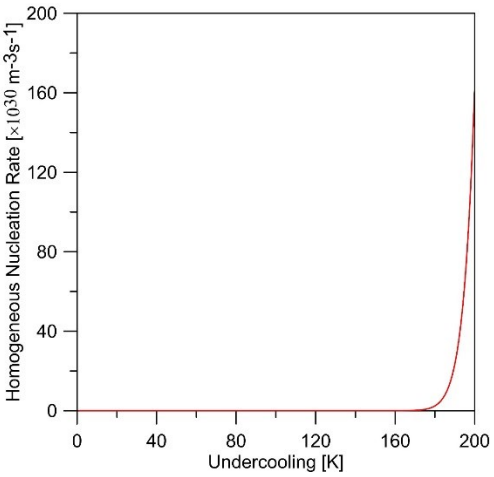


Fig. 10 the homogeneous nucleation rate versus undercooling for βSn

From Fig. 10, it can be seen that there is a critical undercooling ΔT^*, below which, nucleation will not happen, while upon reaching, the nucleation rate will increase dramatically. The appearance of critical undercooling can be understood from

$$r^* = \frac{2\gamma_{SL}}{\Delta G_V} = \frac{2\gamma_{SL}}{\rho \Delta S_f \Delta T} \qquad \text{Equation 12}$$

Equation 12, it can be seen that when undercooling ΔT increases, r^* decreases. The maximum atom cluster, r_{max}, that can be appear during homogeneous nucleation also depends on the undercooling, but the relationship is the lower undercooling gives smaller r_{max} because at the lower undercooling, the temperature is higher and the dynamic of atoms is larger. Therefore, the probability to form larger clusters issmaller. The relation between r^* and r_{max} can be seen from Fig. 11 [71].

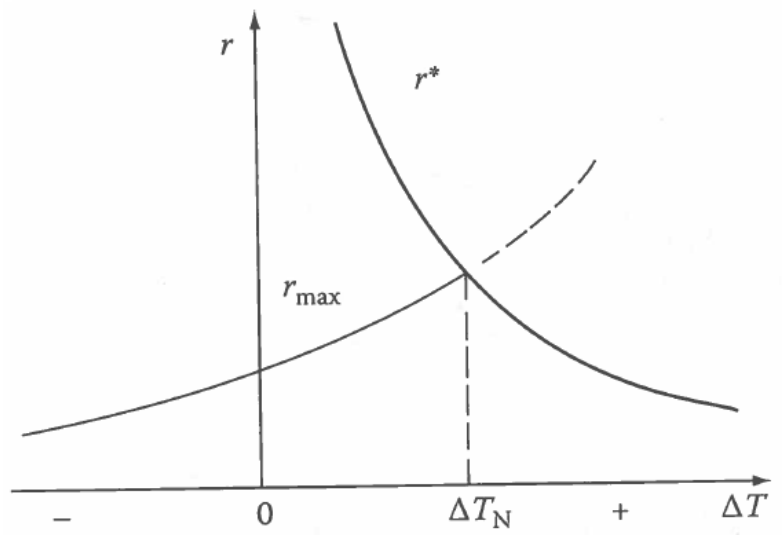


Fig. 11 Critical nuclei size r^* and the maximum size a nuclei can form r_{max} versus undercooling [71]

It can be seen that two curves intercept at critical undercooling ΔT^*, and below ΔT^*, the maximum clusters that can form is smaller than the critical size r^*, therefore, nucleation will not happen, while beyond ΔT^*, the clusters have probability to be larger than r^*, therefore, homogeneous nucleation can happen.

2.2.3 Heterogeneous nucleation theory

In reality, homogeneous nucleation is very hard to happen, because the impurity always exists in the melt or on the mould e.g. oxide or nitride, which can be the substrate for nucleation. Fig. 12 [71] shows a model of a spherical cap nucleating on a pre-existing solid-liquid interface.

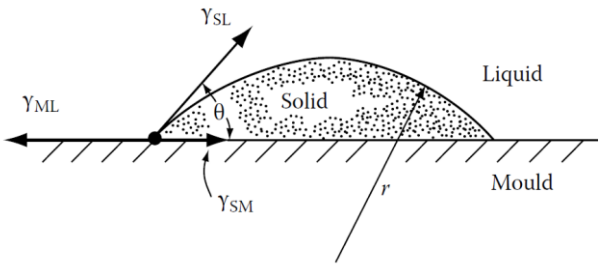


Fig. 12 model of heterogeneous nucleation: a spherical cap nucleates on the flat wall [71]

In Fig. 12, it can be seen that the spherical cap has a wetting angle θ° with the substrate. The wetting angle is determined by the surface tension between solid liquid γ_{SL}, liquid substrate γ_{ML} and solid substrate γ_{SM}. The balance is achieved at the point where three phases join together:

$$\gamma_{SM} + \gamma_{SL}\cos\theta = \gamma_{ML} \qquad \text{Equation 15}$$

The existing impurities have already had interfaces with the melt, therefore if the solid nuclei is going to nucleate on such interface, the existing impurity/liquid interfaces will be replaced, so the energy needed to the solid nuclei/liquid interface will be less. Therefore, the Gibbs energy for such a spherical cap to nucleate can be expressed by:

$$\Delta G_{het} = V_s\Delta G_v + A_{SL}\gamma_{SL} + A_{SM}\gamma_{SM} - A_{SM}\gamma_{ML} \qquad \text{Equation 16}$$

the V_s, A_{SL} and A_{SM} can be expressed by:

$$V_s = \frac{\pi r^3}{3}(2 - 3cos\theta + cos^3\theta) \qquad \text{Equation 17}$$
$$A_{SL} = 2\pi r^2(1 - cos\theta)$$
$$A_{SM} = \pi r^2 sin^2\theta$$

substituting Equation 17 into Equation 16:

$$\Delta G_{het} = \left\{-\frac{4}{3}\pi r^3\Delta G_v + 4\pi r^2\gamma_{SL}\right\} \times \frac{(2+\cos\theta)(1-\cos\theta)^2}{4} \qquad \text{Equation 18}$$
$$= \left\{\frac{4}{3}\pi r^3\Delta G_v + 4\pi r^2\gamma_{SL}\right\} f(\theta)$$

Comparing Equation 18 with Equation 11, it can be seen that ΔG_{het} is just a fraction of ΔG_{hom}. Therefore, the critical radius for heterogeneous nucleation is the same as that in homogeneous nucleation, while the nucleation rate has the similar format:

$$\dot{N}_{het} = f_1 N_1 \exp\left(-\frac{16\pi\gamma_{sl}^3}{3}\frac{f(\theta)}{kT\left(\rho\Delta S_f \Delta T\right)^2}\right) \qquad \text{Equation 19}$$

where f_1 is the frequency factor and N_1 is the amount of heterogeneous nucleant per unit volume in the melt.

There are several factors may influence the heterogeneous nucleation rate:

(1) undercooling: larger undercooling gives larger heterogeneous nucleation rate

(2) impurity: it can be seen from Equation 19 that smaller $f(\theta)$ will give larger heterogeneous nucleation rate, and $f(\theta)$ depends on θ, smaller θ gives larger $cos\theta$ and smaller $f(\theta)$ and so γ_{SL}, γ_{ML} and γ_{SM} determine the $f(\theta)$. In reality, the γ_{SL}, γ_{ML} will not vary to much, so lower γ_{SM} will contribute to the higher nucleation rate. Two kinds of heterogeneous nucleation site may give lower γ_{SM}: first is the site has similar crystallographic parameters, so the misfit along the interface is low, the second type is if the site has groove or micro-cracks on the surface.

(3) the number of heterogeneous nucleation site: larger number will contribute to larger nucleation rate.

2.2.4 Prediction of potent heterogeneous nucleation sites

If added particles and the target phase can form a coherent interface with lattice mis-

match less than ~10%, the particles are usually effective heterogeneous nucleation sites for the target phase [83]. Bramfitt developed a 'planar lattice disregistry model' to calculate the linear disregistry [84]. In the model, the 'linear disregistry' in three directions with the lowest index within a perpendicular quadrant are averaged. However this model does not consider the lattice vacancies.

2.2.5 Nucleation of Cu_6Sn_5 during soldering

During soldering of Sn-xCu alloys onto Cu substrate, Cu_6Sn_5 may nucleate on Cu substrate and in the bulk solder.

The nucleation of interfacial Cu_6Sn_5 occurs rapidly when liquid solder wets the Cu substrate [85-87] as the Cu dissolution rate from the Cu substrate into liquid is very rapid. The morphology of interfacial Cu_6Sn_5 may depend on the orientation of Cu grains on the interface between the Cu pad and the liquid solder as shown in Fig. 13 by Suh et al. [88].

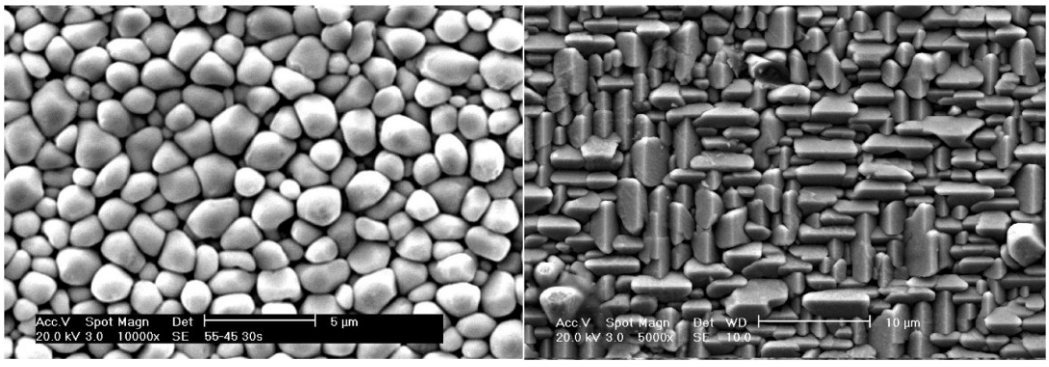


Fig. 13 Top views of interfacial Cu_6Sn_5 layer after fully etched Sn (a) on polycrystalline Cu substrate (b) on single crystalline (001) Cu [88].

It is clearly shown that on polycrystalline Cu substrate, interfacial Cu_6Sn_5 nucleated and grew into scallop morphology while on single Cu crystalline (001) surface,

interfacial Cu_6Sn_5 nucleated and grew into prism morphology. Suh et al. also suggested six preferred orientation relationships (ORs) between hexagonal Cu_6Sn_5 and (001) Cu:

$$(010)_{Cu6Sn5}//(001)_{Cu}$$
$$(343)_{Cu6Sn5}//(001)_{Cu}$$
$$(\text{-}34\text{-}3)_{Cu6Sn5}//(001)_{Cu}$$
$$(101)_{Cu6Sn5}//(001)_{Cu}$$
$$(141)_{Cu6Sn5}//(001)_{Cu}$$
$$(\text{-}14\text{-}1)_{Cu6Sn5}//(001)_{Cu}$$

in all the cases above, $[\bar{1}01]_{Cu6Sn5}$ is parallel to the $[110]_{Cu}$ [88].

The misfit was calculated in order to examine these ORs. The Cu atomic spacing along $[\bar{1}01]_{Cu6Sn5}$ is 2.5573 Å. The Cu atomic spacing along $[110]_{Cu}$ is $3.6078 \times \frac{\sqrt{2}}{2} = 2.5511$Å, the linear misfit between the Cu substrate and interfacial Cu_6Sn_5 layer is $\frac{2.5573-2.5511}{2.5511} = 0.24\%$ which is very low and same as that stated in [88].

Further detailed investigations of the different single Cu surface substrate on the morphology of the interfacial Cu_6Sn_5 layer was reported by Zou et al. [89]. They studied four Cu single crystals with different surface planes: (001), (011), (111) and (123), facing the molten solder. The isothermal reaction temperature was 260℃.

They found that on $(001)_{Cu}$, Cu_6Sn_5 grains form a prism texture aligned with two perpendicular directions (Fig. 14a).

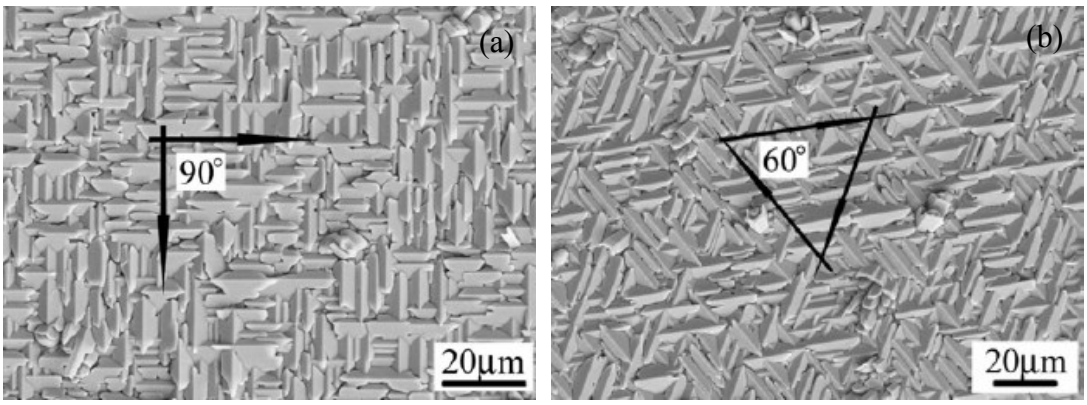


Fig. 14 Morphologies of prism interfacial Cu_6Sn_5 on (001) single crystal Cu substrate at 260℃ for 60s (a), on (111) single Cu substrate at 260℃ for 60s (b) [89]

On (111) of Cu, the Cu_6Sn_5 grains also form as prism morphology, however aligned with three directions forming 60° to each other (Fig. 14b).

By analyzing the Kikuchi bands from EBSD experiments, the preferred ORs are presented as below:

$$\text{OR1}: (010)_{Cu_6Sn_5}||(001)_{Cu}$$
$$[-201]_{Cu_6Sn_5}||[110]_{Cu}$$
$$[-201]_{Cu_6Sn_5}||[-110]_{Cu}$$

$$\text{OR 2}: (010)_{Cu_6Sn_5}||(111)_{Cu}$$
$$[-201]_{Cu_6Sn_5}||[1-21]_{Cu}$$
$$[-201]_{Cu_6Sn_5}||[-211]_{Cu}$$
$$[-201]_{Cu_6Sn_5}||[11-2]_{Cu}$$

Note that on $(001)_{Cu}$, $[110]_{Cu}$ and $[-110]_{Cu}$ are perpendicular to each other, while on $(111)_{Cu}$, $[1-21]_{Cu}$, $[-211]_{Cu}$ and $[11-2]_{Cu}$ are at 60° to each other. Lattice misfits are examined with the help of crystal maker. On $(010)_{Cu_6Sn_5}$, the Cu atom spacing is 0.25478nm along [-201] (Fig. 15(a) and (b)). On $(001)_{Cu}$, the Cu atom spacing is 0.2556nm along [110] and [-110], which are perpendicular to each other (Fig. 15 (a)), while on $(111)_{Cu}$, the Cu atom spacing is 0.2556nm along [-110], [0-11] and [-101], which are 60° to each other (Fig. 15(b)). The misfit between Cu atoms between the direction on $(010)_{Cu_6Sn_5}$ and the directions $(001)_{Cu}$ and $(111)_{Cu}$ are calculated to be $\frac{0.2556-0.25478}{0.25478} = 0.32\%$ which is low enough for nucleation of interfacial Cu_6Sn_5 . This explain the 90° and 60° morphologies of interfacial Cu_6Sn_5 on (001) and (111) surface of single crystal Cu. Those orientation relationships are drawn in Fig. 15, and FCC Cu and monoclinic Cu_6Sn_5 with C12/C1 structure are selected [55].

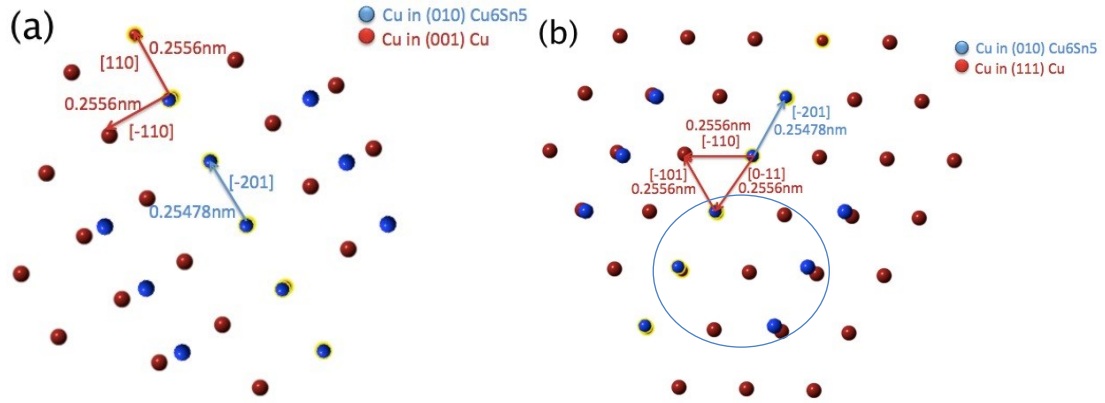


Fig. 15 schematic drawing of planner lattice match of $(010)_{Cu_6Sn_5}$ *with* $(001)_{Cu}$ and $(010)_{Cu_6Sn_5}$ *with* $(111)_{Cu}$ (Generated in Crystal Maker) [55]

Fig. 15(a) shows a good lattice match along $[110](001)_{Cu}$ and $[-201](010)_{Cu_6Sn_5}$, however, the planar disregistry is not good. Fig. 15(b) shows both a good lattice match along $[0-11](111)_{Cu}$ and $[-201](010)_{Cu_6Sn_5}$ and a good planar match with a planar lattice disregistry of 4.1% which is calculated below. This means the orientation relationship between $[0-11](111)_{Cu}$ and $[-201](010)_{Cu_6Sn_5}$ probably has the lower interfacial energy and is expected to be more favourable for the nucleation of Cu_6Sn_5 crystals.

In order to calculate lattice disregistry, an area where Cu atoms in $(010)_{Cu_6Sn_5}$ and $(111)_{Cu}$ match well is selected (blue circle in Fig. 15). The area is shown in Fig. 16.

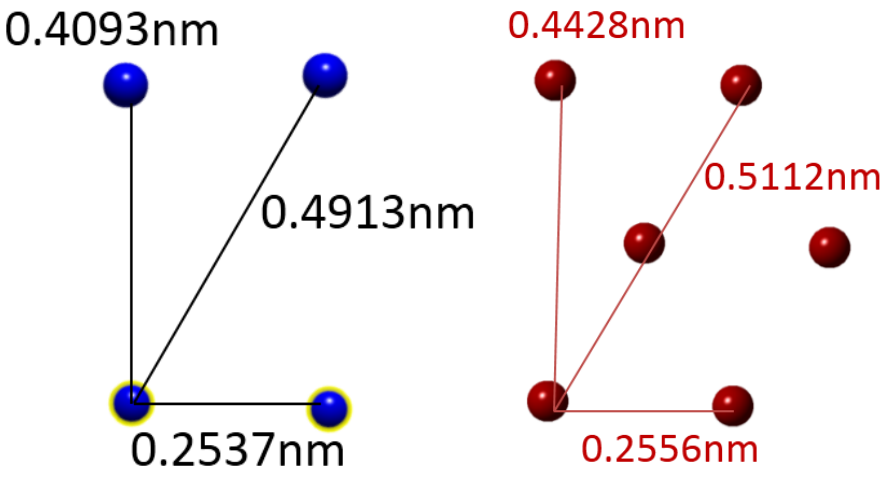


Fig. 16 enlarged area of blue circle in Fig. 15. Blue represents Cu atoms on Cu_6Sn_5 while red represents Cu atoms on Cu. (generated in Crystal Maker)

The planar lattice disregistry can be calculated according to data from Fig. 16 with the Bramfitt model [84]:

$$\frac{\left|\frac{0.4428-0.4093}{0.4428}\right|+\left|\frac{0.5112-0.4913}{0.5112}\right|+\left|\frac{0.2556-0.2537}{0.2556}\right|}{3}=4.1\%$$

On (011) and (123) of Cu, the Cu_6Sn_5 grains form scallop morphology. After aging or with prolonged isothermal reaction time, the morphologies of Cu_6Sn_5 change to scallop in all cases.

The Cu_6Sn_5 structure Zou et al. used is monoclinic η', while from the works of Tian et al. [8], they found two ORs between hexagonal ηCu_6Sn_5 and single Cu crystal (001) and (111) surfaces:

$$\begin{gathered}\text{OR1}:\ (2-1-10)_{Cu_6Sn_5}||(001)_{Cu}\\ [0001]_{Cu_6Sn_5}||[110]_{Cu}\\ [0001]_{Cu_6Sn_5}||[-110]_{Cu}\\ \text{OR2}:\ (2-1-10)_{Cu_6Sn_5}||(111)_{Cu}\\ 0001]_{Cu_6Sn_5}||[-110]_{Cu}\\ [0001]_{Cu_6Sn_5}||[01-1]_{Cu}\\ [0001]_{Cu_6Sn_5}||[-101]_{Cu}\end{gathered}$$

The ORs shown by Zou et al. and that shown by Tian et al. are equivalent, as [0001] in hexagonal ηCu_6Sn_5 is equivalent to the $[\bar{2}01]$ direction in monoclinic η'Cu_6Sn_5. Actually it is more accurate to use ηCu_6Sn_5 instead of using η'Cu_6Sn_5, because the nucleated phase upon liquid solder touching the Cu substrate is hexagonal ηCu_6Sn_5.

Beside their nucleation and growth on the Cu substrate, primary Cu_6Sn_5 crystals also form in the liquid solder in cases where the liquid composition is hypereutectic due to Cu substrate dissolution. Primary Cu_6Sn_5 may form by growth from the pre-existing Cu_6Sn_5 interfacial layer [10, 50, 90, 91]. Primary Cu_6Sn_5 can also nucleate and grow

in the liquid away from the layer [27, 91]. Fig. 17 [91] presents nine typical frames from synchrotron radiography of Sn-0.7wt%Cu paste soldered onto Cu substrate and Fig. 17 (e) shows the first observation of primary Cu_6Sn_5 in which there are two very small primary Cu_6Sn_5 crystals just after nucleation that have started to grow and in Fig. 17 (i) four primary Cu_6Sn_5 labelled A,B,C and D after solidification which all nucleated in the liquid.

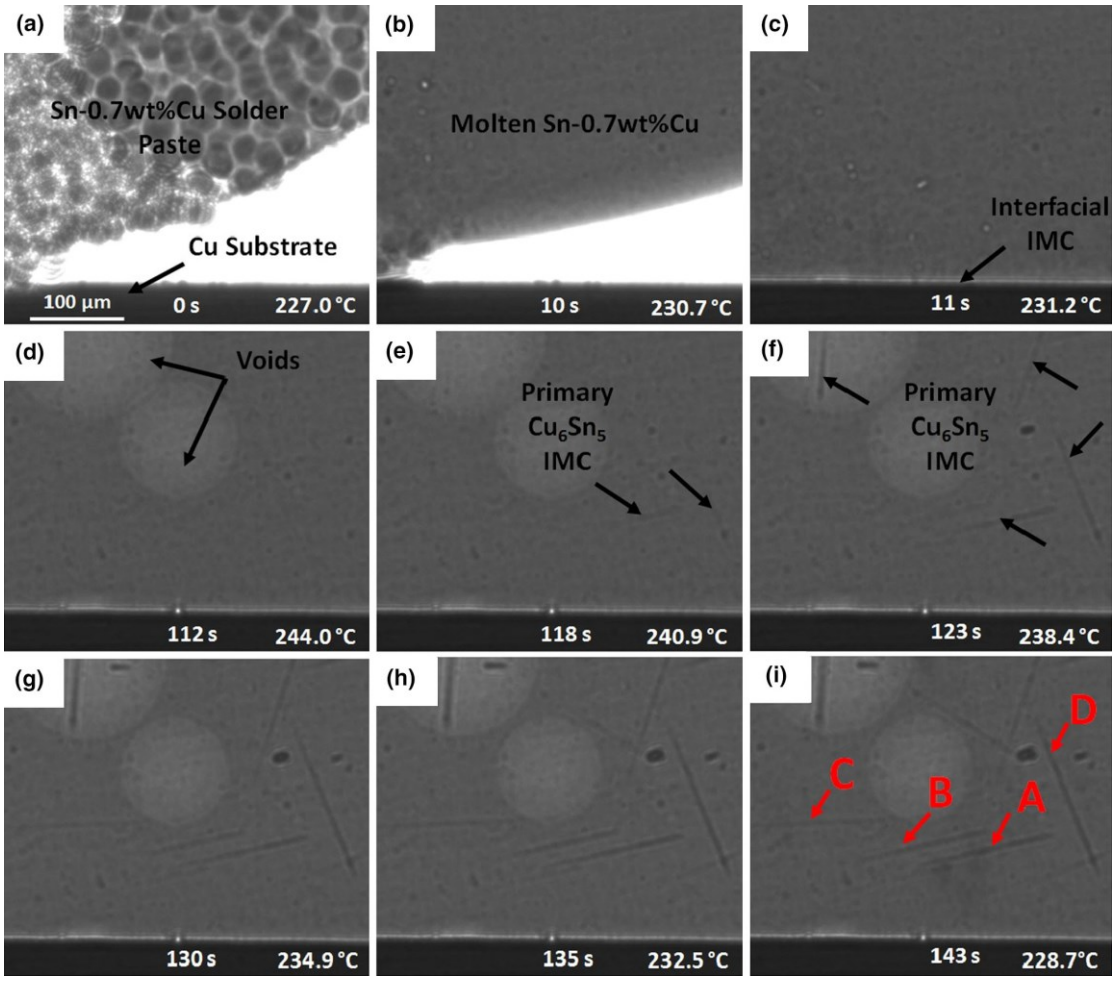


Fig. 17 in-situ observation of soldering reaction of Sn-0.7wt%Cu paste/Cu at (a) 0 s, (b) 10 s, (c) 11 s, (d)112 s, (e) 118 s, (f) 123 s, (g) 130 s, and (i) 143s [91]

Fig. 18 [27] presents another image sequences of soldering of SAC305 solder on Cu from synchrotron radiography. It clearly shows in Fig. 18 (b) a primary Cu_6Sn_5 was

growing from upper right of the solder ball. Meanwhile, it also records the growth of primary Cu_6Sn_5 from the interfacial layer.



Fig. 18 image sequences of the formation of primary Cu_6Sn_5 in SAC305/Cu joint from synchrotron radiography (modified from [27])

Cu_6Sn_5 nucleation can be promoted by dilute addition of Al in the liquid solder in which $\gamma_1 - Cu_9Al_4$ and $\delta - Cu_{33}Al_{17}$ phases act heterogeneous nucleation sites (Fig. 19 [13]) for primary Cu_6Sn_5 which give similar lattice match.

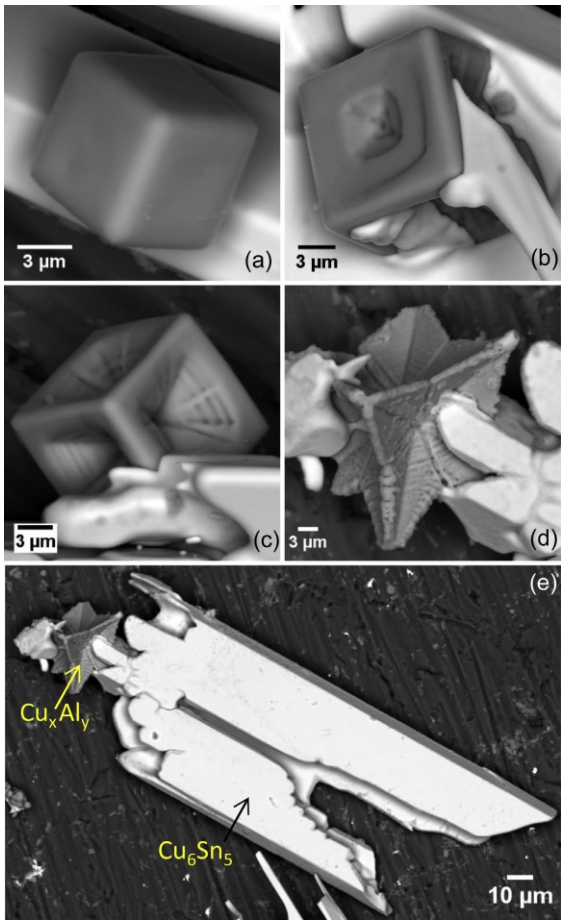


Fig. 19 Backscatter images of Cu_xAl_y with increasing growth distance in (a)-(d) in Sn-4Cu-0.2Al where the primary Cu_6Sn_5 were attached on. (e) Cu_6Sn_5 grew on $Cu_{33}Al_{17}$. [13]

The orient relationship between $\gamma_1 - Cu_9Al_4$ and $\delta - Cu_{33}Al_{17}$ and Cu_6Sn_5 are the same [13]:

$$(1\bar{2}10)_{Cu_6Sn_5}//(10\bar{1})_{Cu_xAl_y}\ or\ (1\bar{1}00)_{Cu_6Sn_5}//(2\bar{1}\bar{1})_{Cu_xAl_y}$$

$$[0001]_{Cu_6Sn_5}//[111]_{Cu_xAl_y}$$

The orientation relationships between Cu_6Sn_5 and βSn has been measured by Xian et al. to be [92]:

$$\text{OR1: } [0001]//[11\bar{2}]\,,(0\bar{1}00)//(\bar{2}41)$$

$$\text{OR2: } [0001]//[11\bar{2}]\,,(10\bar{1}0)//(111)$$

which are shown in Fig. 20 and the same ORs were measured by Ma et al. [93].

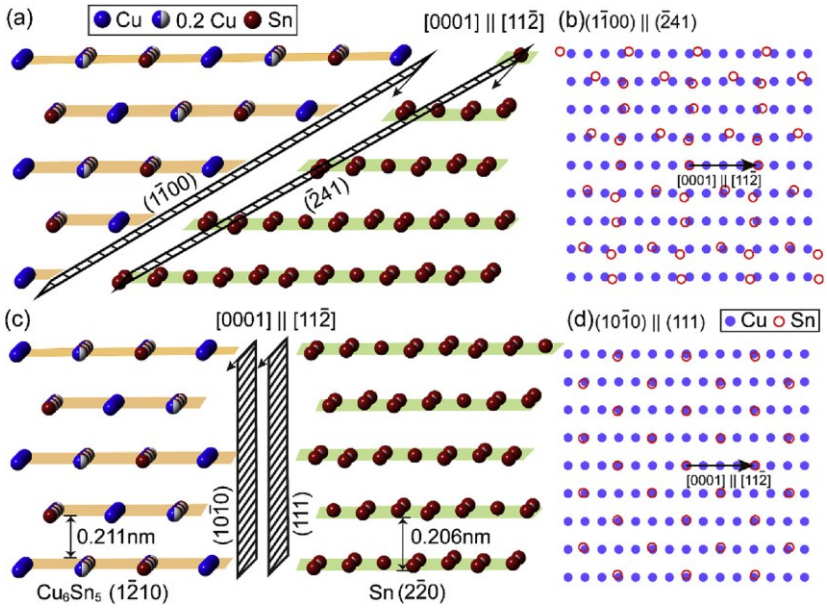


Fig. 20 (a)(c) Schematic representation of OR1 and OR2 between Cu_6Sn_5 and βSn. (b)(d) Planar lattice match for OR1 and OR2 [92].

2.3 Growth of Crystal in liquid

It has been found the morphology and size of Cu_6Sn_5 can influence the reliability of the Sn-xCu/Cu solder joints e.g. during shear impact test, tensile test, thermal mechanical fatigue etc. [49, 67, 94]. Thus, it is important to investigate under what conditions the Cu_6Sn_5 will grow to what morphology and how to control the crystal size.

This section overviews the theory of S-L interface morphology, non-faceted and faceted growth, the transition between the non-faceted and faceted S-L interfaces, the FDR model for Cu_6Sn_5 layer growth during liquid state and primary Cu_6Sn_5 growth.

2.3.1 The morphology of solid liquid interface (S-L) interface

The growth of crystals is the process of a S-L interface propagating into a liquid by the attachment of liquid atoms onto the S-L interface. The attachment of atoms depends on the S-L interface roughness which depends on the Gibbs energy of the interface i.e. whether the interfacial Gibbs energy can be minimized by roughening the interface (to maximize entropy) or by creating an atomically smooth interface (to minimize the number of high enthalpy S-L 'broken' bonds). This can be estimated using Jackson's alpha parameter, also known as the dimensionless entropy of fusion (solidification):

$$\alpha = \frac{\Delta S_f}{R} = \frac{\Delta H_f T_m}{R}$$

where ΔS_f is the entropy of fusion, ΔH_f is the latent heat of fusion, T_m is the melting point, and R is the gas constant. The Jackson parameter predicts two types of S-L interface depending on whether $\alpha \leq 2$ or $\alpha > 2$. Cu_6Sn_5 has an α value of approximately 2 and can grow with both types of interface as shown in [11].

(1) atomically rough S-L interfaces (Fig. 21(b)):

When $\alpha \leq 2$, the minimum S-L interface energy is when half of the atomic positions are occupied by solid atoms, another half are occupied by vacancies. This S-L interface is rough at the atomic level, having an interface width of several atomic planes, and is macroscopically smooth.

(2) atomically smooth S-L interfaces (Fig. 21(a)):

When $\alpha > 2$, the minimum S-L interface energy appears when the fraction of solid atoms on the interface approaches 0 or 1 when the S-L interface is atomically smooth and the thickness of the interface is one atomic plane with a sharp boundary between the solid and liquid.

Those two types of interface lead to the different growth mechanisms and morphologies which are non-faceted and faceted interfaces.

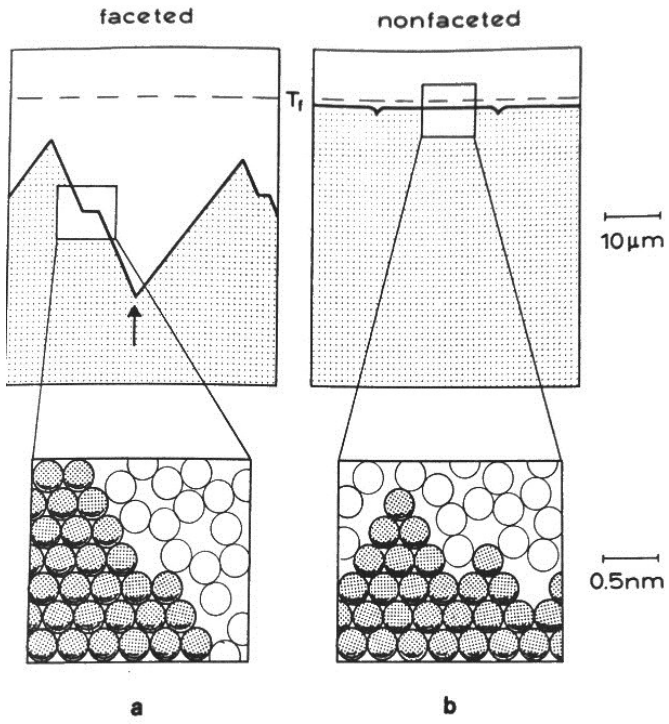


Fig. 21 (a) faceted interface and (b) non-faceted interface [70]

2.3.2 Growth of non-faceted S-L interfaceas

Attachment of atoms onto an atomically rough S-L interface will create a non-faceted interface because every atomic position along the S-L interface has a similar probability for attachment, which makes the S-L interface energy a weak function of the crystal orientation. The atom attachment onto non-faceted interfaces is relatively easy and the kinetic undercooling, ΔT_k, is very small which means that the growth is mainly controlled by the interaction between the diffusion of heat / solute from the interface and curvature of the interface. The growth morphology is then determined by the degree of constitutional supercoiling in the liquid ahead of the interface, the interface velocity and the temperature gradient in the liquid. The morphologies generated by S-L interface growth in pure metals and in alloys is summarized in Table 2 [70, 95].

Table 2 summary of S-L interface stability in pure metal and alloy[70, 95]

	$G_L<0$	$G_L>0$	$G_L \gg \left(\frac{dT_L}{dx}\right)_{interface}$
Pure metal	unstable e.g. equiaxed crystal	Stable (planar)	Stable e.g. planar
Alloy	Unstable e.g. equiaxed crystal	Unstable e.g. dendrite $G_L < \left(\frac{dT_L}{dx}\right)_{interface}$ unstable e.g. cellular $G_L \approx \left(\frac{dT_L}{dx}\right)_{interface}$	Stable e.g. planar

The growth of Cu_6Sn_5 crystals in Sn-rich liquid will develop large constitutional supercooling because of the steep Cu_6Sn_5 liquidus line. Thus, when Cu_6Sn_5 grows with a non-faceted interface, the growth morphology is dendritic [11]. The solidification of βSn in soldering processes involves free growth into undercooled liquid with $G_L<0$

because βSn requires a relatively high undercooling. Therefore, βSn grows as dendrites in solder joints.

2.3.3 Growth of faceted S-L interfaces

Faceted S-L interfaces occur in phases having a S-L interfacial energy that strongly depends on the orientation of the crystal, and atomically smooth interfaces with relatively few ledges and kinks so the liquid atoms have strong preference to join at specific positions along the S-L interface, Fig. 22 [95]. Therefore, the growth of faceted S-L interfaces is limited by attachment kinetics.

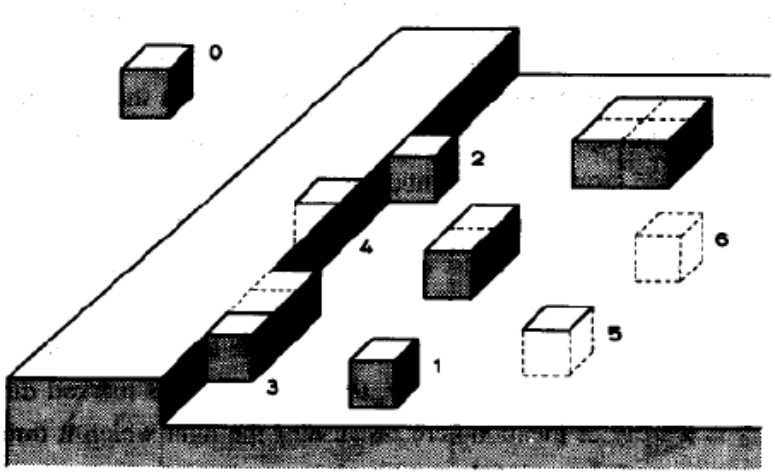


Fig. 22 different positions that liquid atoms can join on the S-L interface of a cubic crystal [95]

Fig. 22 shows different possible atomic sites that the liquid atoms might join on the S-L interface. Comparing site 3 and site 1, if an atom joins the crystal at site 3 then the total increase in the interfacial area is zero; however, if liquid atom joins site 1, then four more surfaces have been added to the total interfacial area and the interfacial energy increases. Meanwhile, the attachment to site 3 has fewer high-energy S-L bonds than at site 1 which means that site 3 has a lower chance of desorption of liquid atoms.

Faceted S-L interface growth is interface controlled and anisotropic in atomic attachment kinetics. Crystal surfaces that are more closely packed tend to have higher Jackson alpha factor which makes them more atomically smooth (fewer ledges etc.), and gives them slower interface attachment kinetics. Since faceted crystals are bounded by the slowest growing planes, the growth facets tend to be the closest packed planes which gives faceted surfaces the same symmetry as their crystallographic symmetry. The stability of a faceted S-L interface occurs because preferable attachment sites such as 4 and 5 are quickly 'filled in' and rapid lateral growth may quickly remove any unstable perturbations into the liquid [96].

In theory, faceted growth should remove all ledges and kinks but, in reality, crystal defects often provide perpetual ledges such as screw dislocations, re-entrant corners at twin boundaries and twist boundaries, Fig. 23 [95].

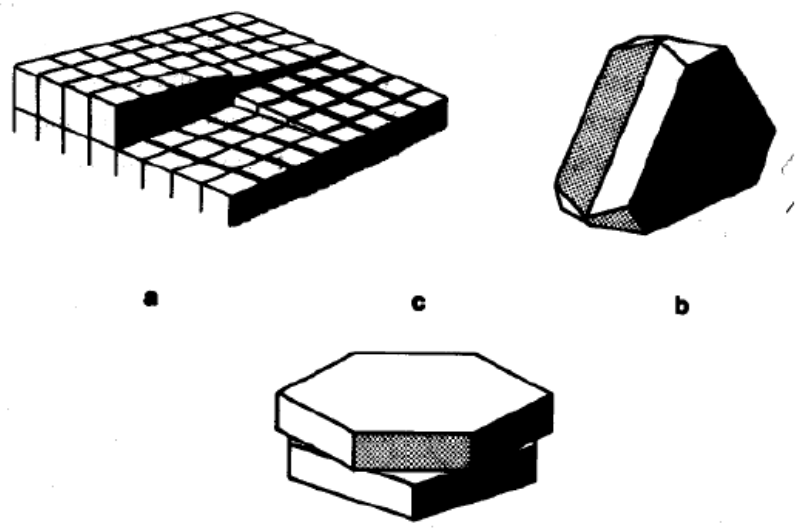


Fig. 23 the defects for faceted crystals (a) screw dislocation (b) twining (c) twisted boundary [95]

2.3.4 Growth of interfacial intermetallic compounds during soldering

2.3.4.1 Soldering reactions between Sn-xCu/Cu solder joint

The Sn-Cu phase diagram is reproduced in Fig. 24 where the red line shows a typical industrial peak reflow temperature.

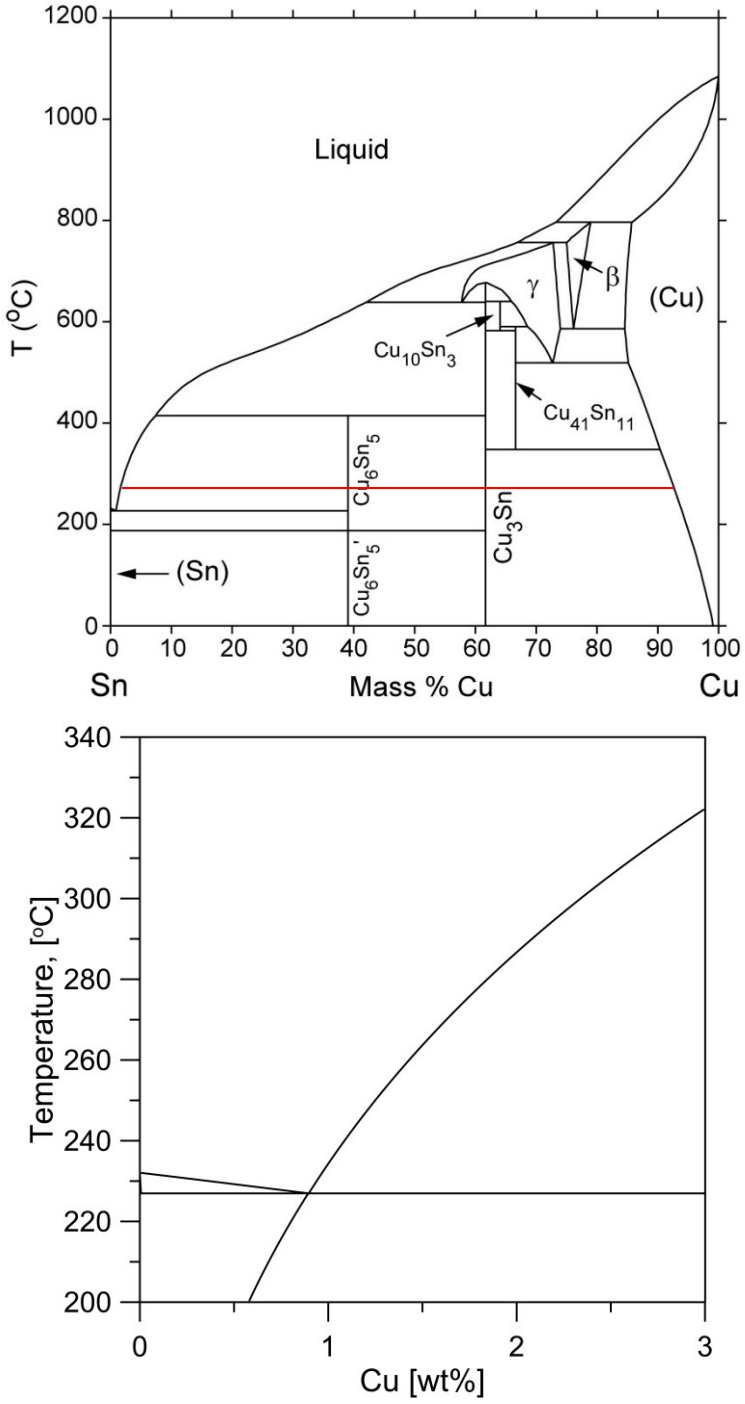


Fig. 24 (a) whole Sn-Cu phase diagram [51] (b) Sn rich part data from Thermo-Calc [97]

Assuming local equilibrium at all interfaces, a diffusion couple between liquid Sn and Cu should form a layered structure of Sn-rich liquid-high temperature Cu_6Sn_5 (hexagonal)-Cu_3Sn-Cu. During the liquid heating stage of the soldering process, individual interfacial Cu_6Sn_5 grains nucleate along the Cu-L interface. Some researchers suggest that there are liquid channels between the interfacial Cu_6Sn_5 scallops [86]. The continuing growth of the interfacial layer is supported by the volume diffusion of dissolved Cu via those channels, as triple points are effective diffusion pathways [86, 98-100]. Other researchers suggest that, after nucleation, the Cu_6Sn_5 grains spread across the interface, without much growth into the solder, perpendicular to the interface until all Cu_6Sn_5 grains contact with each other. The Cu_6Sn_5 grains forming an interfacial layer are separated by grain boundaries between neighboring Cu_6Sn_5. The interfacial layer continues growing by dissolution of the Cu substrate [101-105]. As the interfacial Cu_6Sn_5 grains are separated by grain boundaries, the diffusion of dissolved Cu from the Cu substrate will be controlled by grain boundary diffusion (Fig. 29) which is confirmed by the values of the exponent and activation energy in the empirical power law kinetic equation for the growth of interfacial Cu_6Sn_5 layers [102, 103, 106].

During contact between liquid solder and the Cu substrate, the interfacial Cu_6Sn_5 grains coarsen with time. Coarsening of scallops is a ripening process (i.e. the reduction of interface curvature with time), due to the Gibbs-Thomson effect. Ripening also results in the reduced number of IMC grains/scallops [107]. Qu et al [107] studied the growth of interfacial Cu_6Sn_5 during Sn/Cu isothermal reaction at 350 ℃ using

synchrotron radiation real time imaging and showed that during isothermal reaction, the interfacial grains coalesce. The Gibbs-Thomson effect drives the coalescence/ripening of interfacial grains which are affected by the curvature of neighbouring grains.

Cu substrate dissolution will continue through the isothermal reaction until the mean uniform saturation in the liquid is reached. The Cu flux contributes not only to the formation of interfacial Cu_6Sn_5 grains, but also to the formation of primary Cu_6Sn_5 crystals in the bulk solder [108]. At the same time, the Cu flux may react with the existing Cu_6Sn_5 layer to form a layer of Cu_3Sn between Cu_6Sn_5 layer and the substrate. The growth rate of the Cu_3Sn layer is typically very low and its thickness can often be ignored during reflow and the solidification stages [108]. The reaction equations at the interfaces in a solder joint may be described by the diffusion and the formation of new phases:

at the Cu_3Sn/Cu interface [109]:

$$3Cu+(Sn)\rightarrow Cu_3Sn$$

at the Cu_6Sn_5/Cu_3Sn interface[109]:

$$Cu_6Sn_5+9(Cu)\leftrightarrow 5Cu_3Sn \text{ (interface moves into } Cu_6Sn_5)$$

$$Cu_6Sn_5\leftrightarrow 3(Sn)+2Cu_3Sn \text{ (interface moves into } Cu_3Sn)$$

at the solder/Cu_6Sn_5 interface [109]:

$$5Sn+6(Cu)\rightarrow Cu_6Sn_5$$

where the elements in ( ) are diffusants. Fig. 25 [109] summarises the general diffusion

phenomena in soldering reactions between Sn-xCu solder and Cu substrate where (a) to (c) represent the microstructure development with increasing time.

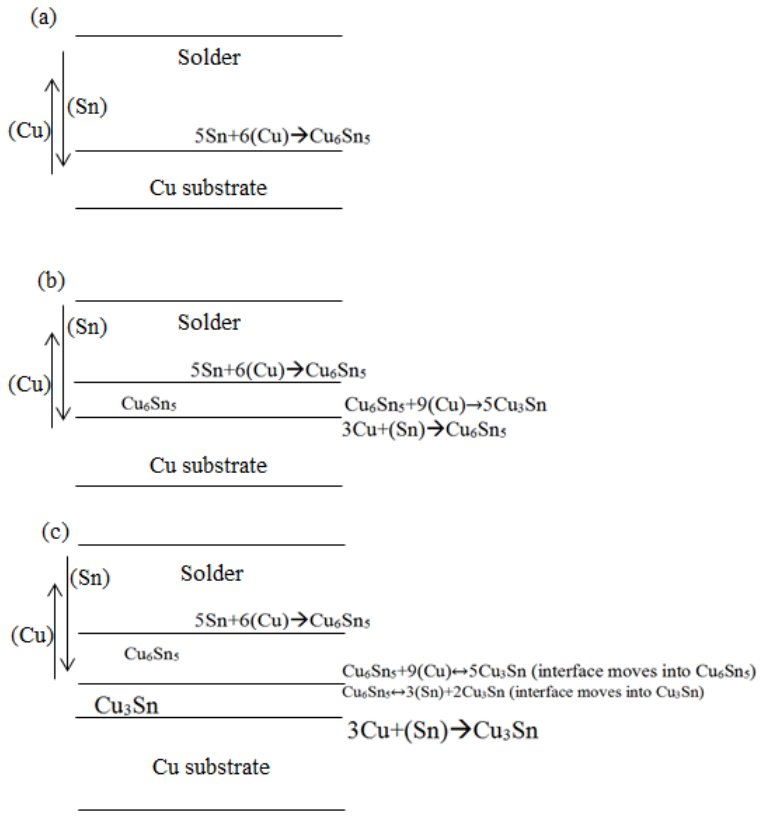


Fig. 25 general interfacial reactions during soldering between Sn-xCu solder and Cu substrate (modified from [109])

The interfacial Cu_6Sn_5 layer is desirable as the metallurgical bonding connecting the solder alloy and the substrate. However, the layer is brittle and there are some property mismatches between the IMC layer, βSn and Cu e.g. coefficient of thermal expansion, Young's modulus etc, Therefore, excessive intermetallic thickness will degrade the solder joint [101, 110-112] and thin IMC layers are desired.

2.3.4.2 Kinetics of interfacial Cu_6Sn_5 growth during soldering

At higher isothermal reaction temperature, as there is higher Cu solubility at higher temperature, or lower cooling rate, there will be more interfacial IMCs precipitated

[108]. Meanwhile, lower cooling rate leads to longer precipitation time and larger interfacial IMCs grains [108]. With longer reflow time, the grain size of interfacial IMCs will increase, while their number will be reduced. Almost all the papers researching interfacial microstructure suggests that the interfacial layer is not a flat layer and interfacial Cu_6Sn_5 grains adopt a scallop morphology, not a layered compound. Meanwhile, a layer of Cu_3Sn may form in between the Cu_6Sn_5 and substrate layers, its growth is a result of consumption of existing Cu_6Sn_5. Therefore, to quantitatively describe the growth kinetics is not easy [102, 113].

Kim et al. suggested a model called flux driven ripening (FDR model) to describe the interfacial Cu_6Sn_5 growth based on the theory schematically drawn in Fig.26 [86]. This model describes the growth and particle size distribution of interfacial Cu_6Sn_5 grains, however only growth will be reviewed here.

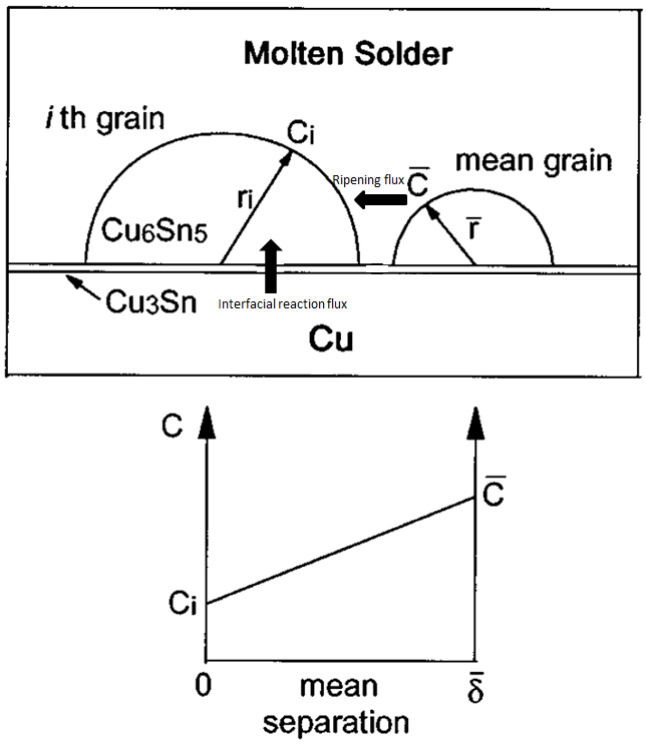


Fig.26 Schematic drawing of an ith Cu_6Sn_5 grain and a mean size Cu_6Sn_5 grain on the interface, and the concentration gradient between them [86].

With longer reflow time, the Cu_6Sn_5 scallops become larger, while the number of them decreases, due to ripening. This ripening is conservative, as the total projected-area of solder/Cu_6Sn_5 interface is considered to be constant but the total volume of the interfacial layer is increasing due to thickening [114]. The ripening of Cu_6Sn_5 scallops is supported by two Cu fluxes: a ripening flux (Fig.26) which is a result of Gibbs-Thomson effect, and an interfacial reaction flux (Fig.26) which is related to the consumption of Cu substrate. The Cu flux will diffuse through the liquid channels between the scallops, which are quick diffusion routes connecting the substrate and the molten solder [114].

The Cu_6Sn_5 scallops are assumed to be hemispheres in the FDR model (i.e. each has constant curvature). From the Gibbs-Thomson effect, the Cu concentration at the liquid/Cu_6Sn_5 interface can be described as [86]:

$$C_r = C_0 \exp\left(\frac{2\gamma\Omega}{rRT}\right) \cong C_0\left(1 + \frac{2\gamma\Omega}{rRT}\right), \text{ if } \frac{2\gamma\Omega}{rRT} \ll 1 \qquad \text{Equation 20}$$

where C_r is the Cu concentration of the liquid at the liquid/Cu_6Sn_5 interface, C_0 is equilibrium concentration of Cu at r=∞in molten solder, γ is the molten solder/Cu_6Sn_5 interfacial energy per unit area, Ω is the molar volume of Cu_6Sn_5, r is the radius of hemisphere, R is gas constant and T is the reflow temperature. Therefore, the Cu concentration at the solder/larger Cu_6Sn_5 scallop interface, C_i, will be lower than that at solder/smaller Cu_6Sn_5 scallops interface $\bar{C}$ (Fig.26), as larger scallop has larger radius (i.e. lower interface curvature). Due to the Cu concentration difference, the Cu flux will diffuse from smaller scallops to the larger scallops leading to ripening.

Comparing the FDR model with Ostwald ripening, the principles are very similar. Considering Ostwald ripening quantitatively, if one sphere with radius r_1 forms in the liquid, then the Gibbs energy associated with one sphere is [71]

$$G = V_s G_s^V + A\gamma \qquad \text{Equation 21}$$

where V_s is the volume of the sphere, G_s^V is the Gibbs free energy associated with unit volume of the sphere, A is the total interfacial area between the sphere and the liquid, γ is the energy per unit interfacial area [71].

$$\mu = \frac{dG}{dn} = \frac{dV_s}{dn} G_s^V + \frac{dA}{dn}\gamma = V_m G_s^V + 2V_m \frac{1}{r}\gamma \qquad \text{Equation 22}$$

where μ is the chemical potential, V_m is the molar volume and r is the radius of the. Assuming there are two spheres with radius r_1 and r_2 $(r_1 < r_2)$ in the liquid. Therefore,

$$\Delta\mu = \mu_1 - \mu_2 = 2V_m\gamma\left(\frac{1}{r_1} - \frac{1}{r_2}\right) \qquad \text{Equation 23}$$

where $\Delta\mu$ is the driving force for Ostward ripening.

Now, considering the concentration associated with the Ostward ripening by using dilute solution and Raoult's law [71]

$$\mu_i = \mu_0 + RTlnC_i \qquad \text{Equation 24}$$

where μ_i is the chemical potential associated with i^{th} sphere having C_i in the liquid at its interface.

$$\Delta\mu = \mu_1 - \mu_2 = RTln\frac{C_1}{C_2} = RTln\left(1 + \frac{C_1 - C_2}{C_2}\right) \approx RT\left(\frac{C_1 - C_2}{C_2}\right) \qquad \text{Equation 25}$$

therefore,

$$RT\left(\frac{C_1 - C_2}{C_2}\right) = 2V_m\gamma\left(\frac{1}{r_1} - \frac{1}{r_2}\right) \qquad \text{Equation 26}$$

Considering r_2 is infinite, so the C_2 is the equilibrium concentration of Cu in the liquid, C_0. Rearranging the equation

$$C_1 = (\frac{2V_m\gamma}{RTr_1} + 1)C_0 \qquad \text{Equation 27}$$

which is same as Equation 20. It suggests that the Cu concentrations in the liquid at interfaces of larger sphere and smaller sphere are different, which can be understood by considering role of curvature undercooling on Gibbs energy versus composition curves and, therefore, the phase diagram in Fig. 27. Since the smaller sphere has larger curvature and larger curvature undercooling than the larger sphere, and the temperature is isothermal, the liquid around the smaller sphere has higher concentration of Cu (C_1). Therefore, a Cu flux will flow from the smaller sphere to the larger sphere and the smaller one will finally disappear, while the larger one will grow.

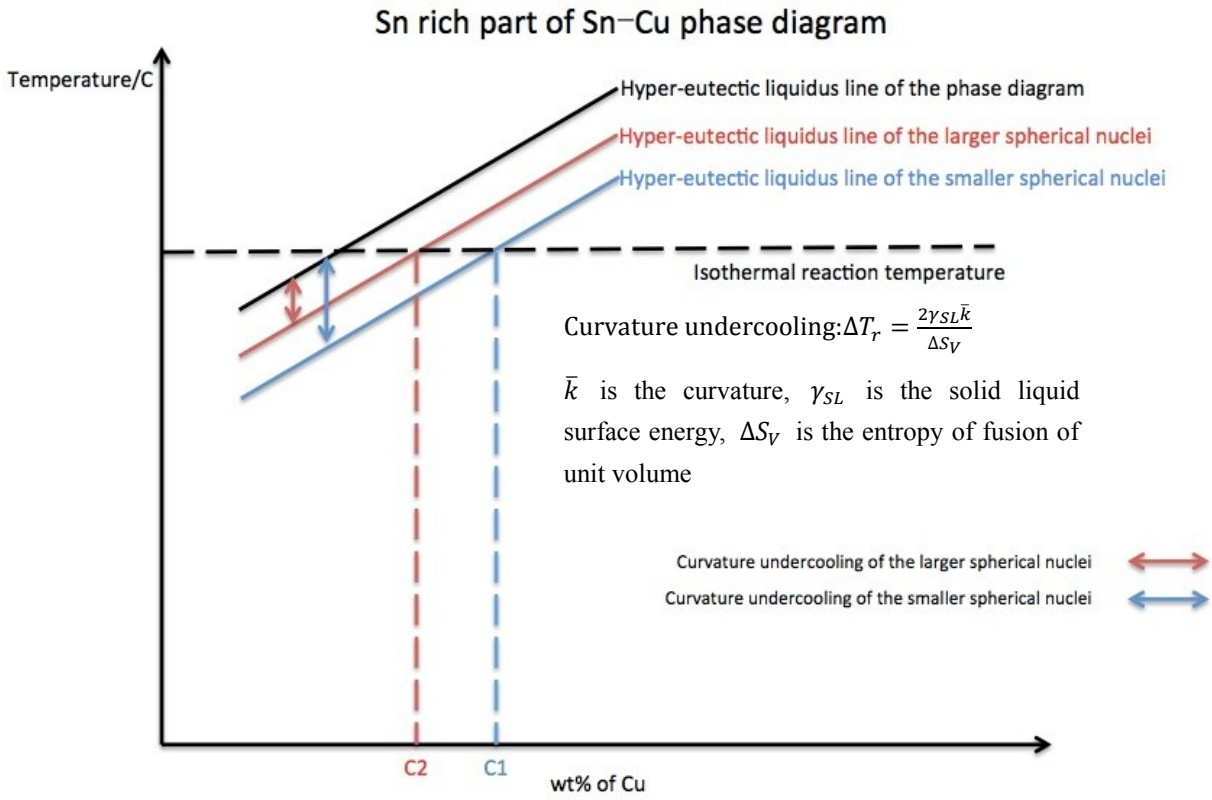


Fig. 27 effect of different curvature undercoolings on the corresponding composition at isothermal reaction temperature

Comparing FDR model with secondary dendrite arms coarsening, the theory is similar as well. If the spacing between the primary arms is enough, the solute fields associated with primary arms will not overlap and, therefore, secondary arms or even more sub-sidebranches from the secondary arms will develop [70, 83]. The secondary arms will grow depending on the thermal and solutal influence. During their growth, when the solutal fields of the secondary arms touch each other, those secondary arms will not grow and some of them will ripen, with some being eliminated. Fig. 28 [83] shows fully developed dendrites during directional solidification and selected neighboring secondary arms.

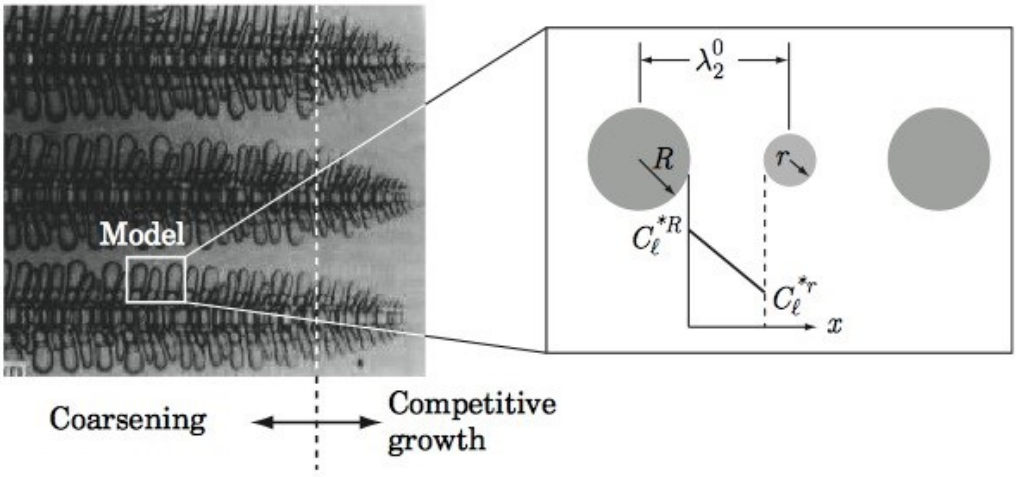


Fig. 28 dendrites formed during directional solidification (left), neighboring secondary arms in the white box and composition gradient between them [83].

In summary, the fundamentals for the FDR model, Ostward ripening and secondary dendrite arm coarsening is similar. In each case, the difference in curvature at different positions of the solid-liquid interface induces composition differences at interfaces and drives diffusion from regions of high to low curvature. This causes curved regions to shrink and low-curvature regions to grow.

Now, returning to the FDR model, and considering steady state diffusion:

$$J_{ripening} = -D\frac{dC}{dx} = -D\frac{\bar{C} - C_i}{\delta} \qquad \text{Equation 28}$$

where δ is the average separations between adjacent scallops and D is the Cu diffusivity in liquid solder. From Equation 20:

$$\bar{C} - C_i = \frac{2\gamma\Omega C_0}{RT}\left(\frac{1}{\bar{r}} - \frac{1}{r_i}\right) \qquad \text{Equation 29}$$

substituting Equation 29 into Equation 28:

$$J_{ripening} = -\frac{2\gamma\Omega DC_0}{RT}\frac{1}{\delta}\left(\frac{1}{\bar{r}} - \frac{1}{r_i}\right) \qquad \text{Equation 30}$$

as δ is smaller than the average scallop radius $\bar{r}$, it can be described as $\delta = L\bar{r}$, where $0 < L < 1$. Substituting this into Equation 30:

$$J_{ripening} = -\frac{2\gamma\Omega DC_0}{RTL}\frac{1}{\bar{r}}\left(\frac{1}{\bar{r}} - \frac{1}{r_i}\right) \qquad \text{Equation 31}$$

a typical radius value for a large size scallop is $r_i = \frac{3}{2}\bar{r}$ [86], substituting this into Equation 31:

$$J_{ripening} = \frac{2\gamma\Omega DC_0}{3RTL}\frac{1}{\bar{r}^2} \qquad \text{Equation 32}$$

To determine the Cu atom flux due to the interfacial reaction, it is assumed that the total amount of Cu flux through the channel from the substrate to the molten solder equals to the total consumption of Cu substrate:

$$\rho A\Delta h = \frac{m}{N_A}\int J_{total}\,dt \qquad \text{Equation 33}$$

where ρ is the density of Cu, A is the total area of the joint, Δh is the thickness of consumption of Cu substrate, m is the molar mass of Cu, N_A is Avogadro's number, J_{total} is the total flux of Cu though the liquid channels. The total Cu flux can be calculated as:

$$J_{total} = \rho \frac{N_A}{m} Av \qquad \text{Equation 34}$$

where $v = \frac{dh}{dt}$ is the consumption rate of the Cu substrate. Then the Cu flux diffusing into a scallop with average size is described as:

$$J_{IR} = \frac{J_{total}}{2\pi \bar{r}^2 N_P} = \frac{\rho N_A A v(t)}{2\pi m N_P(t)} \frac{1}{\bar{r}^2} \qquad \text{Equation 35}$$

where N_p is the total number of scallops on the interface, and N_p and v are functions of time.

The growth of scallops is the combined effects of the ripening and interfacial reaction fluxes. By using Gauss's theorem, the growth of scallops can be described as [86]:

$$r^3 = \int \left(\frac{\gamma \Omega^2 D C_0}{3 N_A R T L} + \frac{\rho A \Omega v(t)}{4\pi m N_P(t)}\right) dt \qquad \text{Equation 36}$$

Tu has published a method to determine the Cu consumption rate [113]. First, it is assumed that the total consumption of Cu equals to the total Cu contained in molten solder and in the intermetallics:

$$\Delta h = \frac{1}{\rho_{Cu} A} (n V_L \rho_L + f_{Cu} \rho_c V_c) \qquad \text{Equation 37}$$

where n is the weight percentage of Cu in molten solder, V is the total volume of molten solder, f_{Cu} is the weight percentage of Cu in intermetallics and V_c is the total volume of the intermetallics. During soldering, upon contacting with molten solder, Cu atoms will dissolve into it and the saturation will quickly be reached in the molten solder,

therefore, further consumption of Cu substrate will be influenced by the volume change of the intermetallics:

$$v(t) = \frac{dh}{dt} = \frac{f_{Cu}\rho_c}{\rho_{Cu}A}\frac{dV_c}{dt} \qquad \text{Equation 38}$$

In Kim and Tu's FDR model, the scallop Cu_6Sn_5 is assumed to have a hemisphere morphology, and the scallops growth controlled by ripening flux, which is derived by Gibbs-Thomson effect, and interfacial reaction flux of Cu diffusing from the substrate to the molten solder through the liquid channels between adjacent scallops. The model suggests scallop radius r depends on the cube root of the time, which Tu suggested means the growth of Cu_6Sn_5 grains is controlled by volume diffusion of Cu atoms in the molten solder [86]. The FDR model assumes liquid channels connecting the substrate and the molten solder which is an example in very short reflow times [106]. Shaefer et al. suggested a continuous thin Cu_6Sn_5 scallop layer along the interface would form around 10s. There are deep channels in between the scallops in the interfacial layer. Those channels do not connect the substrate and the molten solder, and are considered to be associated with the grain boundaries of the Cu_6Sn_5 scallops. Therefore the growth of the interfacial layer is controlled by diffusion of Cu from substrate through grain boundaries between Cu_6Sn_5 scallops [106]. The interfacial Cu_6Sn_5 grains are separated by grain boundaries instead of liquid channels through the interfacial layer is supported by Tu et al. as well [103].

Shaefer et al. developed a model for Cu_6Sn_5 scallop growth controlled by grain boundary diffusion [106]. The Cu_6Sn_5 scallop is assumed to adopt an equiaxed scallop, which means d≈ X_{ave}(Fig. 29).

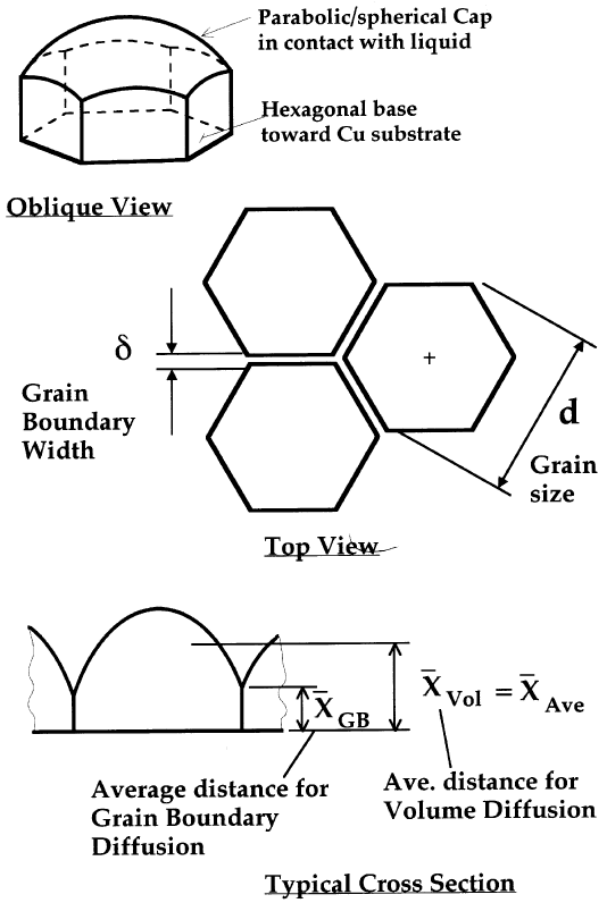


Fig. 29. Schematic representation of equiaxed Cu_6Sn_5 scallop [106]

The total flux for interfacial layer growth consists of a grain boundary flux through the grain boundary and a volume flux through the bulk Cu_6Sn_5 grain. By using one dimensional diffusion equation, the equation for volume diffusion is:

$$J_{vol} = -D_{vol}\frac{\Delta C}{X_{ave}} \qquad \text{Equation 39}$$

the equation for grain boundary diffusion is:

$$J_{gb} = -D_{gb}f\frac{\Delta C}{X_{aveGB}} \qquad \text{Equation 40}$$

where f is the fraction of available grain boundary areas for diffusion, and $f = \frac{\delta}{\sqrt{3}d}$ [106], δ is the grain boundary width and d is the grain size (Fig. 29). The calculation of f is described in Fig. 30:

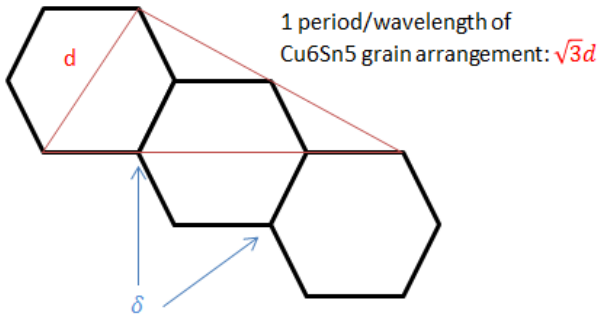


Fig. 30 schematic drawing of how to calculate f, the fraction of available grain boundary area for grain boundary diffusion

The length for one period of Cu_6Sn_5 hexagonal arrangement in one row is $\sqrt{3}d$ (Fig. 30). This period contains two grain boundaries, however, the middle scallop shares these two grain boundaries with two neighbouring scallops, therefore, the available grain boundary area in this period is one. Therefore, the fraction of available grain boundary in each period is $\frac{\delta}{\sqrt{3}d}$, which is same for the total available grain boundary fraction.

So the total flux of Cu is:

$$J_t = -(D_{vol}\frac{\Delta C}{X_{ave}} + D_{gb}\frac{\delta}{\sqrt{3}d}\frac{\Delta C}{X_{aveGB}}) \qquad \text{Equation 41}$$

if grain boundary grooving, which is due to thermodynamics, is fast enough, then the wetting angle between neighbouring grains and the shape of equiaxed scallop will be constant, only the volume of scallop increases, then the ratio between average grain boundary diffusion distance and the average volume diffusion distance will remain, which is

$$r = \frac{X_{aveGB}}{X_{ave}} \qquad \text{Equation 42}$$

with smaller grain size, d, the total and available grain boundary areas for diffusion will increase or with deep grain boundary groove, the grain boundary diffusion distance will be shorter, the grain boundary diffusion will strongly promoted [106], and in those conditions, the volume diffusion could be negligible. Therefore by substituting Equation 42 into Equation 41:

$$J_t = -D_{gb}\frac{\delta}{\sqrt{3}d}\frac{1}{r}\frac{\Delta C}{X_{ave}} \qquad \text{Equation 43}$$

as equiaxed scallop morphology is assumed, then $d \approx X_{ave}$, substituting in to Equation 43:

$$J_t = -D_{gb}\frac{\delta\Delta C}{\sqrt{3}r}\frac{1}{{X_{ave}}^2} \qquad \text{Equation 44}$$

beside proportional to the total flux of Cu, the growth and growth rate of the interfacial layer is also proportional to the volume of Cu_6Sn_5 scallop formed, V_{IMCs}, per mole of dissolved Cu, the growth rate is proportional to:

$$\frac{dX_{ave}}{dt} \propto -D_{gb}V_{IMCs}\frac{\delta\Delta C}{\sqrt{3}r}\frac{1}{{X_{ave}}^2} \qquad \text{Equation 45}$$

integral Equation 45:

$$Xave^3 \propto -D_{gb}V_{IMCs}\frac{\delta\Delta C}{\sqrt{3}r}t + X_{ave,t=t_{initial}}$$

a more accurate solution involves integral from the initial layer thickness at initial time, $t_{initial}$, to the thickness when a continuous interfacial layer is formed during about 10s, with thickness a few tenths of a micron [106]. Now, takng $X_{ave,t=t_{initial}} = 0$:

$$Xave \propto -(D_{gb}V_{IMCs}\frac{\delta\Delta C}{\sqrt{3}r})^{\frac{1}{3}}t^{\frac{1}{3}} \quad \text{Equation 46}$$

therefore, the growth of intermetallic layer, which is controlled by grain boundary diffusion, has a $t^{\frac{1}{3}}$ dependence. The limitation of the derivation is that the scallops are assumed to have uniform size. An empirical Power law equation is commonly used for describing the thickness of interfacial layer:

$$X(t,T) = K_0\exp(\frac{-Q}{RT})t^n \quad \text{Equation 47}$$

where K_0 is growth constant, n is an exponent and Q is the activation energy of growth. If the interfacial layer growth is controlled by grain boundary diffusion, then n should adopt a value around 1/3.

The data from a range of researchers are summarsied in Table.3. It is clear that there is significant deviation from the n=1/3. Shaefer et al. [106] suggested that the deviation could be the result from the change in dominant diffusion mechanisms. With longer reflow time, the interfacial Cu_6Sn_5 grains grow larger, then the total grain boundary areas will reduce, so the transport of Cu atoms may deviate from grain boundary domination and a different exponent value will appear. Quantitatively, r in Equation 42 is a function of grain size instead of a constant value [106]:

$$r = r'X_{ave} \quad \text{Equation 48}$$

where r' is ratio, substitute Equation 48 into Equation 42-Equation 46:

$$Xave \propto -(D_{gb}V_{IMCs}\frac{\delta\Delta C}{\sqrt{3}r'})^{\frac{1}{4}}t^{\frac{1}{4}} \quad \text{Equation 49}$$

In Equation 49, the interfacial layer growth has $t^{\frac{1}{4}}$ dependence.

Some data of exponent values for growth are summarized in Table 3 All the solder joints are on Cu substrates.

Table 3 Reported growth exponent values for different alloy systems on Cu substrate

Alloy system	n	Ref
Cu_6Sn_5 layer of Sn-3.5Ag	0.326→0.456 (240℃) 0.37→0.461 (280℃)	[115]
Cu_6Sn_5 layer of Sn	0.317→0.481 (240℃) 0.357→0.472 (280℃)	
Cu_3Sn layer of Sn-3.5Ag	0.403 (240℃) 0.485 (280℃)	
Cu_3Sn layer of Sn	0.478 (240℃) 0.499 (280℃)	
Cu_6Sn_5 layer of Sn	0.5	[98]
Cu_6Sn_5 layer of SnAgCu	0.47	
Cu_6Sn_5 layer of SnCu	0.35	
$Sn/Cu_{(011)}$	0.3 (scallop)	[89]
$Sn/Cu_{(123)}$	0.31 (scallop)	
$Sn/Cu_{(001)}$	0.24 (prism)	
$Sn/Cu_{(111)}$	0.19 (prism)	
Sn-36wt%Pb-2wt%Ag	0.25	[106]
SnAgCu	0.25~0.32	[116]
Sn-36wt%Pb-2wt%Ag	0.25	[117]
SnCu	0.21 (513K) 0.25 (573K)	[118]
Sn	0.291 (250℃ dipping 1min) 0.259 (250℃ dipping 5min)	[107]

Zou et al [98] studied the Sn-3wt%Cu and pure Sn on Cu substrate with four reflow temperatures: 240℃, 260℃, 280℃, and 300℃, showing that IMCs in Sn-3wt%Cu/Cu coarsen with mean radius proportional to the cube root of reflow time, while for IMCs

in pure Sn on Cu joint (Sn/Cu), they coarsen with square root relationship. Furthermore, their results show that for higher Cu concentration solder, the nucleation rate of interfacial IMCs grain will be higher as activation energy for the formation of critical IMC grains can be reduced by higher Cu content. They concluded that if the Cu concentration in the solder alloy is higher than the solubility under certain temperature according to phase diagram e.g. Sn-3wt%Cu, the mean radius of interfacial IMCs grains has cube root relationship to the reflowing time which follows FDR model. If the Cu concentration is lower than the solubility e.g. pure Sn, the mean radius will have square root relationship with reflowing time [98].

Yang et al [115] studied the interfacial reactions of pure Sn with Cu substrate during isothermal reaction with temperature 240±2℃ and 280±2℃. They found that during isothermal reaction, the average thickness of interfacial IMCs layer can be calculated as Kt^n, where K is the growth rate constant, t is the isothermal reaction time, and n is the exponent. In this research, n for the growth of Cu_6Sn_5 layer at the beginning is ~1/3, however, after 30 minutes is ~1/2, which means the Cu_6Sn_5 layer growth is initially dominated by grain boundary diffusion but change to volume diffusion control [103, 115]. With the same method, they also determined that the growth of the Cu_3Sn layer is controlled by volume diffusion at all times.

Zou et al. [89] studied pure Sn soldered on Cu single crystal substrate, and their relationship between Cu_6Sn_5 grain size and reflow time is: $r=Ct^k$, where r is the grain

size, t is the reflow time, C and k are constant [89]. They found that the orientation of Cu single substrate facing the molten solder/Cu_6Sn_5 morphology may affect the growth mechanism/kinetics with evidence of different k values. For (001) and (123), k values are 0.31 and 0.3 which is ~1/3, while for (001) and (111), k values are 0.19 and 0.24. The effect of interfacial Cu_6Sn_5 morphologies on the reaction kinetics is also mentioned by Suh et al [111]. Beside the orientation, they found that the interfacial morphology is also dependent on the composition [111]. Suh and Tu et al [99] suggested that the scallops would become more faceted if the compositions move away from the eutectic point, by comparing pure Sn with lead-containing solder alloys.

2.3.5 Growth and morphology of primary Cu_6Sn_5 in liquid solder

The dissolution of the Cu substrate into the liquid commonly moves the liquid to a hypereutectic composition which leads to primary Cu_6Sn_5 forming in the bulk solder during solidification. The primary Cu_6Sn_5 can play an important role solder joint reliability [12, 119-122] due to its size, morphology and growth direction [49, 67, 123]. Fig. 31 summarises the different reported morphologies of primary Cu_6Sn_5 from the literature.

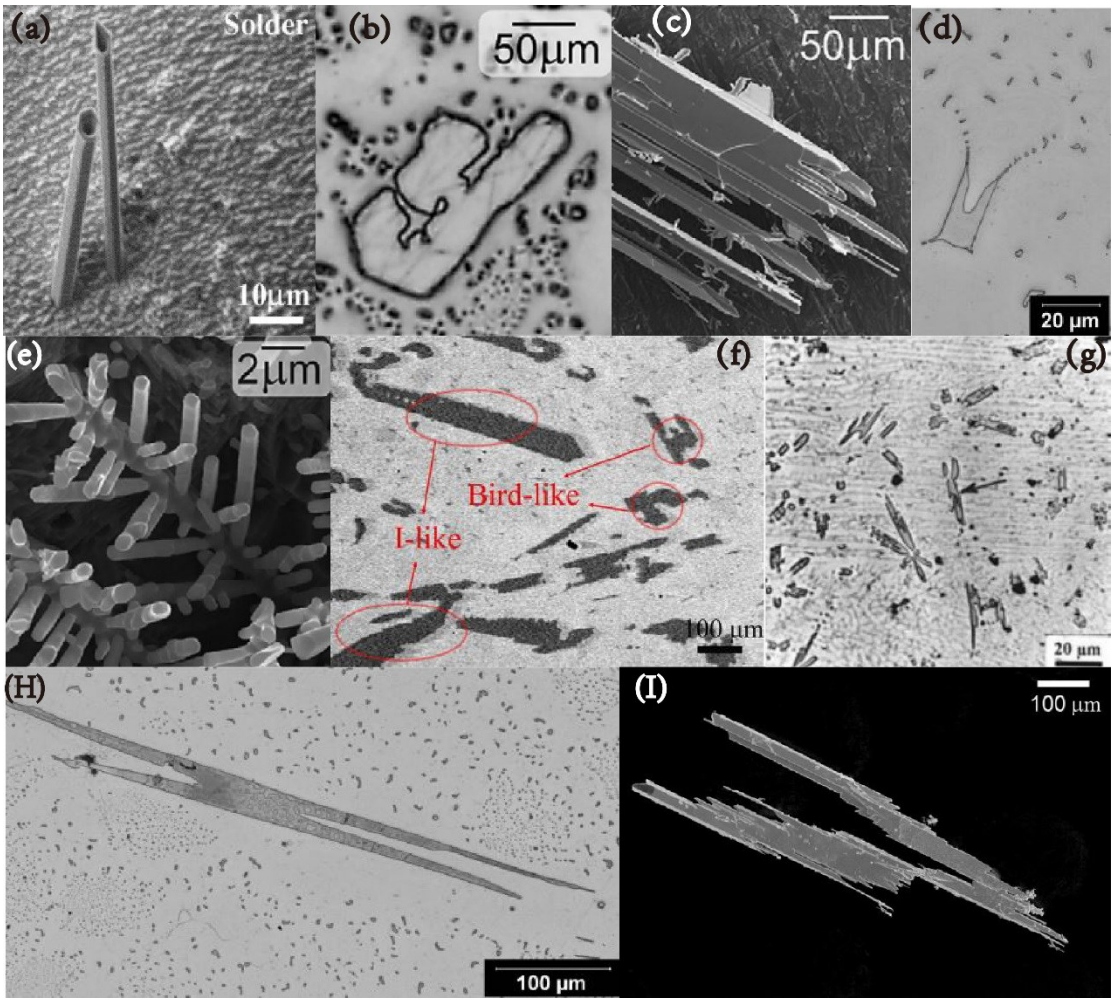


Fig. 31 different primary Cu_6Sn_5 morphologies in 2D and 3D (a) hexagonal rods [49] (b) grooved rod [11] (c) in-plane branched facets [11] (d) 'v'-shape [124] (e) dendrite [11] (f) 'I'-shape, 'bird'-shape [20] (g) 'X'-shape [125] (H) 'H'-shape [124] (I) 'Y'-shape [13]

Table 4 summarizes different morphologies of primary Cu_6Sn_5 from different researches with the order of increasing Cu content.

Table 4 different morphologies of primary Cu_6Sn_5.

Sample	**Processing**	**Cooling/pulling rate**	**Morphology**	**Reference**
Sn-0.7Cu-0.1Ni	DS	2-20μm/s	Hexagonal rods 'v','H'-shape	[124]
Sn-0.7Cu-0.06Ni	DS	~16 μm/s	Hexagonal rods	[28]
Sn-0.7Cu	DSC	~0.03K/s	Hexagonal rod	[11]
Sn-0.7Cu			hollow rods	[126]
Sn-0.89Cu	DSC	~0.03-3.5K/s	Hexagonal rod to in-plane	[11]

			branched facets	
Sn-1Cu	DSC	~0.167k/s	rods	[120]
Sn-1.1Cu	DSC, furnace casting	~0.03-3.5K/s	Grooved rod to in-plane branched facets	[11]
Sn-2Cu ~ 208Cu	DS	18K/s	Dendrite, 'H'-shape	[127]
Sn-2.3Cu	DSC, furnace casting, water quench	~0.03-100K/s	Grooved rod, In-plane branched, dendrite	[11]
Sn-4Cu-0.05Ni	DS	~16.6 μm/s	Hexagonal rods 'H'-shape	[123]
Sn-4Cu-0.05Ni	casting	0.84k/s	dendrite	[12]
Sn-4.2Cu	DSC, furnace casting, water quench	~0.03-100K/s	In-plane branched, dendrite	[11]
Sn-6.9Cu-2.9Ag	casting	~3K/s	dendrite	[128]

*DS means directional solidification

From Table 4，generally it can be seen that the Cu content and the cooling rate/pulling rate will influence the primary Cu_6Sn_5 in a way that with increasing of both, the morphology of primary Cu_6Sn_5 will develop more larger curvature features i.e. from facets e.g. hexagonal rods to grooved rods e.g. 'M'-shape then finally to dendrites. However, there is no comprehensive research focusing on the role of reflow soldering parameters i.e. peak temperature, cooling rate and Cu content, on primary Cu_6Sn_5 morphology.

Beside the morphology, the growth directions of primary Cu_6Sn_5 have been studied as summarized in Table 5 for different morphologies.

Table 5. Growth directions of different morphologies primary Cu_6Sn_5

Composition	**Morphology**	**Growth direction**	**Reference**
Sn-0.7Cu	Hollow faceted rods	[0001]	[11, 126]
Sn-4.2Cu	In-plane branched	[0001]	[11]
Sn-4Cu Sn-2.3Cu	Nonfaceted dendrites	Dendrite arms along <405>	[11]

		Ten possible secondary arm directions	
Sn-4Cu-0.05Ni	Faceted grooved 'H' shape rods	[0001]	[123]

As stated previously, it has been found that the size of primary Cu_6Sn_5 will influence the reliability, and in general the smaller size will improve the mechanical properties. Some trace elements and external reinforcements have been found to be useful for reducing the size of Cu_6Sn_5 as summarized in Table 6.

Table 6 The influence of trace elements and external reinforcement on IMCs size and morphology

Element addition	**Solder composition**	**substrate**	**Primary Cu_6Sn_5 Size&Morphology**	**Ref**
Ni (~0.05wt%Ni)	Sn-0.7wt%Cu	Cu	Smaller size Large long rod to flake like	[91]
Ni (0.05, 0.1wt%)	SAC0507	-	$(Cu,Ni)_6Sn_5$ forms, finer and uniform distributed IMCs	[16]
Ni (0.05, 0.1wt%)	SAC305	-	Form rod-shaped $(Cu,Ni)_6Sn_5$	[15]
Al (0.25-0.2wt%)	Sn-4wt%Cu SN100C	-	Primary Cu_6Sn_5 from large faceted dendrite to compact polyhedrons with small branching	[12]
Al (0.02, 0.2wt%)	Sn-4Cu	-	Density of Cu_6Sn_5 increased ~8 times, and the branching size much smaller	[13]
Al (0.05wt%)	Sn-0.7Cu	Cu	~4 times smaller	[9]
La (0.06wt%)	Sn-6.5wt%	-	The size more uniform, I-shape and bird-shape to Y-shape	[20]

SiC (0.7wt%)	SAC305	-	Reduce the IMCs size	[21]
Al_2O_3 (0.25-1wt%)	SAC305	-	Ag_3Sn size reduced, eutectic area increased	[24]
TiO_2	Sn-0.7wt%Cu	Cu	Suppress primary Cu_6Sn_5 growth	[25]
TiO_2 (0.25-1wt%)	Sn-0.7wt%Cu	-	Refine Cu_6Sn_5 size and increase eutectic fraction	[26]

2.4 Role of intermetallic compounds in the fracture of solder joints

The fracture of Sn-xwt%Cu/Cu solder joints through the bulk solder involves the fracture of primary Cu_6Sn_5 by cleavage and the ductile tearing of βSn matrix. This section contains a brief background on cleavage fracture, ductile tearing, the fracture behavior and the role of solder intermetallics i.e. primary Cu_6Sn_5 and Ag_3Sn on the mechanical property of solder joint.

2.4.1 Fracture classification and cleavage fracture

The fracture processes can be categorized according to several different aspects due to the their appearances and failure mechanisms etc [129]. Macroscopically, the fracture mechanisms can be classified from stress state or crack progression i.e. loading types, orientations of crack relating to the principal stresses, crack stability, rate of crack growth etc. [129]. Microscopically, the various fracture mechanisms will result in and can be characterized from different fracture surfaces. The fracture types can be cleavage fracture whose fracture surface is normally flat with little deformation, intercrystalline/trancrystalline fracture, dimple fracture/ductile fracture, fatigue fracture and creep fracture etc.[129]. Various fracture types were summarized in Fig. 32.

Cleavage is a typical mechanism of brittle fracture, during which the atoms are separated on the certain fracture plane (normally low energy plane [130]) with an extremely fast speed which is comparable to sound speed [131]. The cleavage fractures in metallic materials usually leave steps which are resulted from interactions between crack tip with dislocation tangles or twins, giving typical river marking morphology

[131]. The analysis of cleavage fracture can be approached from two aspects: energy and stress intensity which are briefly discussed.

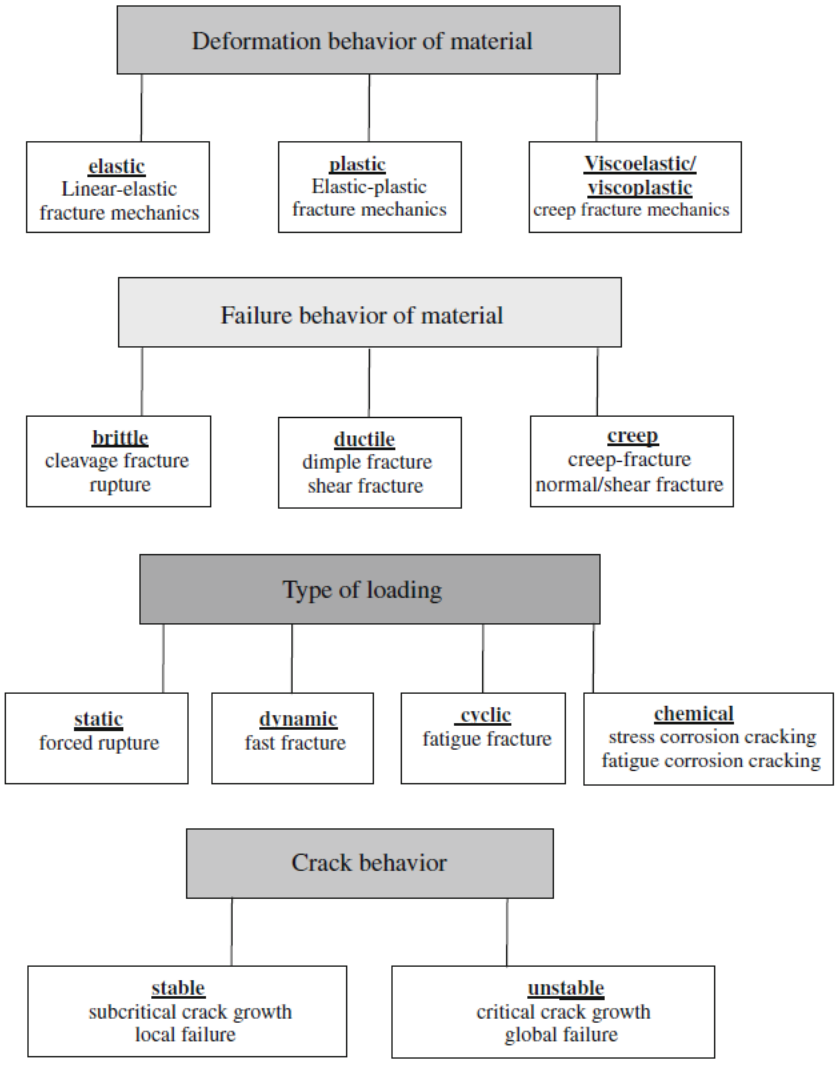


Fig. 32 Different types of fracture [129]

2.4.1.1 Energy criterion approach

The cleavage fracture process can be analyzed by using Griffith's energy balance analysis [130-136] and the modern version of the energy criterion involving the energy release rate is proposed by Irwin [137]. The criterion describes that in order for a crack to growth, the energy available is required to overcome the resistance i.e. surface energy

created, plastic work etc. Considering an infinite wide plate containing crack having length 2a and has been applied a remote tensile stress Fig. 33

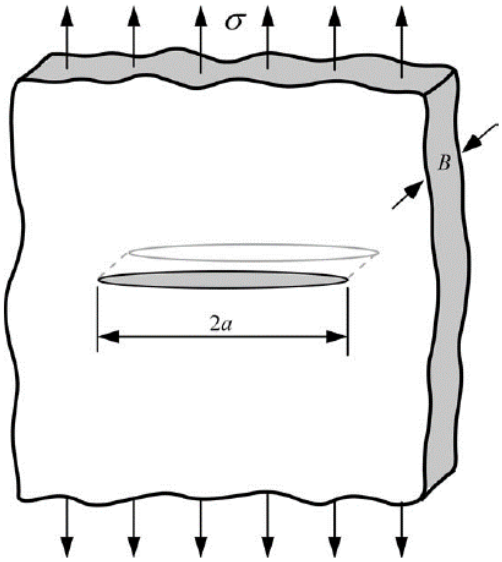


Fig. 33 infinite plate under remote tensile stress, containing through thickness crack [134]

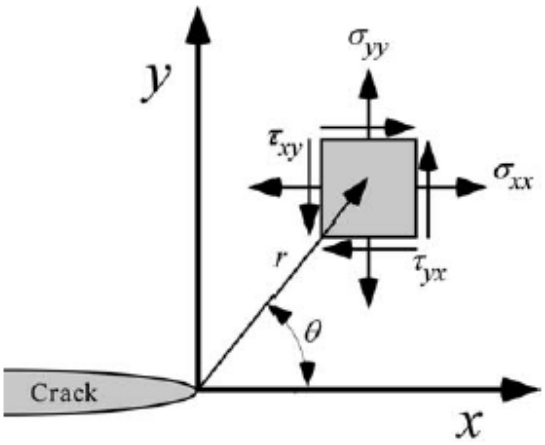
by adding up all the energy contributions i.e. energy applied, surface energy, plastic work and differentiate the total energy change, the fracture stress and critical energy release rate can be related to the crack size a:

$$G_c = \frac{\pi \sigma_f^2 a}{E} \qquad \text{Equation 50}$$

where G_c is critical energy release rate, σ_f is fracture stress, E is Young's modulus and a is half crack length. The energy release rate G is defined as potential energy change with respect to the crack area and it is the driving force of fracture, while G_c is the resistance to fracture and is one way of representing the fracture toughness [134].

2.4.1.2 Stress Intensity approach

The stress elements around a crack tip is schematically depicted and described by equations in Fig. 34.



$$\sigma_{xx} = \frac{K_I}{\sqrt{2\pi r}}\cos\left(\frac{\theta}{2}\right)\left[1-\sin\left(\frac{\theta}{2}\right)\sin\left(\frac{3\theta}{2}\right)\right]$$

$$\sigma_{yy} = \frac{K_I}{\sqrt{2\pi r}}\cos\left(\frac{\theta}{2}\right)\left[1+\sin\left(\frac{\theta}{2}\right)\sin\left(\frac{3\theta}{2}\right)\right]$$

$$\tau_{xy} = \frac{K_I}{\sqrt{2\pi r}}\cos\left(\frac{\theta}{2}\right)\sin\left(\frac{\theta}{2}\right)\cos\left(\frac{3\theta}{2}\right)$$

Fig. 34 stress elements around crack tip [134]

Each stress element is proportional to stress intensity factor, K_I, characterizing the conditions around crack tip and is defined as:

$$K_I = Y\sigma\sqrt{\pi a} \qquad \text{Equation 51}$$

where Y is compliance representing the geometry, σ is applied stress and a is the half length of crack. The fracture occurs at the critical stress intensity, K_{IC}. In this case, the fracture driving force is K_I while the K_{IC} represents the resistance for fracture it is another way of representing fracture toughness [134]. The energy release rate and stress intensity factor can be linked by:

$$G = \frac{K_I^2}{E} \qquad \text{Equation 52}$$

$$G = \frac{K_I^2}{E}(1-v^2) \qquad \text{Equation 53}$$

where v is Poisson's ratio. Equation 52 is for the plane stress while Equation 53 is for the plane strain [130, 133]. G_c and K_{IC} have the same relations, and the both approaches towards the fracture mechanism are equivalent.

2.4.1.3 Other approaches

The above two approaches can well explain the linear elastic fracture mechanics or

in the case that the deformation is limited in a very small area around the crack tip in nonlinear material. Generally, for nonlinear materials fracture can be analyzed by elastic-plastic fracture mechanics in which two parameters crack tip opening displacement and J contour integral are used to depicted the conditions at crack tip. They can be treated as fracture criterion and measurements for fracture toughness with less limited applications than linear elastic fracture mechanics have [134].

2.4.2 Ductile tearing

If a ductile metal e.g. βSn is loaded under room temperature, it can undergo heavy plastic deformation. A crack in βSn is a stress concentrator, if the loading is sufficiently high, then the fracture will take place, starting at the crack tip. After fracture, the fracture surface of βSn is very rough due to the large amount of plastic work that has taken place. The process above is the ductile tearing in βSn.

Microscopically, the stress very close to the crack is [138]:

$$\sigma_{local} = \sigma + \sigma\sqrt{\frac{a}{2r}}$$

where a is the half length of the crack, r is the distance from the crack tip. σ_{local} is larger than the mean stress applied to the material and the closer to the crack tip (smaller r), the σ_{local} increases. The plastic deformation will occur if the local stress reaches the yield stress ($\sigma_{local} = \sigma_y$). In this case, and if r is much smaller than a:

$$\sigma_y = \sigma\sqrt{\frac{a}{2r}}$$

so

$$r_y = \frac{\sigma^2 a}{2\sigma_y^2} = \frac{K^2}{2\pi\sigma_y^2}$$

where $K = Y\sigma\sqrt{\pi a}$, and $K = K_c$ the fast fracture will happen (Fig. 35 [138]).

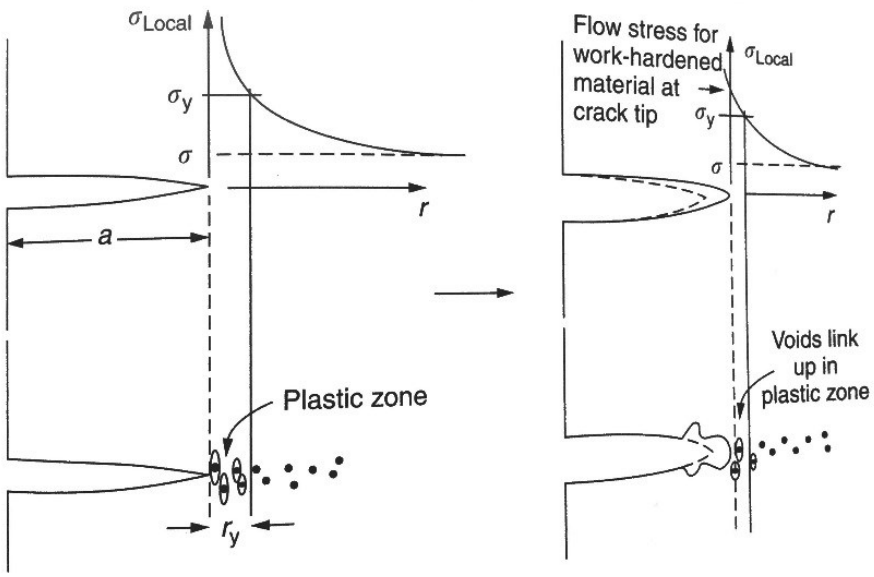


Fig. 35 schematic drawing of stress propagation by ductile tearing [138]

With increasing of yield stress, the plastic zone, r_y, decreases quickly [138]. Soft metals e.g. βSn has a large plastic zone.

Impurities or inclusions will always be present in metals or alloys due to chemical reactions and the cavities around these inclusions will propagate until they coalesce leading to the macroscopic propagation of the crack (Fig. 35) [138]. The process is ductile tearing.

The plastic deformation associated with ductile tearing expends a large amount of energy, and the larger plastic zone, r_y, the more energy will be absorbed which means the material property K_c is very high [138], so ductile materials are very tough.

2.4.3 Fracture of primary Cu_6Sn_5 and its influence on the solder joints

The role of primary Cu_6Sn_5 crystals on the tensile properties and fracture mechanism of solder has been shown to depend on the temperature by Frear et al. [50] who studied 60Sn-40Pb solder on Cu joint containing primary Cu_6Sn_5 with hexagonal hollow rod

morphology (Fig. 36 [50]) and 60Sn-40Cu without intermetallics.

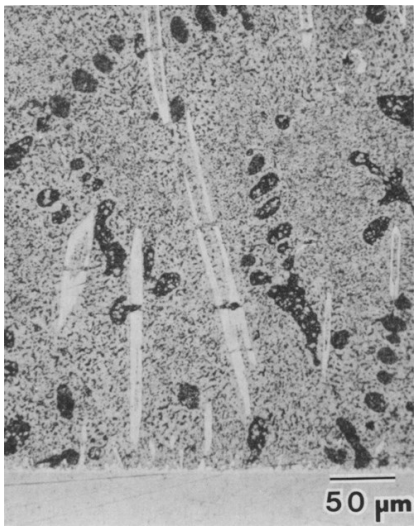


Fig. 36 the primary Cu6Sn5 rod, with hollow rod morphology in 60Sn-40Pb/joint [50]

Fig. 37 [50] presents the stress strain curves for 60Sn-40Pb with and without primary Cu_6Sn_5 and the corresponding fracture surface of 60Sn-40Pb with primary Cu_6Sn_5. At -196℃, the ultimate strengths (UTS) are very close (~130MPa), the work hardening rate for sample with primary Cu_6Sn_5 is much higher while the elongation reduced a lot. The fracture of sample without primary Cu_6Sn_5 is purely ductile, while for the sample with primary Cu_6Sn_5 interfacial separation between Sn and primary Cu_6Sn_5 occurred due to harder mass flow of solder and pile up of dislocation at the interface. At room temperature 20℃, the sample with primary Cu_6Sn_5, which undergone cleavage fracture and acted as crack nucleation sites, has higher UTS (~45MPa) than that without primary Cu_6Sn_5. At 125℃, the tensile behaivour for two samples are very similar, while the fracture behavior of the sample with intermetallics is ductile with only few primary Cu_6Sn_5 on the fracture surface which means at this temperature level, the primary Cu_6Sn_5 only had very little influence on the fracture [50].

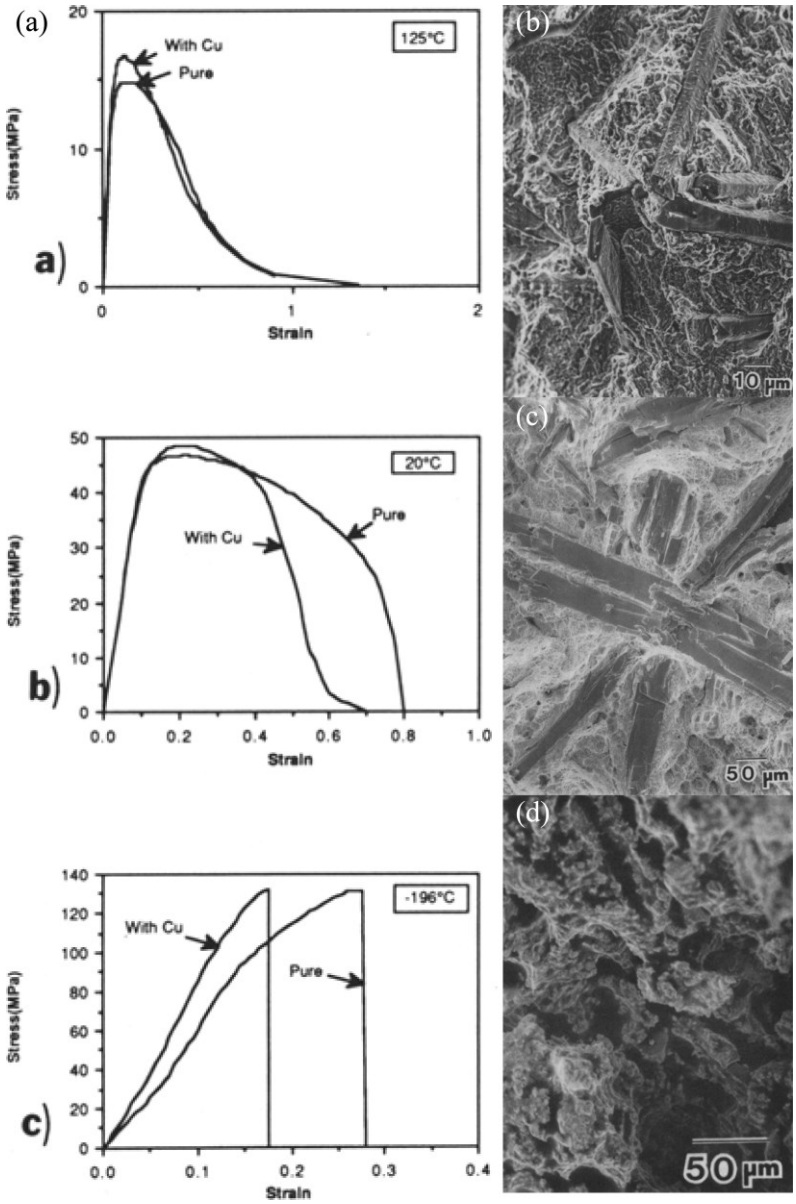


Fig. 37 (a) stress-strain curves for 60Sn-40Pb with and without intermetallics at -196,20,125℃. SEM fractographs of 60Sn-40Pb with intermetallics at (b)-196℃ (c) 20℃ and (d)125℃ (modified from [50]).

At room temperature, the cleavage of the primary Cu_6Sn_5 is important to the fracture of the solder. Fundamental studies have been carried out by several researchers. Jiang et al. used nanoindentation with a flat tip to research the fracture of single crystal Cu_6Sn_5 which was made by focused ion beam milling and they found that there are severel strain bursts on the stress-strain curves, indicating the cleavage of Cu_6Sn_5

occurred on several planes Fig. 38 [139]. This implies that the cleavage fracture has preferences to initiate on certain Cu_6Sn_5 crystal orientations. Meanwhile, from the stress-strain curve it can be seen that Cu_6Sn_5 deformed elastically at the beginning before cleavage.

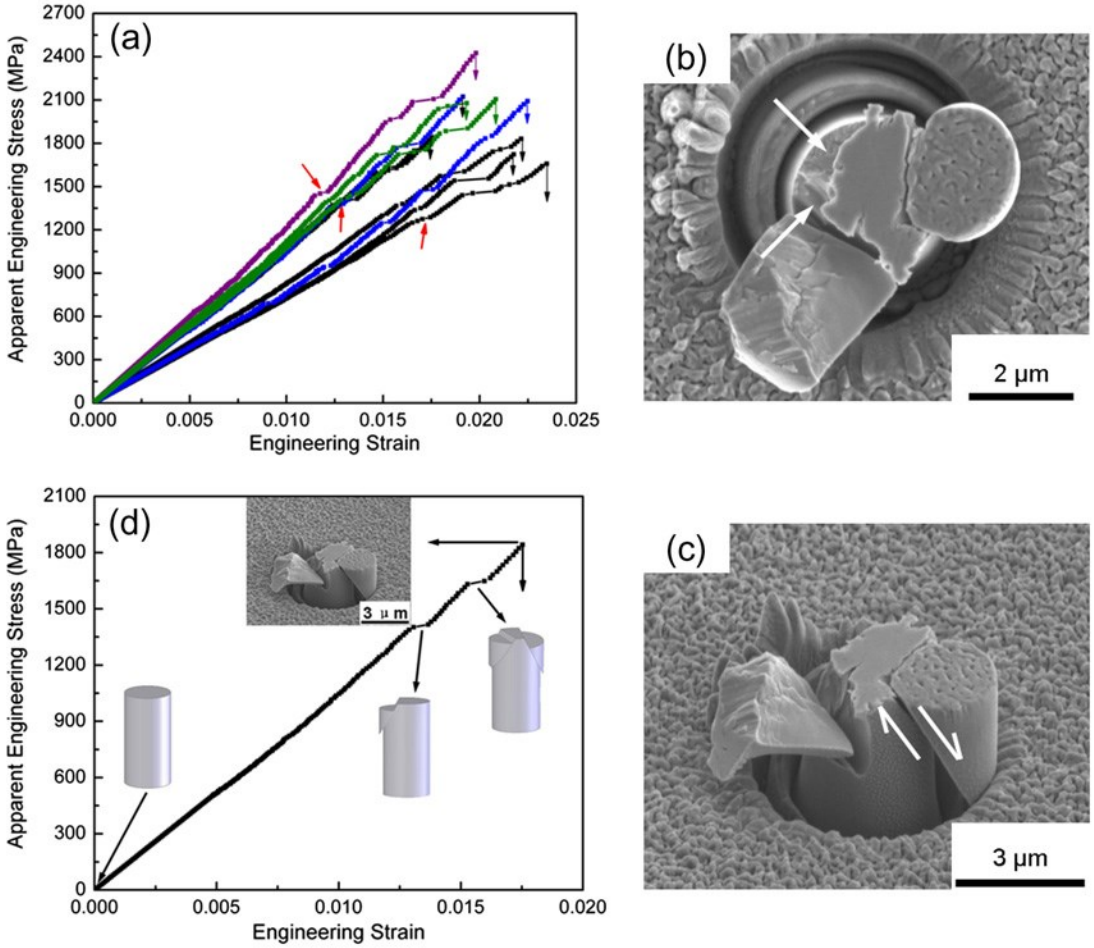


Fig. 38 (a) stress-strain curves of Cu_6Sn_5 single crystals, showing the strain bursts (b-c) top view and side view of cleavage fractured Cu_6Sn_5, corresponding to the strain bursts. (d) schematically presenting the nanoindentation process according to the stress-strain curve [139].

Similar fracture behavior of Cu_6Sn_5 has been reported by Yu et al. [140]. They did nanoindentation on single crystal Cu_6Sn_5 as well and found the several strain bursts Fig. 39(a) and the corresponding SEM in-situ micrographs of cleavage are shown in Fig. 39(b-c). After several (usually 1-5 [141]) cleavages, final fracture occurred and the cleavage planes are parallel to each other Fig. 39(e).

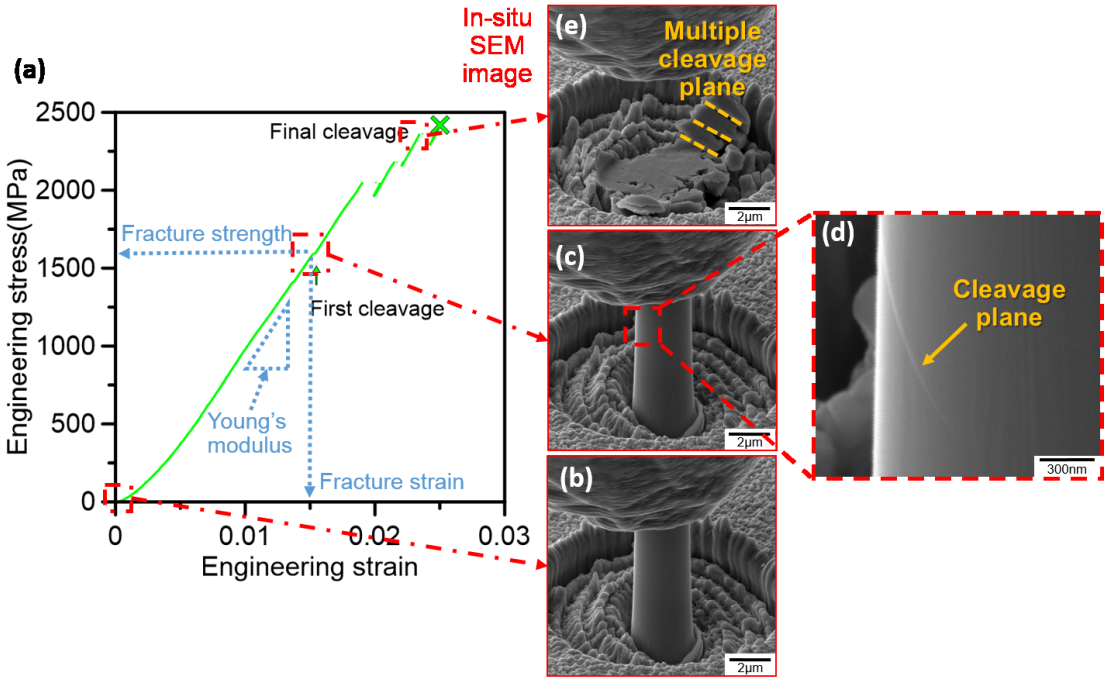


Fig. 39 The stress-strain curve from nanoindentation and corresponding in-situ SEM micrographs [140].

Another work conducted by Yu et al. [141] in which they did micropillar compression and from the stress-strain curve they did not found several strain bursts Fig. 40 (a).

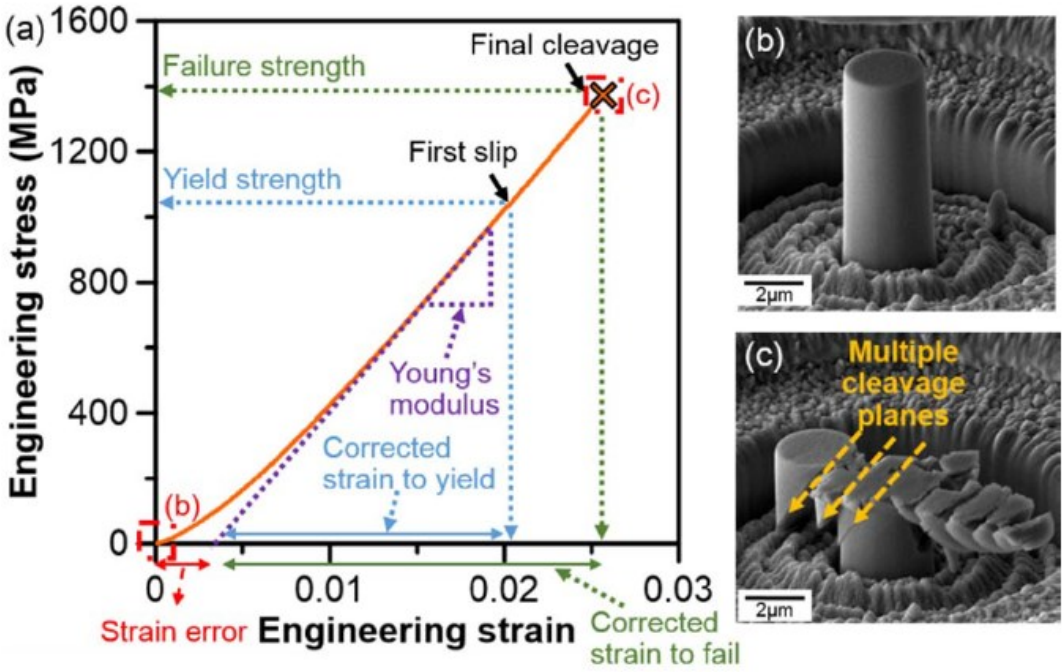


Fig. 40 (a) micropillar compression stress-strain curve of single Cu_6Sn_5 (b) before test (c) after failure [141].

Although the failure mode of Cu_6Sn_5 is still cleavage (Fig. 40(c)) with a brittle nature, it exhibited a small amount of plastic deformation prior to failure and the slip trace has been observed after strain burst (Fig. 41(a)) and no crack was found through the FIB cross section view (Fig. 41(b)). Zhang el al. did in-situ micro-hardness on Cu_6Sn_5 formed at the Sn-4Ag/Cu interface and reported that the initiation of fracture was parallel to the interface where (001) growth textured formed indicating (001) of Cu_6Sn_5 is the slip plane [37].

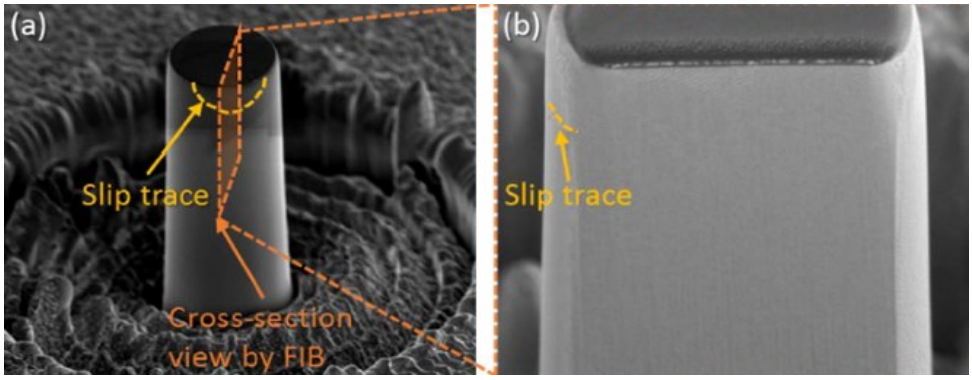


Fig. 41 (a) SEM micrograph of slip trace appeared during micropillar compression (b) FIB cross section view of the Cu_6Sn_5 pillar [141].

Yu et al. [140] also measured the fracture strength, fracture strain and Young's modulus versus the misorientation to c-axis of the Cu_6Sn_5 crystal (Fig. 42) and shown that parallel to c-axis, the mechanical properties are higher [140].

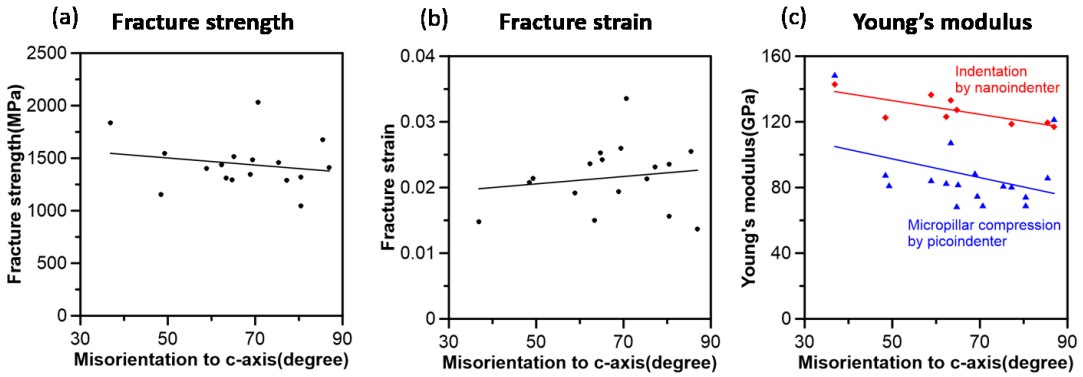


Fig. 42 Fracture strength, fracture strain and Young's modulus versus misorientation to c-axis [140]

The anisotropic mechanical properties in Cu_6Sn_5 have been reported by Jiang et al. who did nanoindentation and microcompression on single Cu_6Sn_5 crystal pillars [142]. They found that the strength and Young's modulus of Cu_6Sn_5 increase up to 20% and 7% as loading became more aligned to the c-axis and the strength decreased linearly with deviation from the c-axis (Fig. 43).

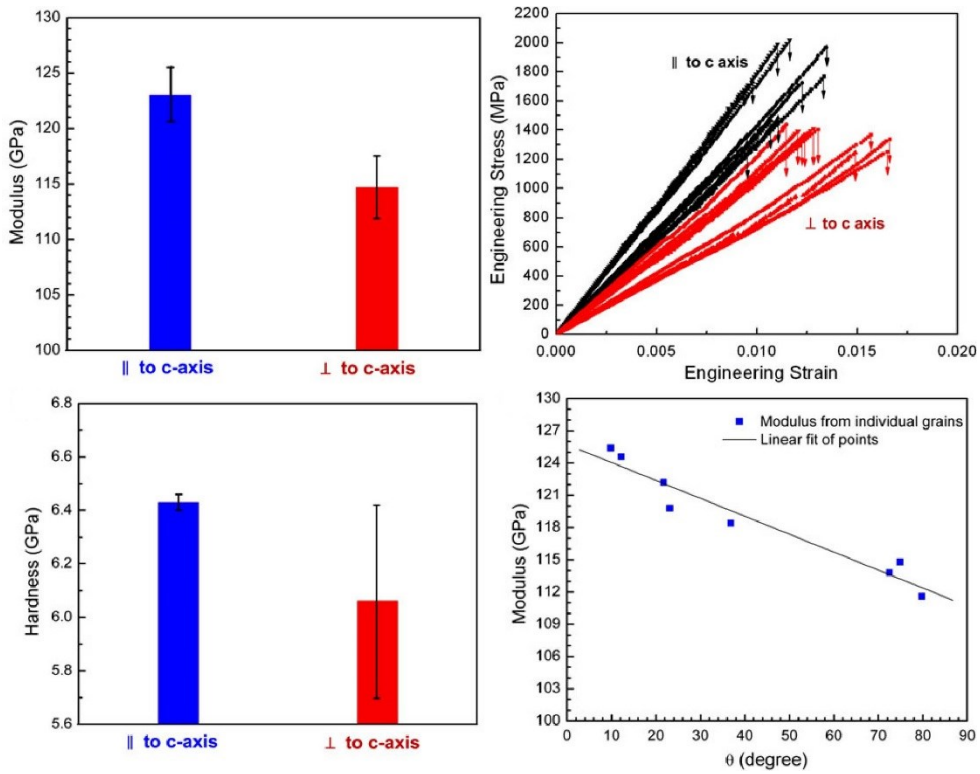


Fig. 43 Comparison of mechanical properties versus misorientation angle from c-axis of Cu_6Sn_5 crystal (modified from [142]).

Mu et al. [143] performed nanoindentation with a conical tip on directly solidified Cu_6Sn_5 crystals, and they reported that with increasing stress, the cracks first appeared in the (001) plane of Cu_6Sn_5 which is perpendicular to the c-axis and the secondary cracks were occurred parallel to the c-axis (Fig. 44) [143] which agrees with the trend of anisotropic mechanical properties of Cu_6Sn_5.

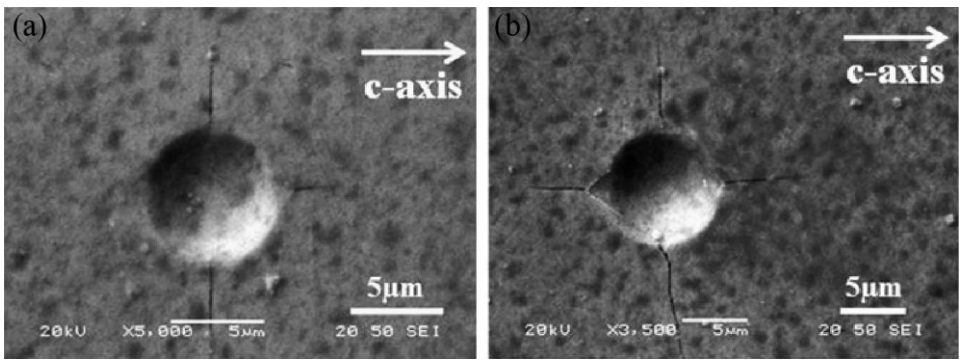


Fig. 44 (a) primary crack formed perpendicular to c-axis 30mN (b) secondary crack formed parallel to c-axis 40mN [143].

In solder joints, the influence of fracture of primary Cu_6Sn_5 on the fracture of the βSn matrix is important, as the reliability of the solder is the key to the reliability of electronic devices. Tian et al. [144] conducted in situ tensile tests on SAC305 solder and reported that the cracks of primary Cu_6Sn_5 due to brittle fracture (Fig. 45(b)) may act as the source of macro-cracks of the solder joint (Fig. 45(c-d)). Zhang et al. [37] found that the Cu_6Sn_5 with long rod morphology tends to crack at the end of grains while those with short rod morphology tend to crack in the middle. However, Kim et al. [49] and Quan et al. [43] both reported similarly that the long Cu_6Sn_5 had little influence on the mechanical properties. Up to now, there are only limited research on the influence of primary Cu_6Sn_5 on the failure of solder or solder joints, and a lot of research regarding the effect of interfacial Cu_6Sn_5 generally reported that solder joints with thicker interfacial layer will have lower fracture toughness [36-48].

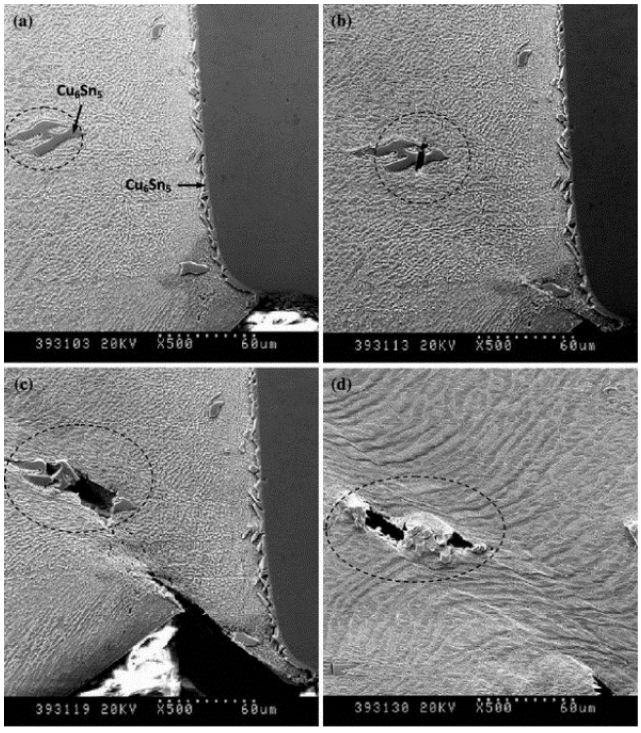


Fig. 45 tensile test with increased deformation (a) 0% (b) 4.6% (c) 11.5% and (d) 16.9% [144]

2.4.4 Fracture of primary Ag_3Sn and its influence on the solder joints

The role of primary Cu_6Sn_5 on solder joint reliability has not been explored in detail. Therefore, the next section reviews past work on the role of another common primary IMC in solder joints: Ag_3Sn

Primary Ag_3Sn crystals are usually on the scale of hundreds of micrometres and have a plate or blade morphology in the bulk solder [145-148] (Fig. 46 [49]).

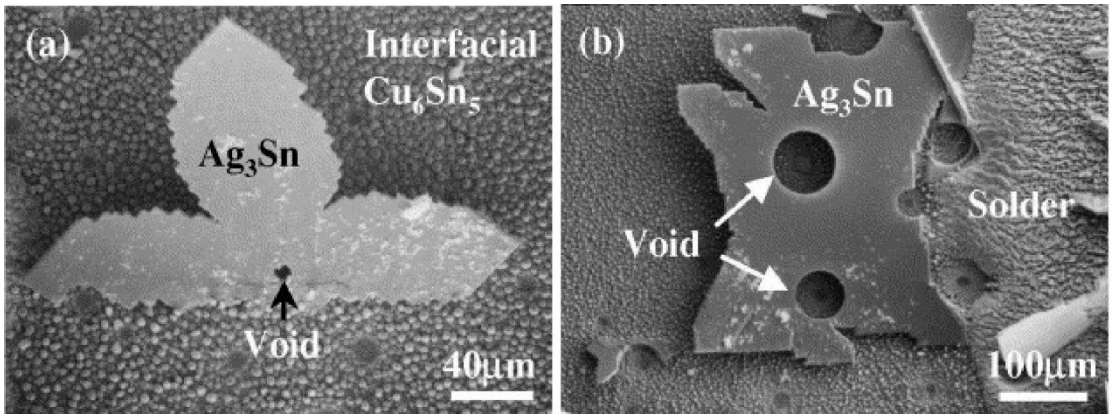


Fig. 46 large Ag_3Sn blades in Sn3.9Ag0.6Cu/Cu joint [49]

The failure mode of primary Ag_3Sn is brittle fracture [49], and it has been shown to have negative effects on the solder joint reliability.

Large primary Ag_3Sn can fracture inside the Sn matrix in the bulk solder and then decohesion will occur between it and the Sn [49] with continuing deformation. The interface between Ag_3Sn and βSn can provide an easier path for the propagation of crack (Fig. 47(a) [49]). At the same time, the large primary Ag_3Sn can also act as secondary crack initiation sites (Fig. 47(b) [49]).

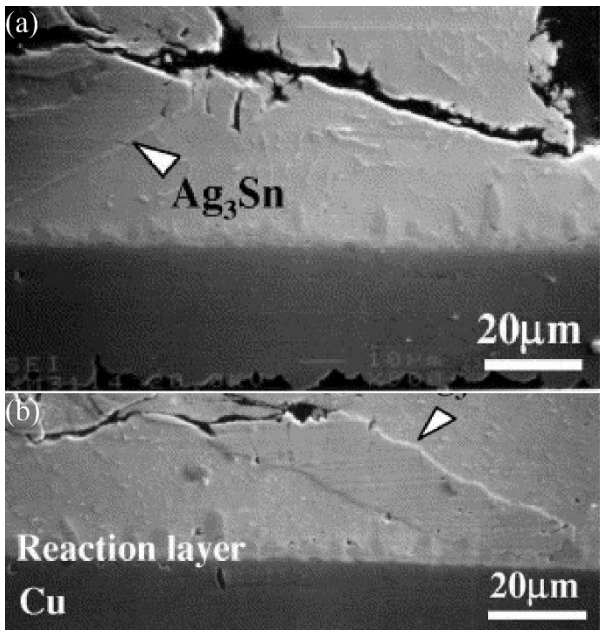


Fig. 47 The crack propagation routes on the interface between Ag_3Sn and Sn matrix (modified from [49])

In addition to tensile and shear impact testing, the preferred propagation routes for cracks could also along the Sn-Ag_3Sn interface boundaries during both thermal cycling (Fig. 48(a) [145]) and three point bending testing (Fig. 48(b) [149]).

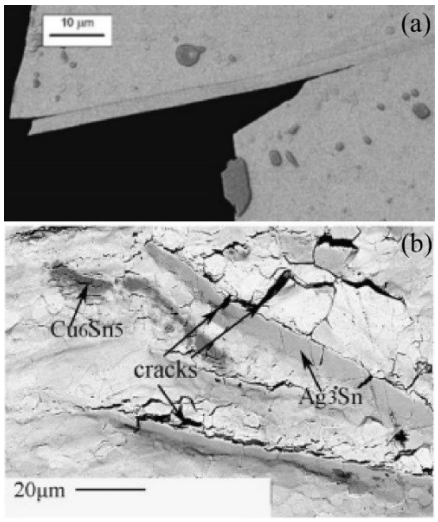


Fig. 48 decohesion at the interface boundary between Ag_3Sn blades and βSn during (a) thermal cycling [145] and (b) during three point bending test [149]

Although large primary Ag_3Sn have been reported to have a negative influence on solder joint reliability, the small eutectic Ag_3Sn have been shown to increase strength and improve crack resistance of the solder by hindering dislocation slip and reducing the grain boundary sliding [149-151]. Indeed, small eutectic Ag_3Sn are one of the most beneficial strengtheners and, generally, act as useful precipitates.

Chapter 3. Influence of reflow process parameters on primary Cu_6Sn_5 morphologies

3.1 Introduction

As reviewed in section 2.3.6, several morphologies of primary Cu_6Sn_5 have been observed and it has been reported that the morphology, thickness of the interfacial Cu_6Sn_5 as well as size and morphology of primary Cu_6Sn_5 all influence the reliability of solder joints and so the reliability of electronic devices. However, most research of primary Cu_6Sn_5 morphology has focussed on the effects of alloying elements [9, 12, 13, 91]. This Chapter explores the influence of soldering process parameters on (i) the volume fraction and morphology of primary Cu_6Sn_5 and (ii) Cu dissolution from the Cu pad (substrate).

3.2 Experimental Methods

3.2.1 Producing solder balls

Sn-0.7wt%Cu was prepared by mixing 99.9wt%Sn ingots with a Sn-10wt%Cu master alloy in a graphite crucible. After heating and holding at 450°C for 4 hours, the liquid was cast into a steel chill mould. The composition of the alloy, analysed by x-ray fluorescence (XRF) spectroscopy, was 0.7 wt% Cu with Ag, Sb, Ni, In less than 0.02wt% and Pb, Bi, Zn, Fe, Al, As, Cd, Ge, Au less than 0.001wt% (Table 7). The as-cast alloy was then rolled to foil with thickness ~0.03mm, punched into discs with diameter ~1.6mm and melted with a ROL1 tacky flux (IPC J-STD- 400) at ~350°C on a hot plate to form solder balls due to surface tension. This approach produced solder balls with diameter of 500 ±25 μm.

Table 7. The composition of the as-cast alloy

Cu%	Pb%	Ag%	Sb%	Bi%	Zn%	Fe%	Al%	As%	Cd%	Ni%	Ge%	In%	Au%
0.697	< 0.001	0.014	0.02	< 0.001	< 0.001	0.001	< 0.001	< 0.001	< 0.001	0.002	< 0.001	0.014	0.001

3.2.2 Reflow soldering

Solder balls were soldered onto 0.5mm 99.99%Cu sheets masked with 500μm diameter pads using a ROL1 tacky flux. Reflow was performed in a forced-air convection oven. For all experiments the mean heating rate was ~20K/s and the following three process parameters were systematically varied: (i) the peak temperature, (ii) the holding time at the peak temperature, and (iii) the cooling rate.

1. Holding times at T^{peak}: 10s, 20s, 30s, 1min, 2min, 5min and 30min

7 batches of solder joints were soldered on Cu using different holding times, 10s, 20s, 30s, 1min, 2min, 5min and 30min with a peak temperature, T^{peak}, of 300°C, followed by cooling under an air extractor. The typical reflow profile is shown in Fig. 49(a) selected from the batch held for 30min. The average cooling rate wass calculated for in the region 290-250°C and is ~ 30 ± 1K/s.

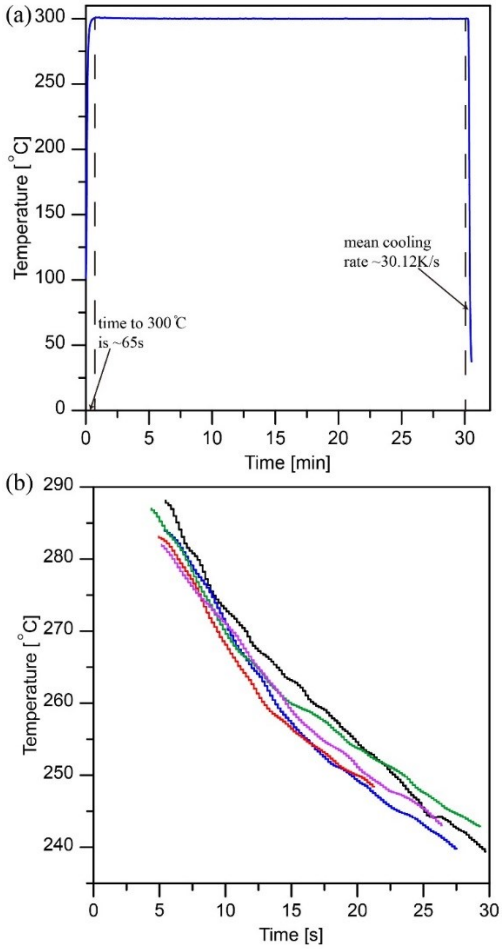


Fig. 49 (a) typical reflow profile (b) Cooling parts of reflow profiles

2. peak temperatures of: 240, 270, 300, 350 and 390°C

5 batches of solders were soldered on Cu at peak temperatures of 240, 270, 300, 350 and 390°C, all with a holding time at the peak temperature of 5 min. Cooling was performed by fully opening the furnace door. The average cooling rate in the range 290-250°C was ~2.6±0.2K/s, calculated from Fig. 49(b).

3. cooling rates: 0.67, 2.6 and 30K/s

5 batches of solder balls were soldered on Cu in a Mettler Toledo DSC1 by heating

at 0.33K/s up to five different peak temperatures i.e. 240, 270, 300, 350 and 390°C for each batch. The corresponding times that solder balls were melted during heating (from eutectic temperature to the peak temperature) were 39.4, 130.3, 221.2, 372.7 and 493.9s. After 5 min at peak temperature, the joints were saturated with Cu and were cooled at 0.67K/s. Another 5 batches were soldered in a furnace with the same five different peak temperatures and then cooled at ~30 ± 1K/s .

After soldering, all solder joints were washed in methanol in an ultrasonic bath to remove residual flux.

3.2.3 Measurement of solder composition after reflow

To study the influence of holding time on the composition of the solder on Cu substrates, ~3200 solder balls were separated into 4 batches and then were soldered onto Cu pads with a peak temperature of 300°C for holding times of 10s, 30s, 5min and 30min followed by cooling at ~30 K/s. After soldering, the solder ball of each joint was detached by low speed (~10 mm/s) ball shear using a blunt steel tool. Careful attention was paid to avoid interfacial Cu_6Sn_5 from being detached with the bulk solder, which would influence (increase) the tested bulk solder composition. For each batch (i.e. holding time), >700 detached balls were collected and re-melted with a ROL1 tacky flux to make a sample for composition analysis. ICP-AES was then conducted to measure the mean Cu content of each batch (holding time) using a Shimadzu ICPS-7510.

3.2.4 Microscopy

Cross sections were prepared by mounting joints in Struers VersoCit resin, grinding

with SiC papers down to 4000 grit size and polishing with colloidal SiO_2 suspension. Sections were then observed by optical microscopy. After that, these cross sections were shallow etched in a solution of 5% NaOH and 3.5% ortho-nitrophenol in distilled H_2O at ~90°C for ~1min to remove Sn and then were coated with carbon and observed by secondary electron imaging in a Zeiss Auriga field emission gun scanning electron microscopy (FEG-SEM). In order to view the 3D morphology of primary and interfacial Cu_6Sn_5, deeply etched cross sections were prepared and imaged using similar procedures.

The thickness of Cu pad dissolution, the mean thickness of the interfacial Cu_6Sn_5 layer, and the mean thickness of the Cu_3Sn layer were measured on SEM images using image J with the definition that the mean thickness is equal to the area of the layer divided by the width of the layer in the micrograph. At least 4 samples were measured for each condition.

3.3 Results and Discussion

3.3.1 Influence of holding time at peak reflow temperature

Fig. 50 (a) and Table 8 show the Cu content of the solder balls measured by ICP-AES after soldering to Cu substrates for different holding times at 300°C followed by fast cooling at ~30 K/s. The experimental data were analysed using the Nernst-Brunner dissolution equation in Equation 54:

$$\mathrm{C} = C_{sat} - (C_{sat} - C_0) \cdot \exp(-\frac{KAt}{V}) \qquad \text{Equation 54}$$

where C is the mean Cu content of the solder at time t, C_{sat} is the Cu-saturated liquid composition (i.e. the Cu solubility) at 300°C, C_0 is the original solder composition, A is the Cu pad area, V is the volume of solder, and K is the Nernst-Brunner dissolution rate constant.

Based on Equation 55, a best fit value of K= 0.8 mm min^{-1} was obtained from the gradient of a plot of $\ln\big((C_{sat} - C_0)/(C_{sat} - C)\big)$ versus $\frac{At}{V}$, using C_0 = 0.7 wt% Cu and C_{sat} = 2.34 wt% Cu. K= 0.8 mm min^{-1} is similar to the value of 0.6 mm min^{-1} obtained by Chada et al. for Cu dissolution into Sn-3.5wt%Ag solder reflowed on Cu at 302°C [125].

$$\ln\left(\frac{C_{sat} - C_0}{C_{sat} - C}\right) = K \cdot \frac{At}{V} \qquad \text{Equation 55}$$

The blue curve in Fig. 50(a) is the mean Cu content versus time plotted using Equation 54 with C_0 = 0.7 wt% Cu, C_{sat} = 2.34 wt% Cu, and K = 0.8 mm min^{-1}. This

is plotted twice; versus time on the lower axis and versus the Nernst-Brunner parameter $\frac{At}{V}$ on the upper x-axis. It can be seen that the Nernst-Brunner equation fits well to the measured mean Cu content of the bulk solder.

Fig. 50 (b) shows the Sn-Cu phase diagram from the Thermo-Calc TCSLD3.2 database [97], with the Cu content of the original solder alloy, C_0 = 0.70wt%Cu, and the saturated Cu composition at 300°C, C_{sat} =2.34wt%Cu, superimposed. It can be seen that the predicted solubility of Cu content in liquid at 300°C is in good agreement with the experimental result.

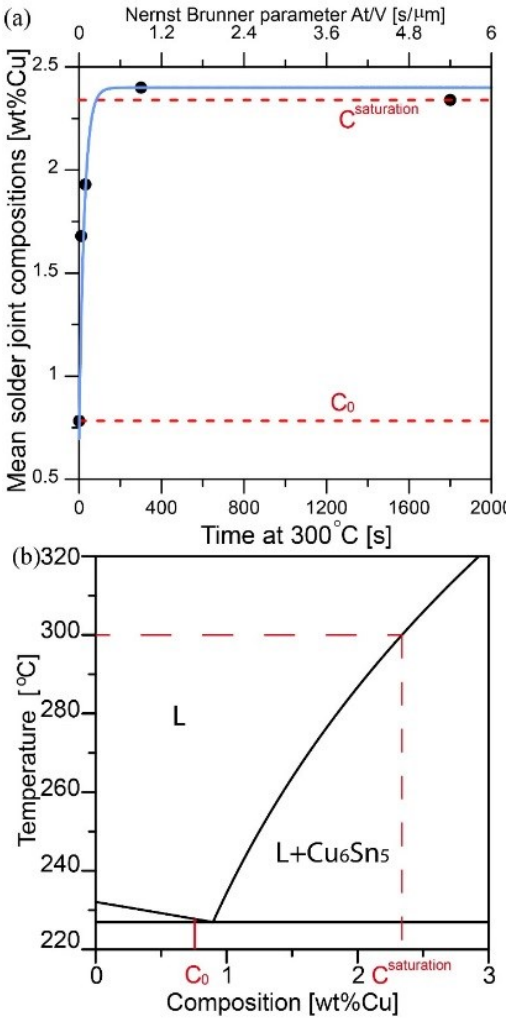


Fig. 50 (a) Variation of Cu content in bulk solder joint after aging for different times at 300°C. Datapoints are ICP-AES measurements. (b) Partial Sn-Cu phase diagram at the Sn rich part [97].

Examining Fig. 50 (a), it can be seen that the average Cu content in the liquid increased sharply in the first 180s of holding and, from 300s onwards, the Cu content is near-constant and close to the predicted saturation composition, indicating that the liquid had become uniformly saturated in Cu. There is a drop in Cu content from 5min to 30min. It is unclear if this is a real effect or due to error/uncertainty in the ICP measurement. Further experiments are needed to confirm this.

Table 8. ICP tested mean compositions of bulk solder joints at five different holding time

Holding time at 300°C/min	Average Cu content/ wt%Cu
0	0.78
0.17	1.68
0.5	1.93
5	2.4
30	2.34

Fig. 51 shows typical micrographs of the bulk solder, the intermetallic reaction layers, and the partially dissolved Cu pads for joints held for 10s, 30s, 5min and 30min at 300°C before being cooled at ~30 $K.s^{-1}$. It is clear that, with increasing holding time, there is an increase in (i) the fraction of primary Cu_6Sn_5 in the bulk solder, (ii) the thickness of the IMC layer(s), and (iii) the thickness of Cu substrate dissolved. These changes are quantified in Fig. 52 and Table 9.

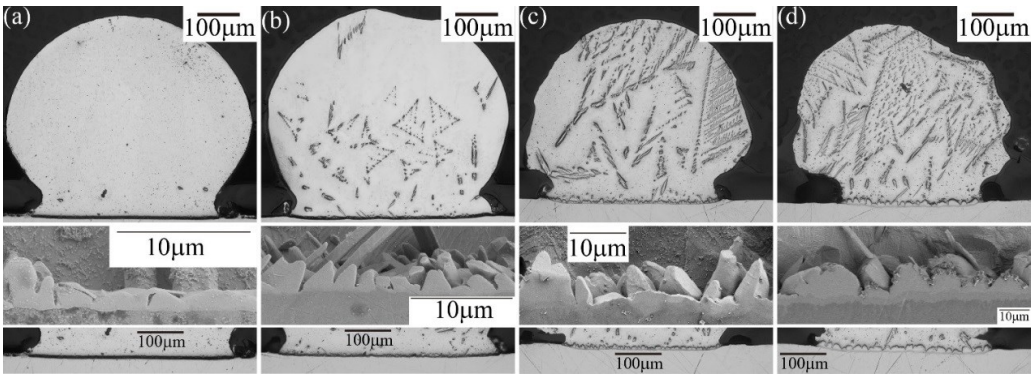


Fig. 51(a)-(d) solder joints that were held at 300°C for 10s, 30s, 5min and 30min before being cooled at ~30 K/s. Top row: full cross-sections showing primary Cu_6Sn_5. Middle row: Cu_6Sn_5 layers after deep etching. Bottom row: dissolved Cu substrate.

Fig. 52(a) shows the area fraction of primary Cu_6Sn_5 in the bulk solder ,$g_{Cu6Sn5}^{primary}$, measured from at least 4 micrographs of solder joints held for 10s, 30s, 1min, 2min, 5min and 30min. It also shows the fraction of primary Cu_6Sn_5 versus time calculated from the Sn-Cu phase diagram using the liquid compositions measured by ICP-AES in Table 8 and Fig. 50(a). It can be seen that for both the measured and calculated results, with increasing holding time, the area fraction of primary Cu_6Sn_5 increases and they have a similar trend.

Table 9 mean thickness of Cu pad dissolution, interfacial Cu6Sn5 layer, interfacial Cu3Sn layer and primary Cu6Sn5 area fraction

	Mean Cu layer dissolution/um	**Mean Cu6Sn5 layer/um**	**Mean Cu3Sn layer/um**	**Primary Cu6Sn5 area fraction/%**
0.5min	5.59	2.28	_	3.8
1min	8.20	2.56	_	6.04
2min	8.96	3.33	_	6.58
5min	9.81	4.89	_	7.13
30min	13.4	7.54	2.66	7.10

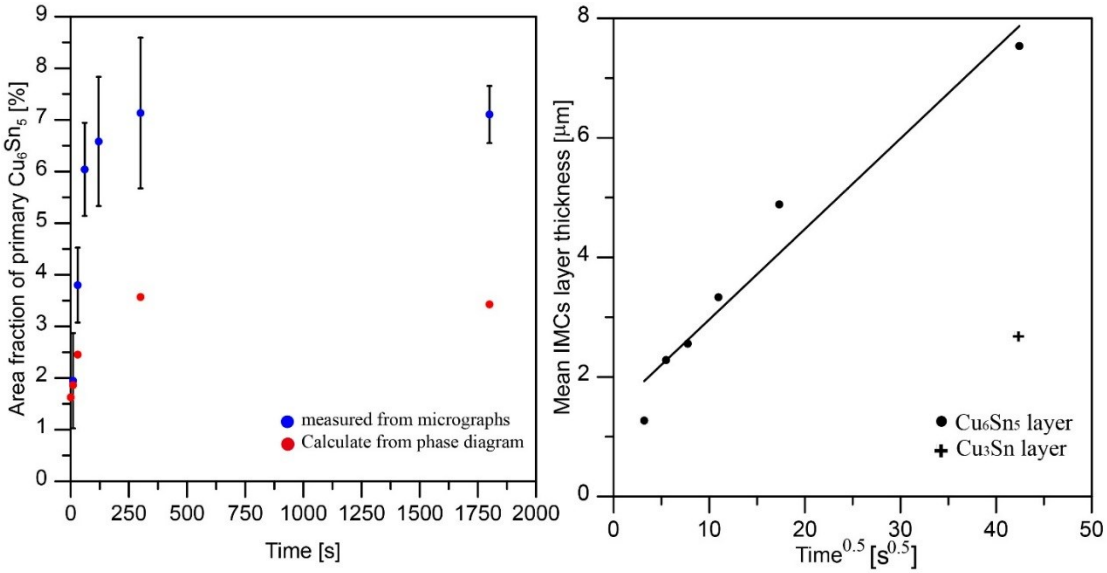


Fig. 52 (a) Blue data point: area fraction of primary Cu_6Sn_5 in solder joints held at 300°C for 10s, 30s, 1min, 2min, 5min and 30min. Red data point: volume fraction of primary Cu_6Sn_5 calculated from equilibrium phase diagram with the compositions measured by ICP-AES and were shown in Table 8. (b) IMC layer thickness versus the square root of aging time.

Fig. 52 (b) shows the development of IMC layer thickness with holding time at 300°C. It can be seen that the Cu_6Sn_5 layer thickness scales with the square root of holding time, indicating that Cu_6Sn_5 layer growth is governed by volume diffusion through the Cu_6Sn_5 layer. A Cu_3Sn layer was only observed after 30 minutes at 300°C as shown in Fig. 51(d).

Fig. 53 depicts the key features of the solder reaction and development of microstructure during reflow of a Sn0.7Cu/Cu BGA solder joint.

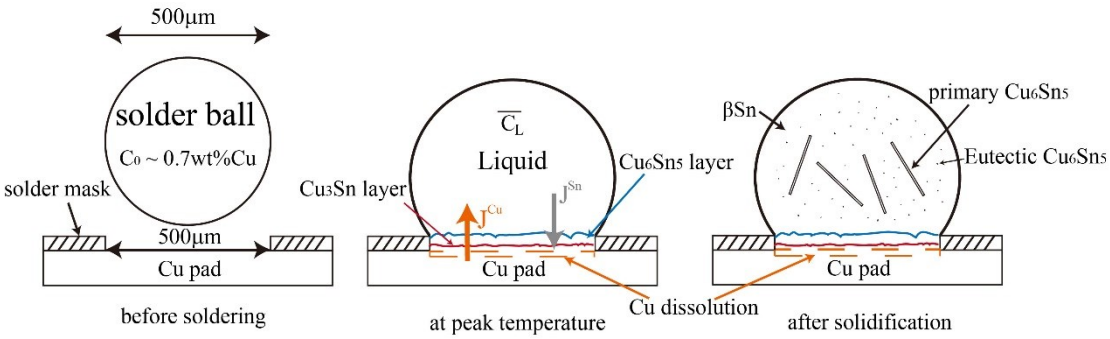


Fig. 53 Schematic diagram of the key features BGA soldering

Initially, between Fig. 53(a) and Fig. 53(b), the solder ball melts, wets and spreads on the Cu pad. The liquid reacts with the Cu to form a Cu_6Sn_5 layer and, for long enough holding time, also a Cu_3Sn layer. At the peak temperature (Fig. 53(b)), the liquid solder has a mean Cu content of $\overline{C_L}$ that changes with time until uniform saturation is reached. After solidification (Fig. 53(c)), the microstructure of the solder joint contains primary Cu_6Sn_5, βSn, and eutectic Cu_6Sn_5 in the bulk solder, and Cu_6Sn_5 and Cu_3Sn layers between the solder and Cu. The relationships between the growth of IMC layers, the formation of primary Cu_6Sn_5 and the thickness of dissolved Cu substrate can be derived as follows:

(1) Cu dissolution thickness due to the formation of an interfacial Cu_6Sn_5 layer:

6 moles of Cu react to create 1 mol of Cu_6Sn_5 via the reaction $6Cu+Sn \rightarrow Cu_6Sn_5$.

Therefore, the volume of copper substrate consumed in forming 1 mol of Cu_6Sn_5 is:

$$V_{Cu} = 6\frac{M_{Cu}}{\rho_{Cu}}$$

where M_{Cu} is the molar mass of Cu and ρ_{Cu} is the density of Cu.

the volume, $V_{Cu_6Sn_5}$, of 1 mol of Cu_6Sn_5 is:

$$V_{Cu_6Sn_5} = \frac{M_{Cu_6Sn_5}}{\rho_{Cu_6Sn_5}}$$

therefore:

$$\frac{V_{Cu_6Sn_5}\rho_{Cu_6Sn_5}}{M_{Cu_6Sn_5}} = \frac{V_{Cu}\rho_{Cu}}{6M_{Cu}} = 1$$

$$V_{Cu} = 6\frac{V_{Cu_6Sn_5}\rho_{Cu_6Sn_5}M_{Cu}}{M_{Cu_6Sn_5}\rho_{Cu}} \qquad \text{Equation 56}$$

as the area of the Cu pad is approximately equal to the area of the Cu_6Sn_5 layer, the thickness of the dissolved Cu can be written as:

$$L_{Cu} = 6\frac{L_{Cu_6Sn_5}^{layer}\rho_{Cu_6Sn_5}M_{Cu}}{M_{Cu_6Sn_5}\rho_{Cu}}$$

where $L_{Cu_6Sn_5}$ is the mean thickness of the Cu_6Sn_5 layer.

(2) Cu dissolution thickness due to the formation of an interfacial Cu3Sn layer:

A similar derivation considering the Cu_3Sn layer gives:

$$L_{Cu} = 3\frac{L_{Cu_3Sn}\rho_{Cu_3Sn}M_{Cu}}{M_{Cu_3Sn}\rho_{Cu}}$$

where L_{Cu} is the thickness of dissolved copper substrate due to the formation of a Cu_3Sn layer with mean thickness L_{Cu_3Sn}.

(3a) Cu dissolution thickness due to the formation of Cu_6Sn_5 in the bulk solder:

The relationship between the volume of primary Cu_6Sn_5 and the volume of dissolved Cu substrate is also given by Equation 56. The volume of primary Cu_6Sn_5 can be calculated from Equation 57 where V_{solder} is the volume of the solder which can be taken as the volume of the solder ball before soldering ($6.54 \times 10^7 \mu m^3$ for 500 μm balls); A_{pad} is the area of the Cu pad; and $g_{Cu6Sn5}^{primary}$ is the volume fraction of primary Cu_6Sn_5 in the solder joint, which is equal to the mean area fraction of primary Cu_6Sn_5 in micrographs provided that sufficient microstructure is sampled:

$$V_{Cu_6Sn_5}^{primary} = V_{solder}g_{Cu6Sn5}^{primary} \qquad \text{Equation 57}$$

the volume of Cu dissolution equals the thickness of Cu dissolved multiplied by the area of the Cu pad. Substituting Equation 57 into Equation 56:

$$L_{Cu} = \frac{6\rho_{Cu_6Sn_5}M_{Cu}}{M_{Cu_6Sn_5}\rho_{Cu}} \cdot \frac{V_{solder}}{A_{pad}} \cdot g_{Cu6Sn5}^{primary} \qquad \text{Equation 58}$$

(3b) Cu dissolution thickness due to the increase in Cu content in the liquid:

The mean Cu content in the bulk solder joint after soldering (measured by ICP-AES) is approximately equal to the mean Cu content in the liquid at the peak temperature, $\overline{C_L}$. The mass fraction of primary Cu_6Sn_5 in the bulk solder, $f_{Cu_6Sn_5}$, can be calculated from the Sn-Cu phase diagram with the $\overline{C_L}$ data using Equation 59, assuming that βSn nucleates at the eutectic temperature when the liquid composition is C_L= 0.89 wt% Cu:

$$f_{Cu_6Sn_5} = \frac{\overline{C_L} - 0.89}{38.5 - 0.89} \qquad \text{Equation 59}$$

if, however, βSn nucleation requires an undercooling, the fraction of primary Cu_6Sn_5 in the bulk solder will be higher and equal to:

$$f_{Cu_6Sn_5} = \frac{\overline{C_L} - C_L^*}{38.5 - C_L^*}$$

where C_L^* is the composition of the liquid at the βSn nucleation temperature, T_n. This can be found from the Cu_6Sn_5 metastable liquidus extension line which can be expressed (in wt% Cu and °C) as [97]:

$$C_L^* = 9.303 \times 10^{-9} \cdot T_n^{3.389}$$

the volume fraction of Cu_6Sn_5 can be calculated from the mass fraction of Cu_6Sn_5:

$$g_{Cu_6Sn_5}^{primary} = \frac{\frac{f_{Cu_6Sn_5}}{\rho_{Cu_6Sn_5}}}{\frac{1 - f_{Cu_6Sn_5}}{\rho_{Sn}} + \frac{f_{Cu_6Sn_5}}{\rho_{Cu_6Sn_5}}}$$

(4) Total thickness of dissolved Cu substrate:

The total thickness of dissolved Cu is then the sum of the three components: the

formation of the Cu_3Sn layer, the Cu_6Sn_5 layer and primary Cu_6Sn_5 in the bulk solder.

$$L_{Cu} = \frac{6\rho_{Cu_6Sn_5}M_{Cu}}{M_{Cu_6Sn_5}\rho_{Cu}}L_{Cu_6Sn_5}^{layer} + \frac{3\rho_{Cu_3Sn}M_{Cu}}{M_{Cu_3Sn}\rho_{Cu}}L_{Cu_3Sn}^{layer} + \frac{6\rho_{Cu_6Sn_5}M_{Cu}V_{solder}}{M_{Cu_6Sn_5}\rho_{Cu}A_{pad}}g_{Cu6Sn5}^{primary}$$

where $g_{Cu6Sn5}^{primary}$ can either be measured (3a) or calculated from the mean Cu content in the bulk solder joint after soldering (measured by ICP-AES) (3b). Using the data in Table 10, the relationship can be rewritten as:

$$L_{Cu} = 0.36L_{Cu_6Sn_5}^{layer} + 0.78L_{Cu_3Sn}^{layer} + 0.36\frac{V_{solder}}{A_{pad}}g_{Cu6Sn5}^{primary}$$

This can also be rewritten in terms of mass:

$$m_{Cu} = 0.36L_{Cu_6Sn_5}^{layer}A_{pad}\rho_{Cu} + 0.78L_{Cu_3Sn}^{layer}A_{pad}\rho_{Cu} + 0.36V_{solder}g_{Cu6Sn5}^{primary}\rho_{Cu} \qquad \text{Equation 60}$$

Table 10 parameters for Sn, Cu, Cu_6Sn_5 and Cu_3Sn

atomic mass of Cu /gmol^{-1}	63.546
atomic mass of Sn /gmol^{-1}	118.7
Molar mass of Cu_6Sn_5 /gmol^{-1}	974.776
Molar mass of Cu_3Sn /gmol^{-1}	309.338
diameter of solder ball /mm	0.5
density of Cu_3Sn /gcm^{-3}	11.33
density of Sn /gcm^{-3}	7.31
density of Cu_6Sn_5 /gcm^{-3}	8.26
density of Cu /gcm^{-3}	8.96

Fig. 54 plots datapoints for the Cu mass gained by the Cu_6Sn_5 layer, the Cu_3Sn layer and the liquid versus time at 300°C using Equation 60, parameters from Table 10 and the measurements of $L_{Cu_6Sn_5}^{layer}$, $L_{Cu_3Sn}^{layer}$, and $g_{Cu6Sn5}^{primary}$ from Table 9. Fig. 54 also plots the Cu mass lost from the Cu pad (as a negative mass) versus time using the measurements in Table 9. The sum of the mass gained in the IMC layers and liquid is also plotted as a negative mass for comparison. It can be seen that the total Cu mass

lost from the Cu pad (black cross) fits closely with the total Cu mass gained (blue dots), which means that Equation 60 is effective.

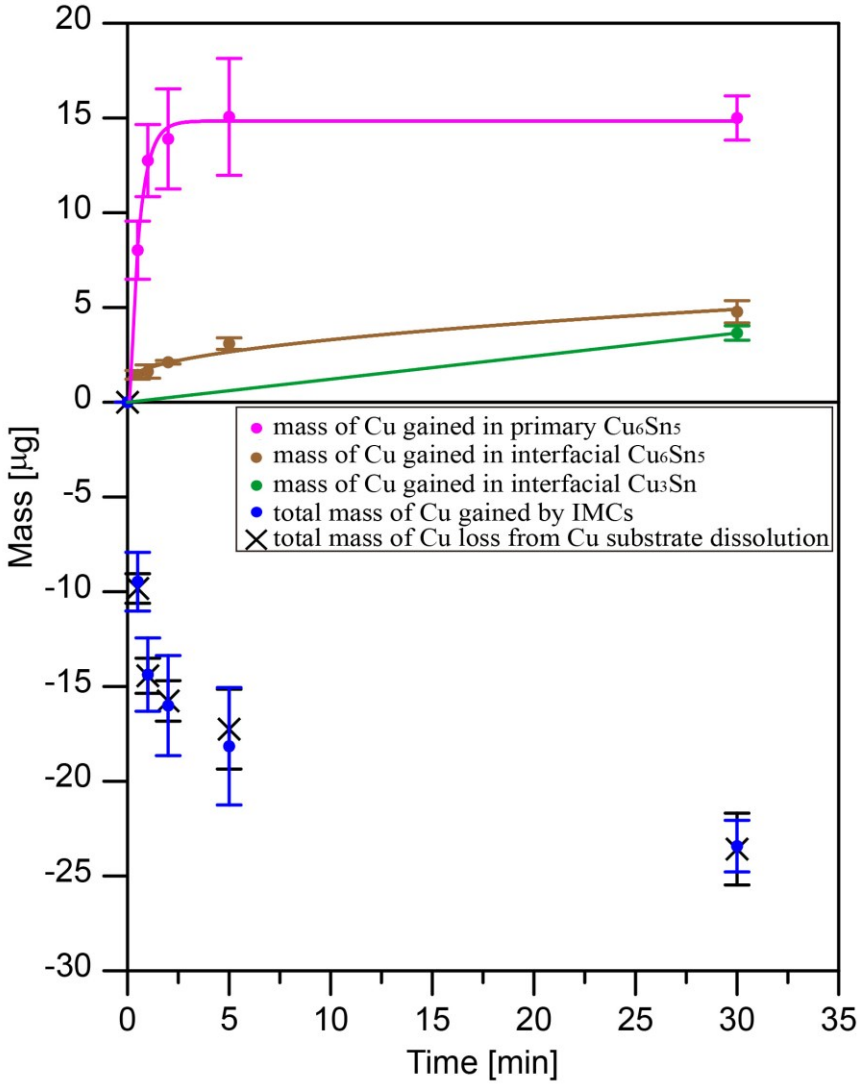


Fig. 54 Cu mass gained in each of IMCs and Cu mass lost from Cu pad with time

Fig. 54 shows that the dissolution of the Cu substrate has two components: (1) the reaction to form Cu_6Sn_5 and Cu_3Sn layers, and (2) Cu dissolution to move the liquid towards the equilibrium Cu solubility at the peak temperature. In Equation 54, it can be seen that component (2) was dominant in the first 300 seconds and then, once the liquid approached uniform Cu saturation, component (1) became dominant.

3.3.2 Influence of peak temperature

Fig. 55 shows typical cross sections of Sn-0.7wt%Cu/Cu solder joints held at (a) 240°C, (b) 270°C, (c) 300°C, (d) 350°C and (e) 390°C for 5min followed by cooling at ~2.6 K/s. It is clear that, with increasing peak temperature, the fraction of primary Cu_6Sn_5 increases, the Cu_6Sn_5 and Cu_3Sn layers become thicker, and more Cu substrate is dissolved. Table 11 summarises the measured thicknesses of the Cu_6Sn_5 and Cu_3Sn layers, the area fractions of primary Cu_6Sn_5, and the thickness of Cu substrate dissolved.

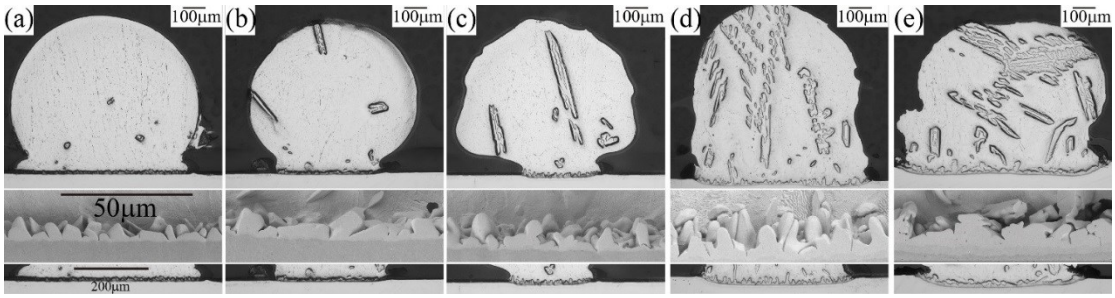


Fig. 55 (a)-(e) solder joints that were held for five minutes at 240°C, 270°C, 300°C, 350°C and 390°C before being cooled at ~2.6 K/s. Top row: full cross-sections showing primary Cu_6Sn_5. Middle row: Cu_6Sn_5 layers after deep etching. Bottom row: dissolved Cu substrate.

Table 11 measurements of thicknesses of Cu_6Sn_5 and Cu_3Sn layer, area fraction of primary Cu_6Sn_5 and the thickness of Cu substrate dissolution.

	Mean Cu layer dissolution/um	**Mean Cu6Sn5 layer/um**	**Mean Cu3Sn layer/um**	**Primary Cu6Sn5 area fraction/%**
Peak 240°C	1.62	3.12	0.24	0.22
Peak 270°C	4.40	3.97	0.591	1.69
Peak 300°C	7.28	4.48	0.76	4.51
Peak 350°C	18.87	5.75	1.68	7.44
Peak 390°C	25.88	6.11	2.86	11.49

Fig. 56(a) plots the measured area fraction of primary Cu_6Sn_5 at each peak temperature (datapoints) where the error bars are standard deviation from 4 micrographs at each condition given the assumptions that the microstructures of primary Cu_6Sn_5 and the micrographs taken are random and that sufficient microstructure is sampled. Fig. 56(b) shows the Sn-Cu phase diagram up to 7wt%Cu from Thermo-Calc TCSLD3.2 [97] and the saturated liquid composition of the five peak temperatures: 240°C, 270°C, 300°C, 350°C and 390°C. Fig. 56(c) shows the mass fraction of Cu_6Sn_5 as a function of temperature for cooling from the five peak temperatures studied, predicted using reference [97]. The βSn-Cu_6Sn_5 eutectic temperature is labelled and the dashed curves below this line indicate the continued solidification of primary Cu_6Sn_5 for cases where βSn does not nucleate (i.e. along the metastable Cu_6Sn_5 liquidus extension line). From similar calculations incorporating the densities, the volume fraction of primary Cu_6Sn_5 versus the peak temperature is plotted as curves with different colours in Fig. 56(a) for three values of βSn nucleation (0, 15 and 47 K undercooling). It can be seen that there is reasonable agreement between the calculations and the measured area fractions of primary Cu_6Sn_5. This indicates that the liquid was approximately uniformly saturated at each peak temperature.

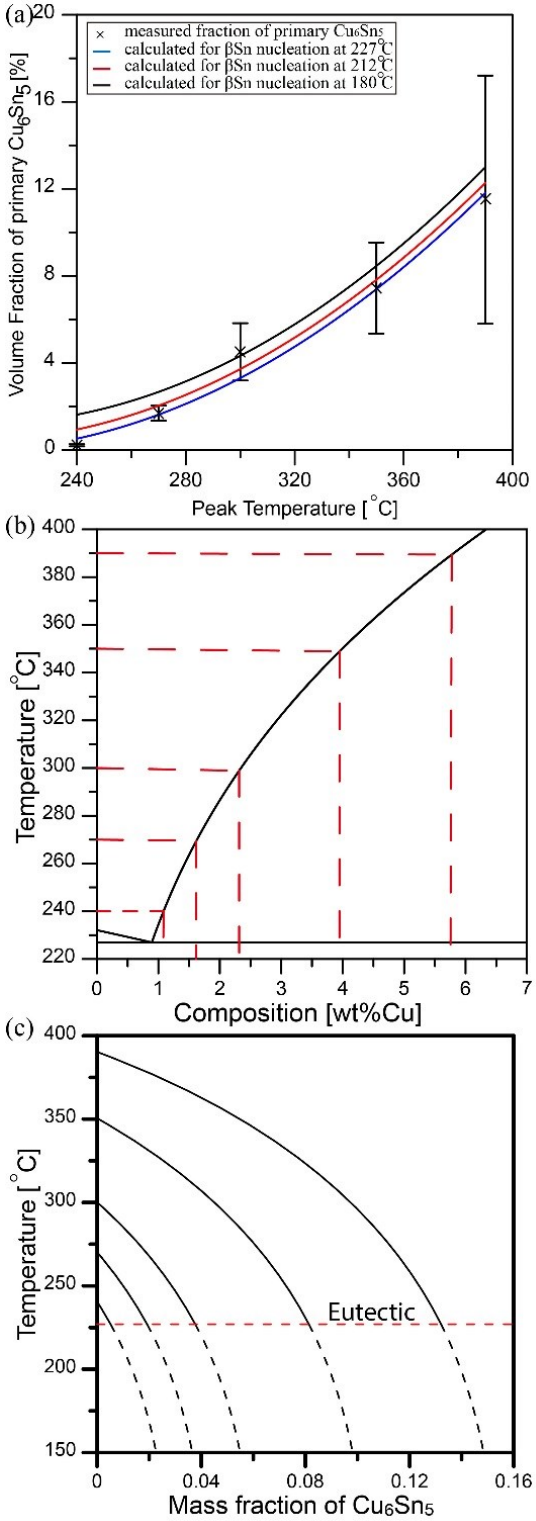


Fig. 56 (a) Measured area fraction of primary Cu_6Sn_5 versus peak temperature (black cross) compared with predictions of the volume fraction of primary Cu_6Sn_5 versus peak temperature for three values of βSn nucleation undercooling (coloured curves). (b) Sn-Cu phase diagram from ref [97] indicating the saturated liquid compositions for the five peak temperatures (c) Mass fraction of primary Cu_6Sn_5 as a function of temperature for uniformly saturated liquid cooled from the five peak temperatures (calculated using ref [97]).

The data in Table 11 has been converted into the mass of Cu gained and lost, and plotted in Fig. 57. It shows the Cu mass gained in the Cu_3Sn layer, the Cu_6Sn layer and in the primary Cu_6Sn_5 as a positive mass. It also shows the Cu mass lost from the Cu pad as a negative mass (black crosses). The blue data are the sum of the mass lost to the Cu_3Sn layer, Cu_6Sn_5 layer and primary Cu_6Sn_5 plotted as a negative mass for comparison with the measured Cu mass lost from the Cu pad (black crosses). It can be seen that the sum of Cu mass gained in the formation of IMCs is in reasonable agreement with the Cu mass dissolved from the copper substrate.

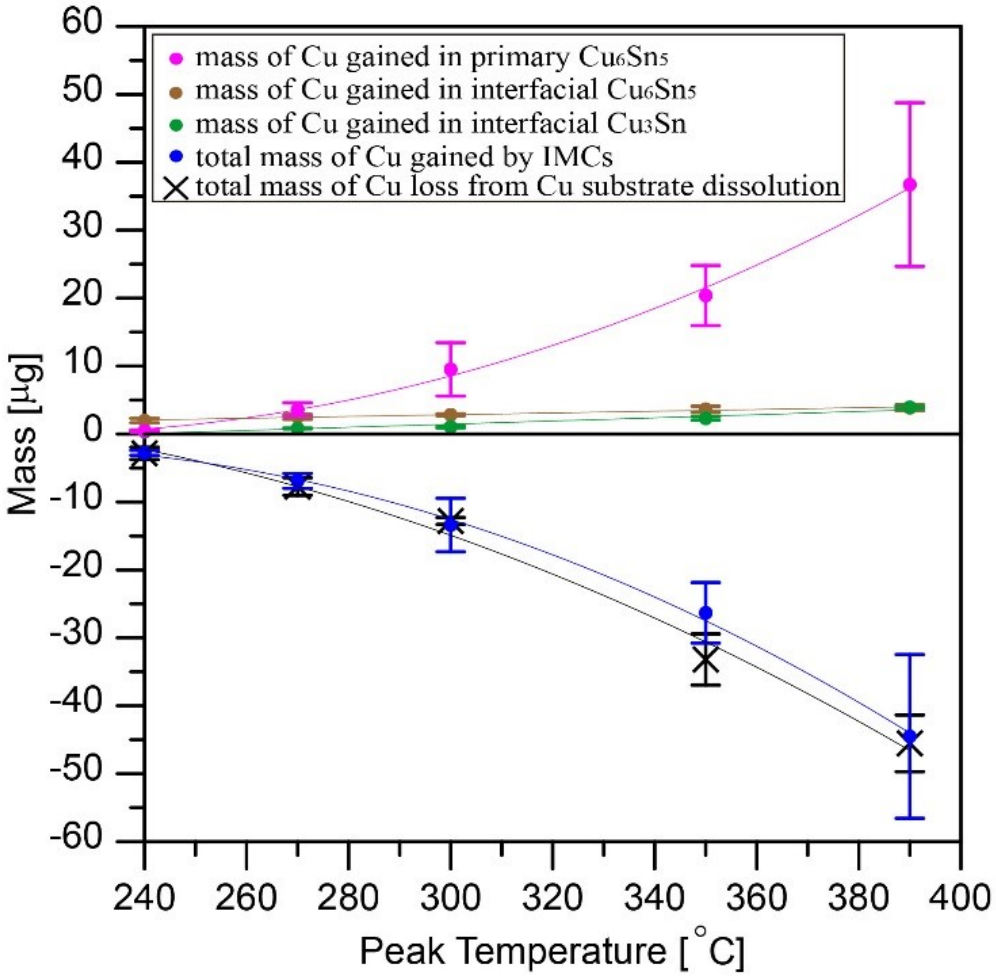


Fig. 57 Cu mass gained in the Cu_3Sn layer (green), Cu_6Sn_5 layer (brown) and primary Cu_6Sn_5 (pink), along with the Cu mass lost from the Cu pad versus time. Black crosses are from the measured thickness of dissolved Cu. Blue data are the sum of the mass lost to the Cu_3Sn layer, Cu_6Sn_5 layer and primary Cu_6Sn_5

Fig. 57 also clearly shows the relative contributions to Cu dissolution from: (1) the reaction to form Cu_6Sn_5 and Cu_3Sn layers, and (2) Cu dissolution to move the liquid towards the equilibrium Cu solubility at the peak temperature. It can be seen that component 1 was dominant for low peak temperatures (e.g. 240 °C) that are commonly used in industrial reflow soldering. In contrast, as the peak reflow temperature increases, component 2 became the dominant source of Cu dissolution. Since the liquid was approximately uniformly saturated at each peak temperature, it can be concluded that the increased Cu dissolution at increased peak temperature is mostly due to the increased solubility of Cu in the liquid at increased temperature (i.e. the effect is predominantly thermodynamic rather than kinetic). It can also be seen that, while the IMC layers are thicker at higher peak temperature, increased IMC layer growth is not the main contributor to increased Cu dissolution at increased peak temperature.

3.3.3 The morphologies of primary Cu_6Sn_5

Throughout this work, a wide variety of primary Cu_6Sn_5 growth morphologies formed. These could be categorised into four types similar to those reported and discussed by Xian et al. [11]. Fig. 58 shows the typical features of the four primary Cu_6Sn_5 morphologies: (a) hexagonal rods, (b) grooved rods, (c) in-plane branched crystals and (d) nonfaceted dendrites. Note that these four types are not the result of sharp transitions but are four main growth forms within a gradual spectrum of primary Cu_6Sn_5 growth morphologies. It can be seen that the hexagonal rods are often hollow which has been explained due to the re-melting of an axial screw dislocation [50] in the centre. Hexagonal rods are bounded by by six {10-10} facets and grow along [0001] [8, 9, 11,

123, 152]. The grooved rods still keep a long rod feature with {10-10} facets, while not maintaining a simple hexagonal shape [8]. In-plane branched primary Cu_6Sn_5 development has been shown to start from Cu_6Sn_5 rod tip splitting where the tips are usually nonfaceted indicating a transition from lateral ledge growth in highly faceted rods to continuous tip growth in the branched crystals which is indicative of an interface roughening transition from an atomically smooth to atomically rough solid-liquid interfaces [11]. It was shown by in-situ imaging in [11] that Cu_6Sn_5 dendrites usually grow with a nonfaceted tip and that the faceting of Cu_6Sn_5 dendrites occurs later during solidification as the dendrites coarsen. The Cu_6Sn_5 dendrite crystallography has been discussed in detail by Xian et al. [11].

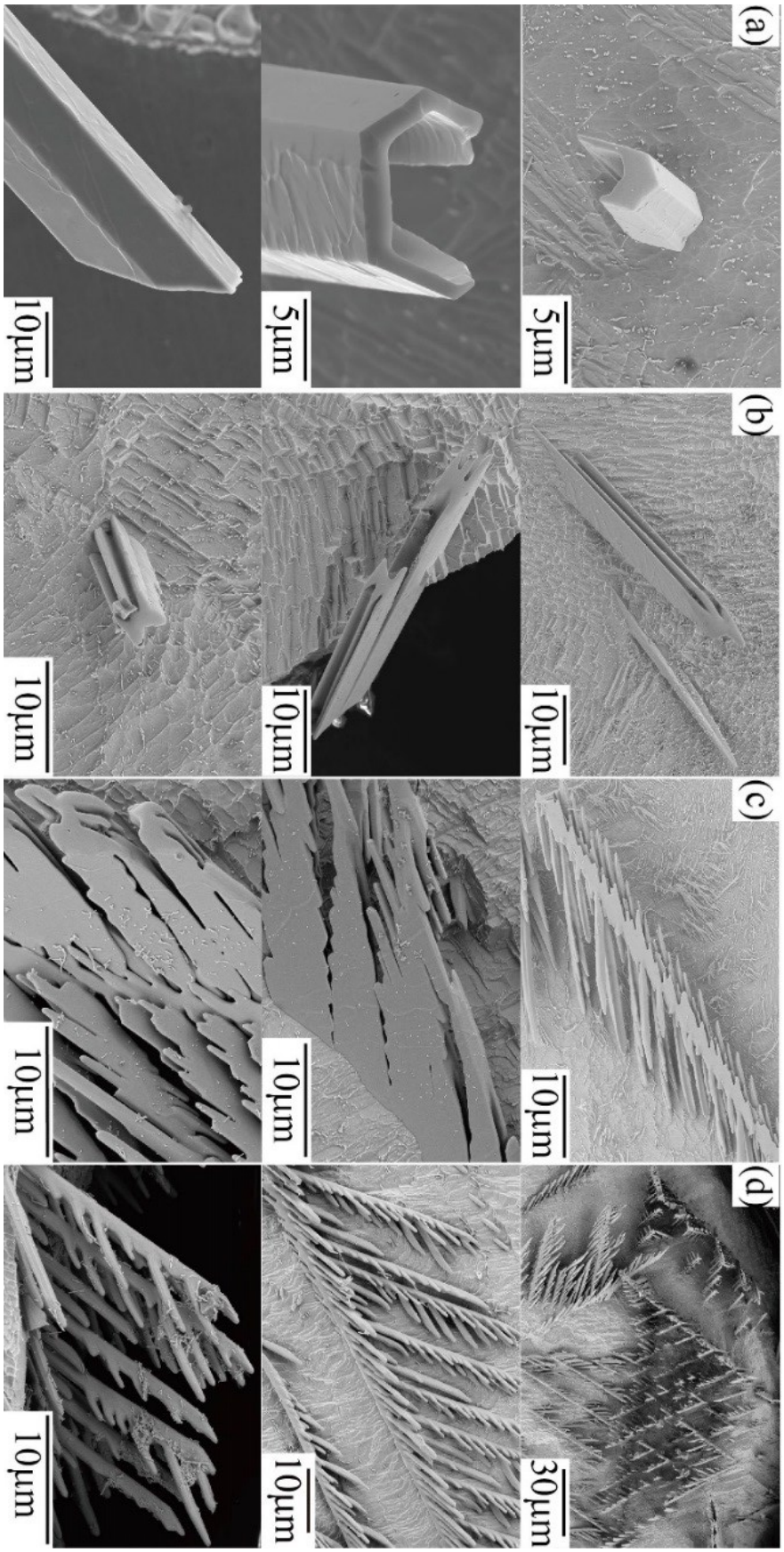


Fig. 58 typical micrographs of primary Cu6Sn5 from shallow etched Sn-0.7wt%Cu/Cu solder joints. (a) hexagonal rod (b) grooved rod (c) in-plane branched and (d) dendrite

3.3.4 Dependence of Cu_6Sn_5 morphology on Cu dissolution and cooling rate

Fig. 59(a)-(d) show typical optical micrographs and SE images of primary Cu_6Sn_5 crystals after holding Sn-0.7wt%Cu/Cu solder joints at 300°C for 10s, 30s, 5min and 30min and then cooling at ~30 K/s. It can be seen that the sample held for 10s contains mainly grooved rods, the samples held for 30s mainly contains in-plane branched crystals, and there is a small portion of dendrites indicated by the small triangular arrays [11]. The samples held for 5min and 30min mainly contained the dendritic Cu_6Sn_5, while a little bit rods at the bottom of the joints. Combining the results Fig. 50(a) and Fig. 59, it can be seen that samples held for 5min and 30 min had similar Cu content, and the main primary Cu_6Sn_5 morphologies in them are dendrites. Meanwhile, with increasing Cu content in samples held for 10s to 30min, the dominant morphologies of primary Cu_6Sn_5 changed from faceted-rods to dendrites.

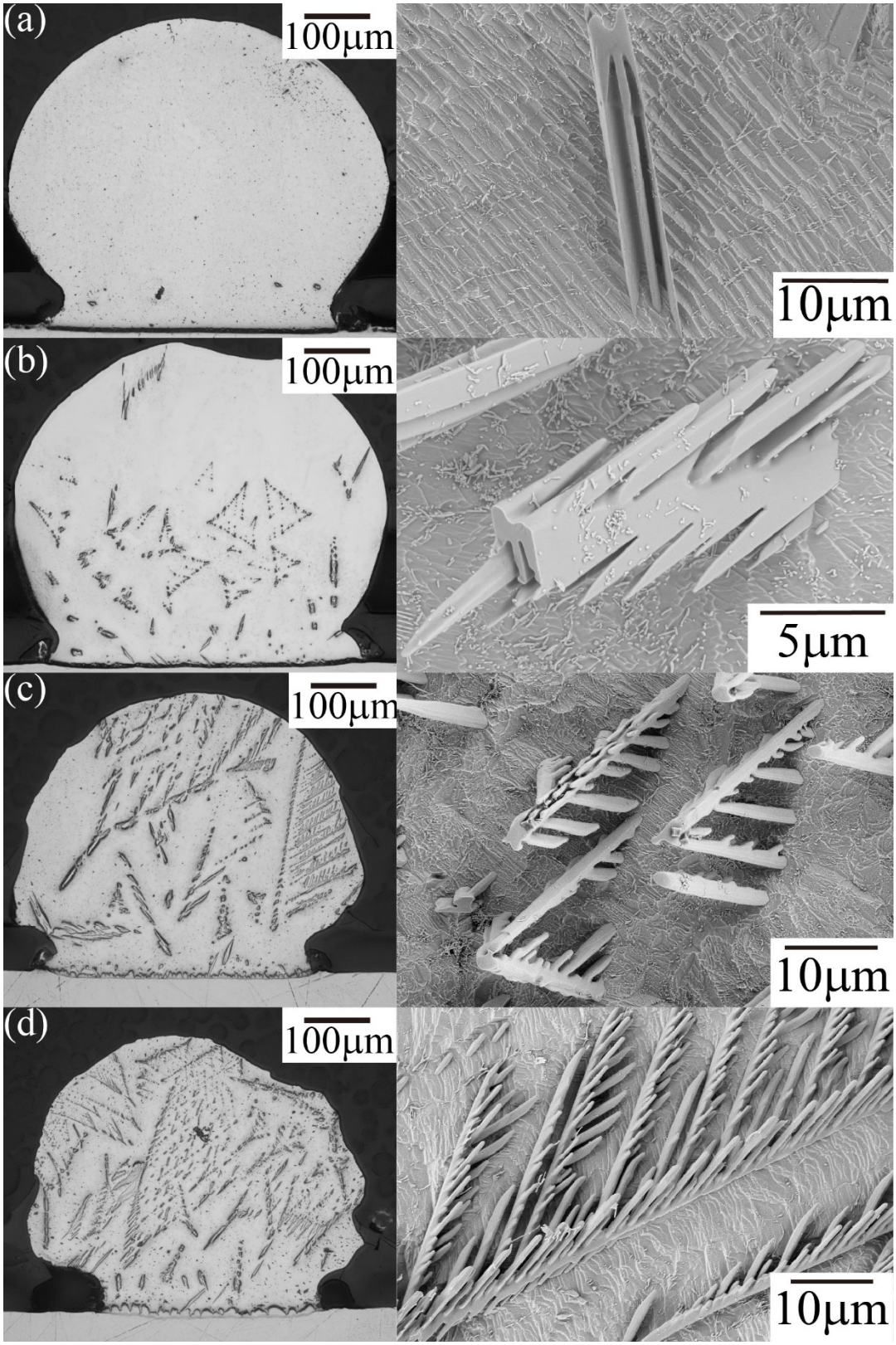


Fig. 59 (a)-(d) typical 2D optical micrographs of Sn-0.7wt%Cu/Cu solder joints held at 300°C for 10s, 30s, 5min and 30min and secondary election images of primary Cu6Sn5 with typical features corresponding to each holding time.

From Fig. 59 it can be also seen that, although the main morphology of primary Cu_6Sn_5 changed with changing mean Cu content in the liquid, there were always some faceted rod-type Cu_6Sn_5 at the bottom area of the joints near the Cu_6Sn_5 reaction layer. This led to a gradation of Cu_6Sn_5 morphology with distance from the Cu_6Sn_5 reaction layer in samples with high Cu content (i.e. long holding time). For example, Fig. 60(a) shows a typical deep etched cross section of a solder joint held at 300°C for 5min followed by cooling at ~30 K/s. It can be seen that the dendrites have grown to span almost the entire solder ball. Many primary Cu_6Sn_5 have grown from the layer and other primary Cu_6Sn_5 seem to have nucleated and grown in the bulk solder as was found in [27]. Fig. 60(b) shows a large primary Cu_6Sn_5 that grew from the Cu_6Sn_5 layer and has a morphology that changes with growth distance from faceted hexagonal rod, to grooved rod, in-plane branched and then dendritic along its growth direction. Note that the debris on the Cu_6Sn_5 are eutectic Cu_6Sn_5 that were not washed off by ultrasonic bathing to ensure that the fine dendrites did not fracture and so as to ensure that the fine dendrite structure was retained.



Fig. 60 (a) typical cross section of a solder joint which has been held at 300°C for 5min within which Sn has been fully etched off (b) a typical large primary Cu_6Sn_5 grown from the layer.

The transition of morphology in one single primary Cu_6Sn_5 growing from the layer can be understood from the heat flow situation upon rapid cooling. The heat flux will be towards the outer surface of the joint where the cooling rate is highest yet many Cu_6Sn_5 grow from the hotter Cu_6Sn_5 layer where there is no nucleation barrier. Therefore, a primary Cu_6Sn_5 crystal growing from the layer grows into liquid with a negative thermal gradient and a near-uniformly saturated composition. Growth into a negative thermal gradient will induce an increasing interface velocity which, in Cu_6Sn_5, causes a transition from faceted to nonfaceted crystal growth [11].

An example of the morphology transition in one Cu_6Sn_5 crystal is overviewed by Fig. 61. Fig. 61(a) shows a hexagonal rod that has developed internal grooves analogous to cooling fins on a heat sink in order to reject Sn more efficiently while maintaining a high interface area of the preferred {10-10} facets. With further growth into the negative temperature gradient, nonfaceted perturbations are apparent near the growth tips (Fig. 61 (b)). The growth of the perturbations creates valleys that become deeper producing in-plane branches which maintain the {10-10} facets (Fig. 61(b)), and multiple such branching events create the in-plane branched morphology. With continued growth into a negative temperature gradient, nonfaceted dendrite branches form (Fig. 61 (c)) and grow with some of the possible <101> directions (close to {1-214} plane normal) [11].

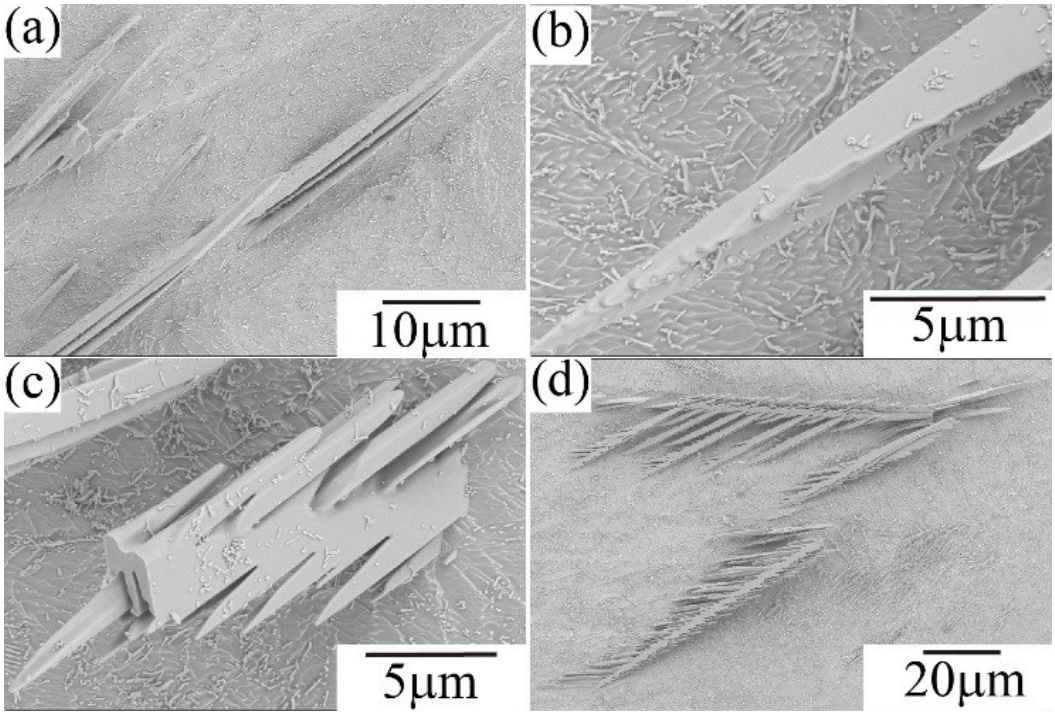


Fig. 61 description of primary Cu_6Sn_5 morphology transformation from hexagonal rod to dendrite.

Although the Cu_6Sn_5 can have a range of morphologies within one joint, one morphology usually occupied the majority of the solder volume because the transition between different morphologies occurred over a relatively short distance. The remainder of this Chapter only considers the dominant morphology in each joint.

Fig. 62 shows solder joints that were held for five minutes at 240°C, 270°C, 300°C, 350°C and 390°C before being cooled at ~2.6 K/s. It is clear that, with increasing peak temperature, the dominant Cu_6Sn_5 morphology changed from grooved rods, to faceted crystals with few in-plane branches to in-plane branched crystals with numerous branches. Since each of these joints was near-uniformly saturated in Cu, it can be seen that the main cause of this morphological transition is the increasing Cu at increasing peak temperature.

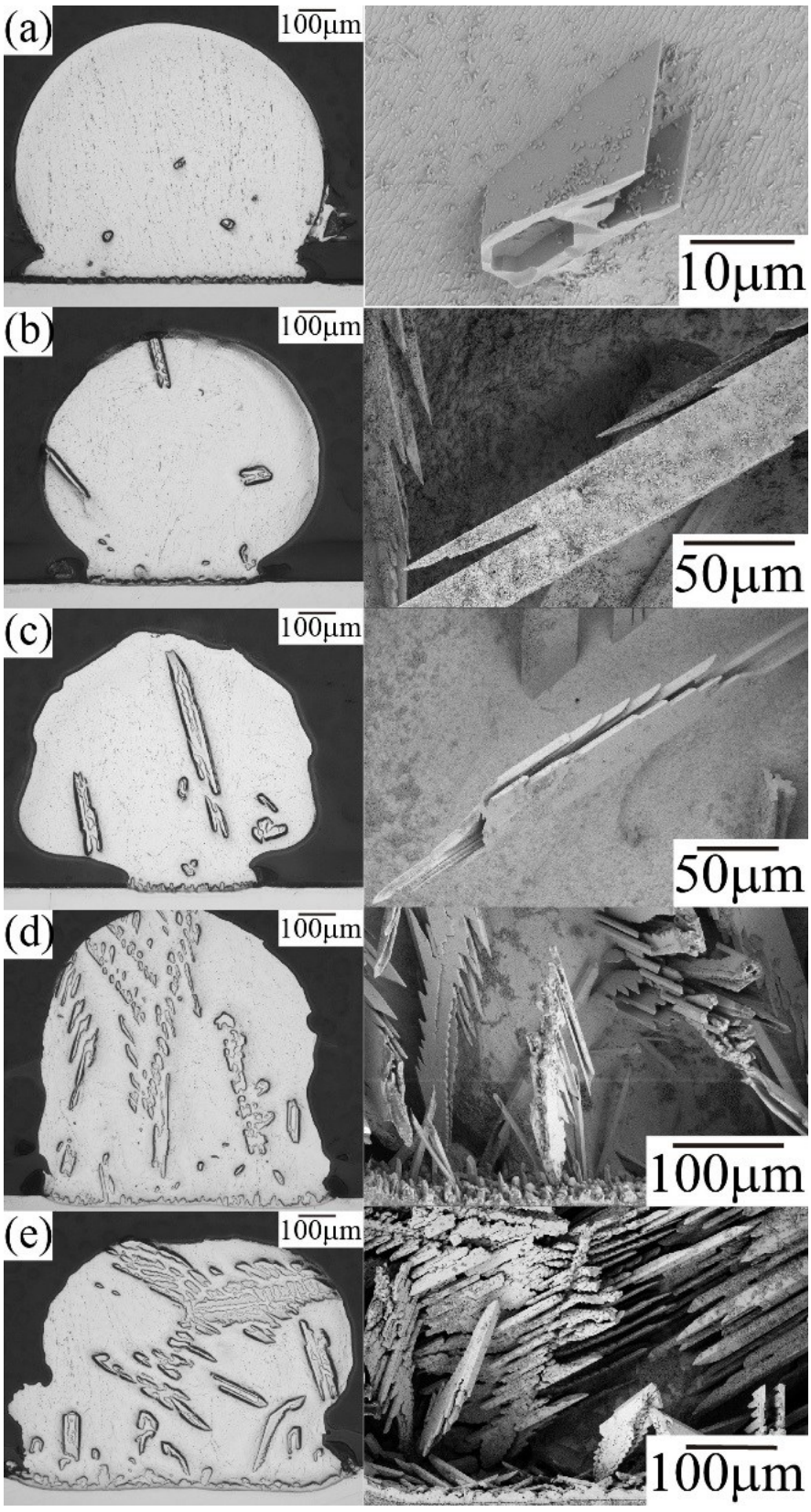


Fig. 62 (a)-(e) solder joints that were held for five minutes at 240°C, 270°C, 300°C, 350°C and 390°C before being cooled at ~2.6 K/s. Left side: full cross-sections showing primary Cu_6Sn_5. Right side: the typical 3D morphology of primary Cu_6Sn_5 after deep etching.

Fig. 63 presents typical examples of Sn-0.7wt%Cu/Cu solder joints which were cooled at three different cooling rates after holding at five different peak temperatures from 240°C to 390°C for 5 min. It can be seen that the primary Cu_6Sn_5 morphology is strongly dependent on the peak temperature and cooling rate. Combining Fig. 59 with Fig. 62 and Fig. 63, it can be seen that the two main factors in determining the primary Cu_6Sn_5 morphology are the Cu dissolution into the liquid and the cooling rate.

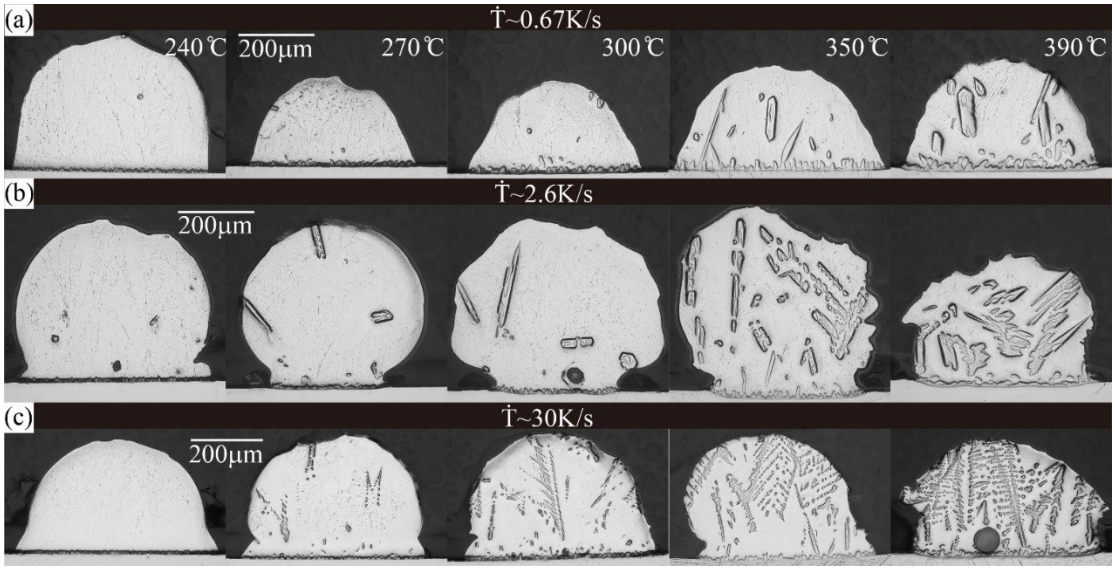


Fig. 63 morphologies of primary Cu_6Sn_5 cooling at (a) ~0.67K/s (b) ~2.6K/s (c) ~30K/s after holding for 5 min at five different peak temperatures. Each column represents same peak temperature, and micrographs in each row share the same scale bar.

Fig. 64 presents a map of cooling rate versus Cu content for Cu_6Sn_5 morphologies extracted from micrographs such as those shown in Fig. 63. The upper x-axis shows the five peak temperatures used for solder joints held for 5 min. The lower x-axis shows the Cu content in the liquid assuming uniform saturation of the solder balls. Five different symbols in the legend depict the main primary Cu_6Sn_5 morphologies. The red datapoints are for Sn-0.7wt%Cu/Cu solder joints from this study, combined with those from reference [11], while the black data points are for primary Cu_6Sn_5 in 0.5g

freestanding solders with compositions ranging from 0.7 – 4.2 wt% Cu from the study in reference [11].

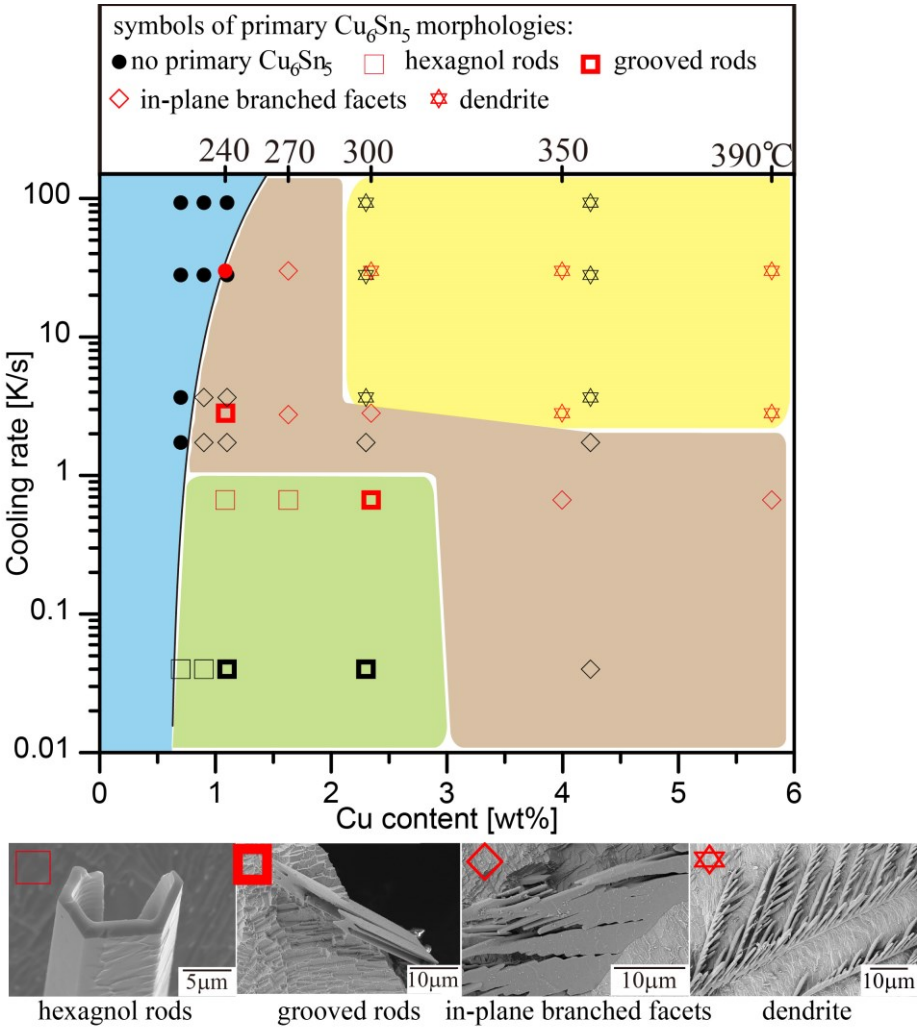


Fig. 64 primary Cu_6Sn_5 morphology map. Black data points: primary Cu_6Sn_5 in large free standing samples [11]. Red data points: primary Cu_6Sn_5 in ~500μm Sn-0.7wt%Cu/Cu solder joints.

It can be seen from Fig. 63 and Fig. 64 that with increasing Cu content and cooling rate, the primary Cu_6Sn_5 morphology undergoes the transition from not existing (blue) to faceted rods (green) to in-plane branched crystals (pink) and finally to dendrites (yellow). Note that for solder joints cooled from 240°C with cooling rate ~2.6K/s, the data point is inside the pink region. This is likely to be because, for a peak temperature

of 240°C, the diffusion rate is lower and it takes a longer time for Cu to saturate the bulk solder so the actual liquid composition is lower than the saturated value. All other points are a reasonable fit to a simple microstructure map that links the mean Cu content in the liquid and the cooling rate to the morphology of primary Cu_6Sn_5.

There is a large body of literature that has observed similar morphologies in different studies [9, 12, 20, 50, 90, 91, 125, 128, 153-155]. The Cu_6Sn_5 morphologies from these studies can be interpreted by the primary Cu_6Sn_5 morphology map in Fig. 64 which can be a useful tool to select process parameters to generate the desired primary Cu_6Sn_5 morphology for electronic solder joints. For example, the heating and cooling rate can be very high in laser soldering, whereas a low peak temperature and low cooling rate is common in BGA soldering, and the cooling rate can vary from large packages to small exposed joints.

3.4 Conclusions

The influence of soldering process parameters i.e. peak soldering temperature, holding time at peak temperature and cooling rate on the dissolution of Cu, and the volume fraction and morphology of primary Cu_6Sn_5 has been investigated in 500μm BGA-type joints of Sn-0.7wt%Cu soldered on Cu substrates.

It has been found that a higher Cu content in the bulk solder, due to Cu substrate dissolution, resulted from longer holding time and higher peak soldering temperature, which can be understood from the phase diagram and the Nernst-Brunner effect. In turn, the higher Cu content in the liquid resulted in a higher volume fraction of primary Cu_6Sn_5 and a morphology transition of primary Cu_6Sn_5 from faceted rods to non-faceted dendrites at high cooling rate. The interfacial Cu_6Sn_5 layer thickness increased near linearly with the square root of holding time at 300°C, indicating the growth of the layer is controlled by volume diffusion through the layer. Large primary Cu_6Sn_5 crystals have been observed to grow from pre-existing Cu_6Sn_5 crystals in the interfacial layer and grow to fill the whole joint, containing the morphology transition from faceted to non-faceted with increased growth distance which can be understood as growth into a negative temperature gradient. A quantitative study of the relationship between Cu dissolution from the substrate and that gained due to growth of both the IMC layer(s) and primary Cu_6Sn_5 under various holding times and peak temperatures have been presented. A simple equation linking the Cu dissolved and that gained by IMCs has been derived:

$$m_{Cu} = 0.36L_{Cu_6Sn_5}^{layer}A_{pad}\rho_{Cu} + 0.78L_{Cu_3Sn}^{layer}A_{pad}\rho_{Cu} + 0.36V_{solder}g_{Cu6Sn5}^{primary}\rho_{Cu}$$

It has been shown using this equation and the measurements of primary Cu_6Sn_5 fractions and interfacial layer thicknesses that the Cu substrate dissolution was mainly due to interfacial IMC layer growth at low peak temperature and after the saturation of liquid solder with Cu, whereas the Cu substrate dissolution was mainly due to saturating the liquid in Cu at higher peak temperature.

A morphology map for primary Cu_6Sn_5 of cooling rate versus Cu content and peak reflow temperature has been built which can be used to select different soldering process parameters to grow primary Cu_6Sn_5 with preferred morphologies and volume fractions.

Chapter 4. Real-time imaging of primary Cu_6Sn_5 evolution during the reflow soldering of Sn-xCu/Cu joints

4.1 Introduction

In the previous Chapter, substrate dissolution and the cooling rate were shown to significantly affect the volume fraction and morphology of primary Cu_6Sn_5. However, all conclusions were based on *post mortem* analyses of fully solid samples. In recent years, there have been major developments in the *in situ* imaging of solidification phenomena using X-ray techniques on both synchrotron [27-35] and laboratory X-ray sources [156-158]. This Chapter applies synchrotron radiography to the observation of primary Cu_6Sn_5 in solder joints with a focus on the dynamics and kinetics of primary Cu_6Sn_5 formation in Sn, Sn-0.7Cu and Sn-2Cu (wt%) soldered on copper substrates. The first two alloys (Sn, Sn-0.7Cu) are hypereutectic and will dissolve Cu into the liquid during soldering. The third alloy (Sn-2Cu) is hypereutectic and has a Cu_6Sn_5 liquidus that is higher than common reflow temperatures in reflow soldering. Thus, Sn and Sn-0.7Cu are studied to examine primary Cu_6Sn_5 formation due to Cu dissolution and Sn-2Cu is studied to examine the effect of only partially dissolving the Cu_6Sn_5 during reflow. Two Sn-2Cu are investigated; one with a small initial Cu_6Sn_5 size and one with a large initial Cu_6Sn_5 size to test whether the final primary Cu_6Sn_5 size in solder joints can be engineered by only partially remelting the primary Cu_6Sn_5 during reflow.

4.2 Experimental Methods

4.2.1 Sample preparation.

Sn, Sn-0.7Cu and Sn-2Cu (wt%) solder alloys were cast and rolled to foils with area of ~ 10mm x 10mm and 100μm thickness. The primary Cu_6Sn_5 with small size in Sn-2wt%Cu was achieved by rolling the alloy the ingot down to 100μm which fractured the primary Cu_6Sn_5 into small fragments, while the primary Cu_6Sn_5 with large size was achieved by assembling the solder foil after rolling in between two SiO_2 plates and then holding this in a furnace at 210^0C for two weeks to coarsen the Cu_6Sn_5. Specimen cells were produced as shown in the schematic diagram in Fig. 65. They include a Cu sheet of 100μm thickness to act as a substrate and a solder foil with a thin coating of a ROL-1 flux, placed within a cavity in a 100 μm thick polytetrafluoroethylene (PTFE) spacer sheet with an observation window of 10 x 10 mm^2 and a vent for flux outgassing. Finally, the solder foil, substrate and PTFE were secured between two quartz plates.

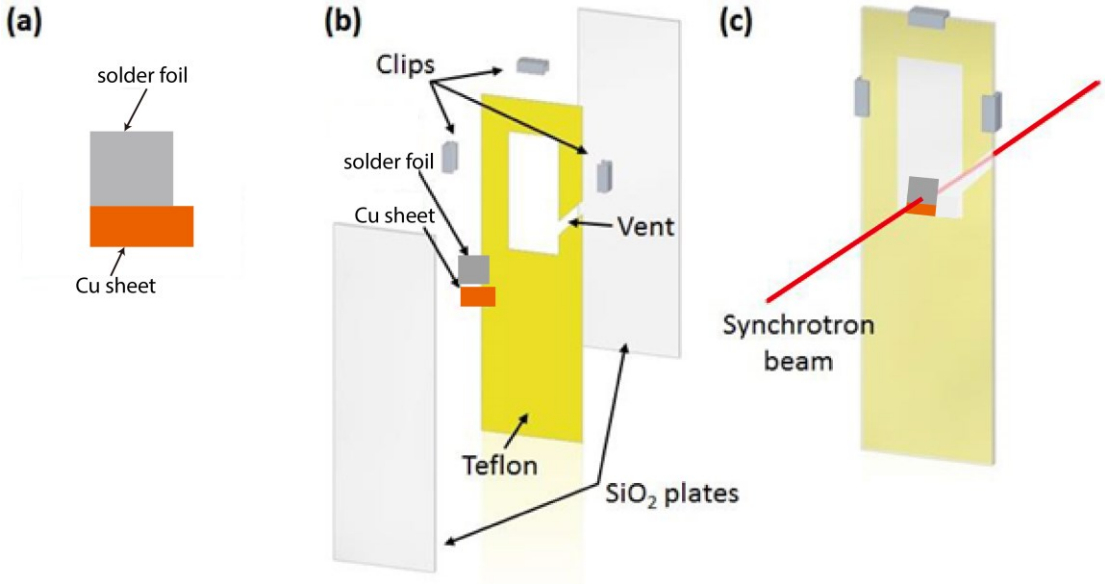


Fig. 65: Schematic diagram of in situ soldering specimen cell. (a) fluxed solder foil on a Cu substrate. (b) Individual parts of the sample cell. (c) Assembled parts of the sample cell. Note that the image is not to scale.

4.2.2 Synchrotron X-ray Imaging.

Experiments were conducted on BL20XU at the SPring-8 synchrotron in Hyogo, Japan. A planar undulator was used as an X-ray source and Si double crystal monochromators were used to produce an X-ray energy of 21 keV. The apparatus and solidification imaging setup within the hutch is shown in Fig. 66, which is similar to that developed in previous research [27-29]. The transmitted images were converted into visible light and recorded in a digital format with 2,000 X 2,000 pixels at 1 mm X 1 mm field of view giving a resolution of 0.477 μm per pixel. An exposure time of 120 ms per frame with 1 frame per second was used. A radiation furnace with graphite heating elements applied a reflow profile that heated from room temperature to approximately 250 ^{0}C at 0.33 ^{0}C/s, held at this peak temperature for 30 s before cooling down at approximately 0.33 ^{0}C/s. temperature was recorded by a thermocouple placed close to (within 2mm of) the sample. The observation of βSn-Cu_6Sn_5 eutectic melting was used to calibrate the thermocouple by identifying an appropriate offset.

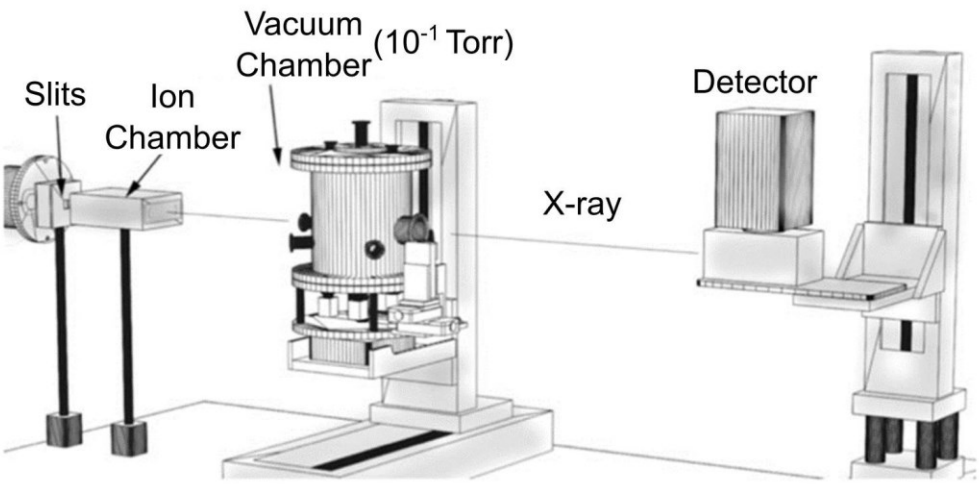


Fig. 66 schematic drawing of synchrotron hutch with apparatus [12]

4.2.3 X-ray image processing

For the intensity (in the range 0-255 for 8-bit image) of each pixel in the image (a 1920 x 1440 matrix), flatfield correction was used as described in the following equation, to form a new processed image (a new 1920 x 1440 matrix).

$$\mathrm{ffc}_i(\mathrm{x,y}) = \frac{[R_i(x,y) - D_i(x,y)]m}{F_i(x,y) - D_i(x,y)} \qquad \text{Equation 61}$$

where (x,y) is each pixel coordination in the image/matrix , and the pixel quantity is an intensity value (0-255 for 8-bit image); ffc is a flatfield corrected image (a 1920 x 1440 matrix); R is a raw transmitted radiograph (a 1920 x 1440 matrix); D is the 'dark' image collected by the detector when the X-ray beam is turned off (a 1920 x 1440 matrix); m is the average intensity of the raw transmitted radiograph (a number); F is the 'direct' image collected by the detector when the X-ray beam is on with no sample in the beampath (a 1920 x 1440 matrix); and i in the suffix represents the frame number.

The obtained Images (Fig. 67 (a)) after flatfield correction were then blurred using Gaussian filter with a sigma radius of 30 pixels. The Gaussian filed blurred images (Fig. 67 (b)) were used as background showing the intensity variations due to flux bubbles. Finally, the normalized images (Fig. 67 (c)) were gotten by normalization of the flatfield corrected images (Fig. 67 (a)) against the blurred images (Fig. 67 (b)) with the equation:

$$\frac{ffc_i(x,y)}{blurred_i(x,y)}m \qquad \text{Equation 62}$$

where ffc is flatfield corrected images, blurred is the Gaussian blurred image and m is the average of raw images, suffix i represents the ith frame.

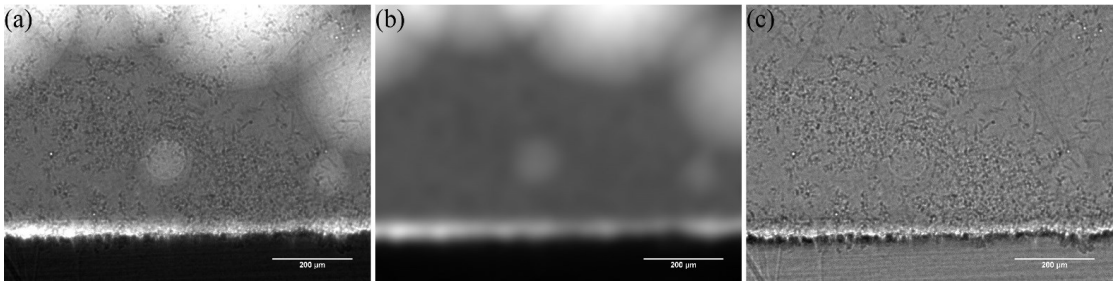


Fig. 67 selected image (frame 600) from image sequences of Sn-2wt%Cu/Cu with small primary Cu_6Sn_5, showing (a) after flatfield correction (b) flatfield corrected image after Gaussian blurred (c) normalized image

4.3 Results and Discussion

Fig. 68 (a) shows the soldering thermal profile of CP Sn onto a Cu substrate and four selected frames that were extracted from the synchrotron radiographs sequence. Fig. 68 (b) shows the moment 15 seconds after the solder fully melted and wet the Cu substrate, it can be seen that a thin layer of Cu_6Sn_5 developed at the interface. Fig. 68 (c) shows a frame during holding at the peak temperature of ~250℃, which appears similar to Fig. 68(b). Note that Cu dissolution cannot be directly observed because the changing Cu content in the liquid does not provide significant absorption contrast in this system. Fig. 68 (d) shows the moment a bit above CP Sn melting point during cooling, and Fig. 68 (e) shows the moment that the temperature was ~185℃ and the joint was solidified. It can be seen from Fig. 68 (e) that no primary Cu_6Sn_5 formed during cooling. This can be understood by Nernst-Brunner parameter:

$$\frac{At}{V}$$

Where t is the time for diffusion, A is the contact area between the solder and the substrate, and V is the volume of solder. It can be seen from the set up in Fig. 65, that the thin solder foil has been constrained within a 100 μm thick cavity between two SiO_2 plates. Therefore the contacting area (A) is very small ~100 μm, so the ratio of A/V is very small, therefore the time required for liquid solder to reach equilibrium is long which means the diffusion rate is slow and before cooling the Cu content in the liquid is very small. Taken time, t, is the holding time at peak temperature 30s, the Nernst-Brunner parameter is 0.003s/μm which corresponds to very low Cu content in bulk solder (Fig. 50). It has also been shown in Chapter 3 that if the soldering peak

temperature is around 240-250℃ (Fig. 57), the Cu dissolution from the layer will mainly contribute to the growth of interfacial layer. Therefore, no primary Cu_6Sn_5 has been observed after solidification.

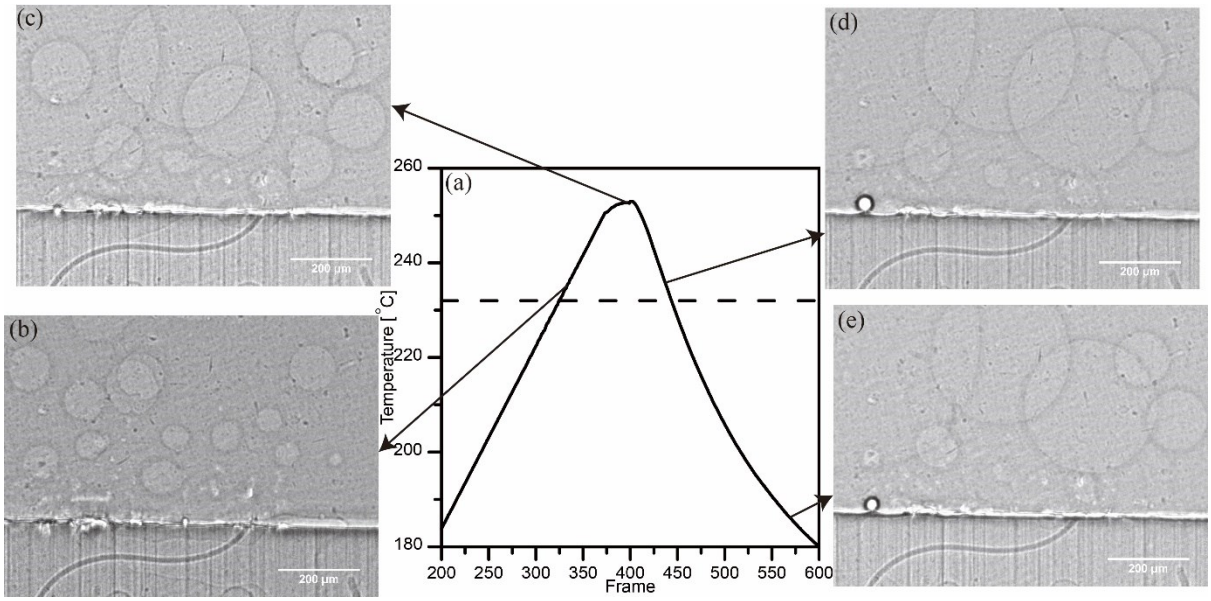


Fig. 68 (a) Thermal profile of soldering CP Sn onto Cu substrate, dashed line indicates melting temperature of pure Sn 232℃. Typical frames were selected from synchrotron radiography of 1 frame per second (b) frame 340 (c) frame 400 (d) frame 439 (e) frame 520.

Fig. 69 shows the thermal profile and typical radiograph frames of soldering Sn-0.7wt%Cu onto a Cu substrate. The interfacial Cu_6Sn_5 can be seen from Fig. 69(b). During cooling, the nucleation and growth of primary Cu_6Sn_5 in bulk solder is clear and two primary Cu_6Sn_5 have been indicated by black arrows in Fig. 69 (d). It can be seen one primary Cu_6Sn_5 is needle-like and another is X-shape. Although the Sn-0.7wt%Cu is a hypo-eutectic composition, the primary Cu_6Sn_5 formed because Cu dissolution from the Cu substrate was sufficient to increase the total Cu content in the liquid into the hyper-eutectic region. In Fig. 69 (d)-(e)-(f) black arrows indicate the growth of two primary Cu_6Sn_5. At the same time, the growth of three primary Cu_6Sn_5

from the interfacial Cu_6Sn_5 layer occurred as indicated by the red arrows. Fig. 69 (f) shows the solder joint was solidified and the arrows represent the primary Cu_6Sn_5 which were indicated in Fig. 69 (d) and (e). From Fig. 69 (d) to (e), although the temperature is below the eutectic temperature, the primary Cu_6Sn_5 was still growing because βSn did not nucleate due to the large undercooling required for βSn nucleation. At these temperatures it is expected that the Cu_6Sn_5-L interfaces are following the metastable Cu_6Sn_5 liquidus line.

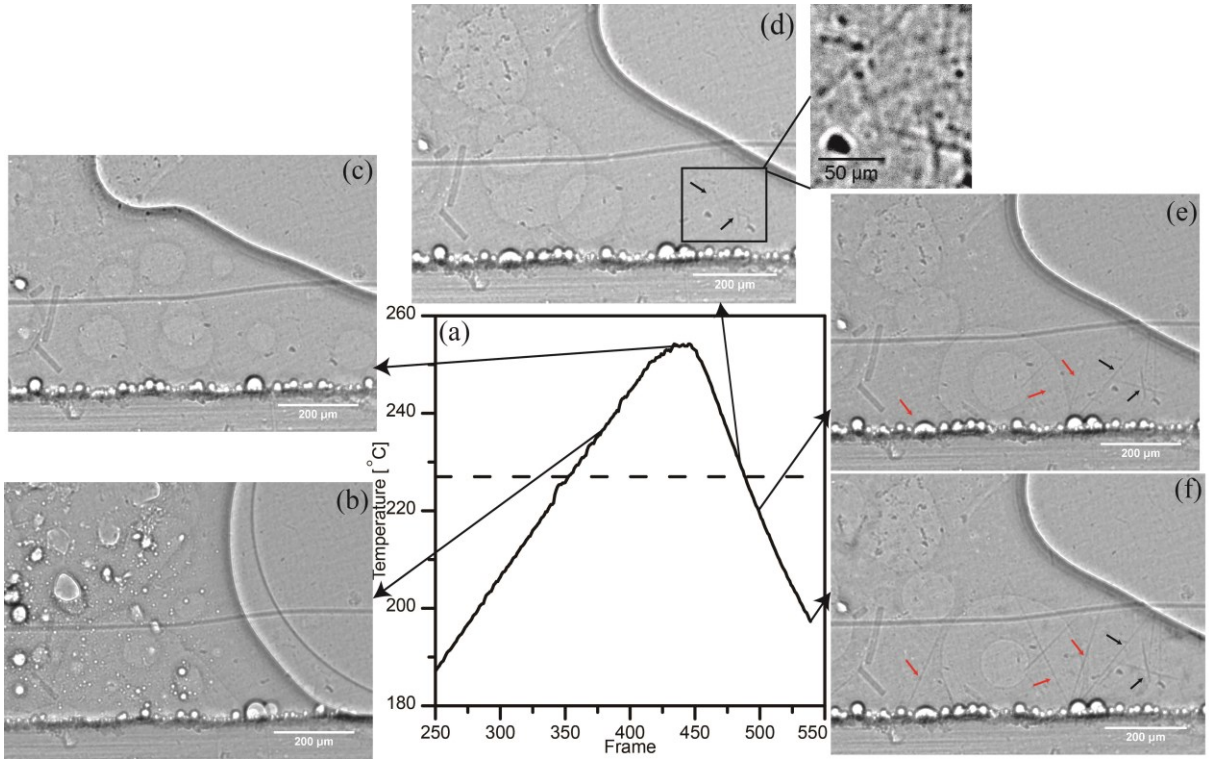


Fig. 69(a) Thermal profile of soldering Sn-0.7Cu onto Cu substrate, dashed line indicates the eutectic temperature 227 ℃. Typical frames were selected from synchrotron radiography of 1 frame per second (b) frame 382 (c) frame 440 (d) frame 487(e) frame 498 (f) frame 520. (black arrow: primary Cu_6Sn_5 nucleated in the bulk solder, red arrows: primary Cu_6Sn_5 grew from pre-existing interfacial Cu_6Sn_5 crystals)

Fig. 70 shows the thermal profile and selected frames for a Sn-2wt%Cu preform that initially contained small primary Cu_6Sn_5. The liquidus temperature for Sn-2wt%Cu is

~287℃ [97], therefore for the peak temperature shown in Fig. 70 (a), the primary Cu_6Sn_5 originally existing in the solder foil is not expected to fully melt during soldering. Comparing Fig. 70 (b) showing the moment below the eutectic temperature when the solder is still solid and Fig. 70 (c) where the solder foil has fully melted and wetted the Cu substrate, a clear interfacial Cu_6Sn_5 layer can be observed. From Fig. 70 (c) to (e) which show the process of liquid heating and the holding stage, it can be seen that more and more small primary Cu_6Sn_5 settle down towards the Cu_6Sn_5 layer at the bottom of the joint due to gravity. These small primary Cu_6Sn_5 were pre-existing in the solder foil and did not fully melt at the peak reflow temperature. From Fig. 70 (f) showing the liquid cooling stage and (g) showing the stage after full solidification, it can be seen that additional needle-like primary Cu_6Sn_5 nucleated and grew in the bulk solder, and grew to much larger size than the un-melted primary Cu_6Sn_5. This creates two populations of primary Cu_6Sn_5: (i) numerous small particles that were originally present in the initial preform and (ii) fewer larger rods that nucleated and grew during cooling from the peak temperature. It can be seen that the newly nucleated Cu_6Sn_5 rods form in regions depleted in Cu_6Sn_5 by the settling small pre-existing Cu_6Sn_5.

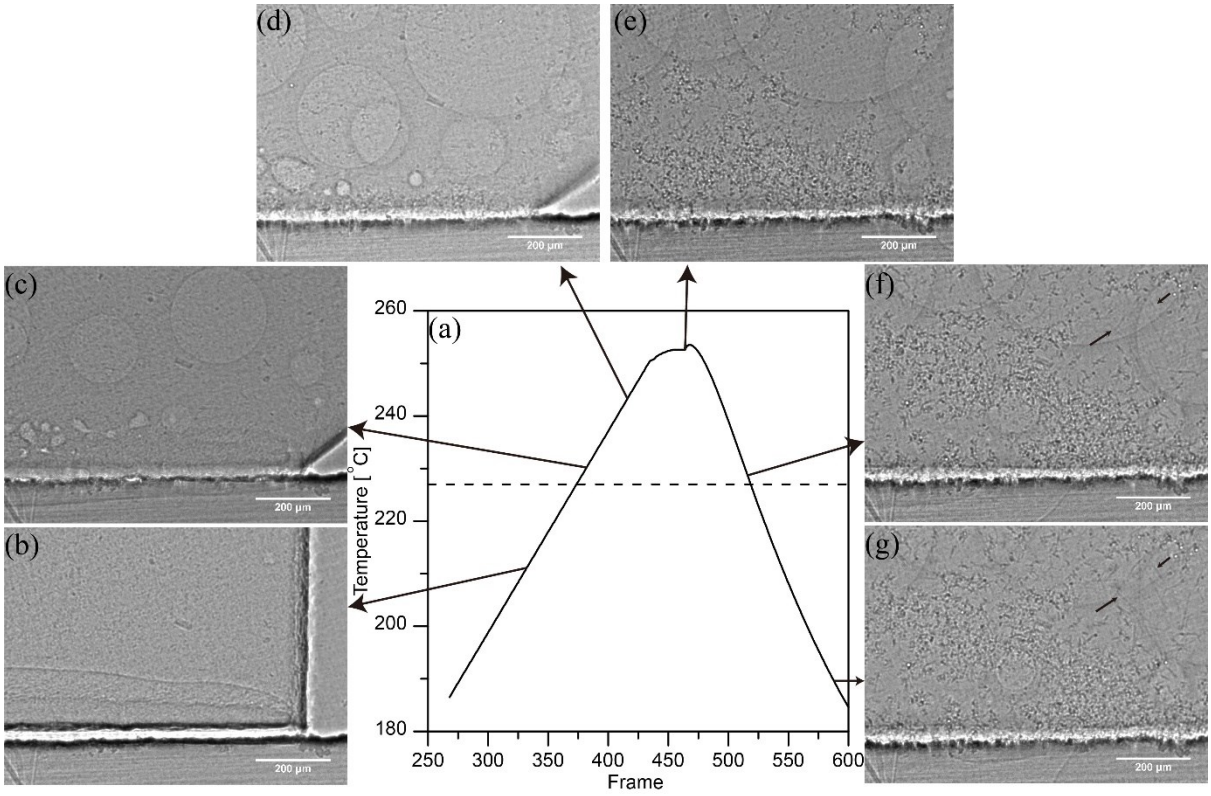


Fig. 70 (a) Thermal profile of soldering Sn-2wt%Cu containing small primary Cu_6Sn_5 onto Cu substrate, dashed line indicates the eutectic temperature 227℃. Typical frames were selected from synchrotron radiography of 1 frame per second (b) frame 330 (c) frame 379 (d) frame 403 (e) frame 470 (f) frame 528 (g) frame 590. (black arrow: primary Cu_6Sn_5 nucleated in the bulk solder).

Fig. 71 presents the thermal profile and selected frames for soldering a Sn-2wt%Cu preform that initially contained large primary Cu_6Sn_5 onto a Cu substrate. Comparing Fig. 71 (b) showing a moment just after the liquid solder wet the Cu substrate with black arrows indicating the pre-existing primary Cu_6Sn_5 and Fig. 70 (c) which is at the similar temperature as that of Fig. 71 (b), it can be seen that the pre-existing primary Cu_6Sn_5 are much larger in Fig. 71 (b). These large pre-existing primary Cu_6Sn_5 undergo partial-remelting and then growth in both the longitudinal and lateral directions throughout the soldering process. Three typical examples are indicated by black arrows in images from Fig. 71 (b) to (e). The nucleation and growth of new primary Cu_6Sn_5

also occurred as indicated by the red arrows from Fig. 71 (d) and (e) and they grew into a long needle-like or morphology with a hollow center. In contrast, the pre-existing primary Cu_6Sn_5 still grow into a morphology similar to the initial morphology in the preform. At the same time, Fig. 71 (e) also shows that the large primary Cu_6Sn_5 tend to remain in the bulk solder instead of settling down to the Cu_6Sn_5 layer. This is presumably because they are attached to the surface oxide of the thin samples since a larger negative buoyancy force acts on larger particles. To test this hypothesis, the location of large primary Cu_6Sn_5 has been examined in Sn-2wt%Cu/Cu joints with similar method of manipulating primary Cu_6Sn_5 size. In Fig. 72, it can be seen that some large primary Cu_6Sn_5 (yellow circled) areattached to the surface oxide of the solder ball.

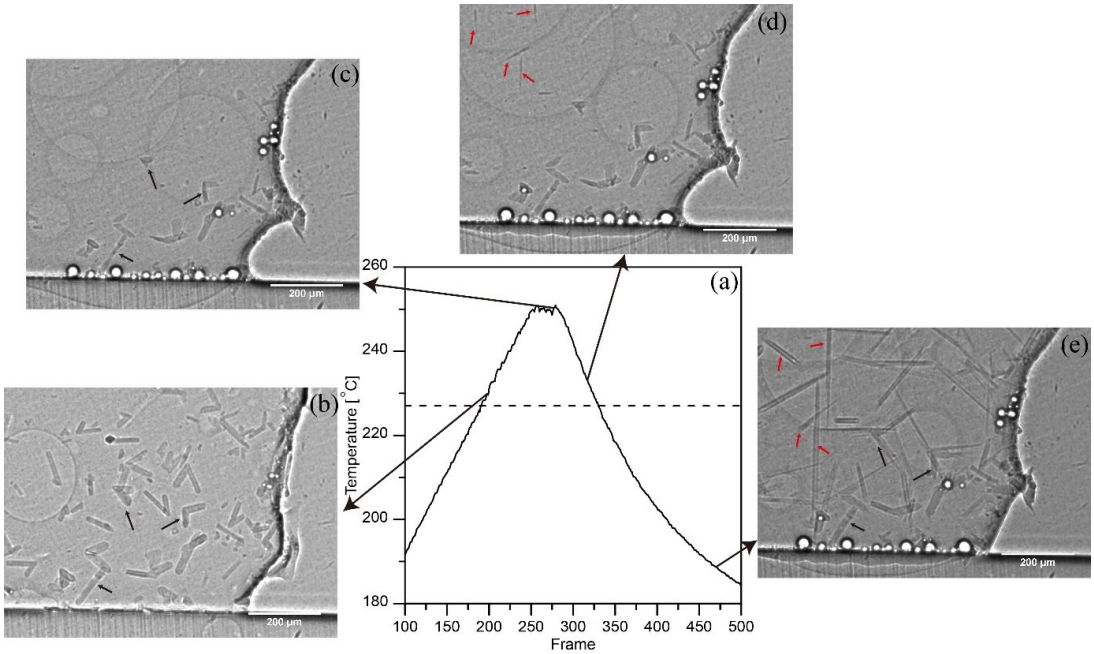


Fig. 71 (a) Thermal profile of soldering Sn-2wt%Cu containing large primary Cu_6Sn_5 onto Cu substrate, dashed line indicates the eutectic temperature 227℃. Typical frames were selected from synchrotron radiography of 1 frame per second (b) frame 195 (c) frame 280 (d) frame 316 (e) frame. (black arrow: primary Cu_6Sn_5 pre-existed in solder foil, red arrows: primary Cu_6Sn_5 nucleated and grew in the bulk solder).

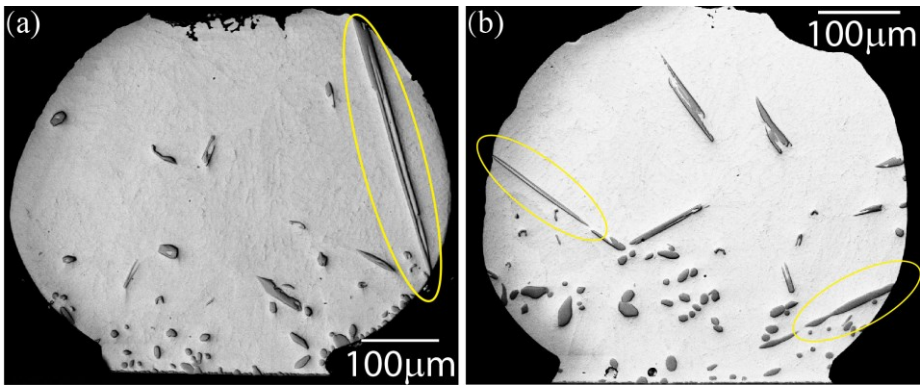


Fig. 72 cross section of Sn-2wt%Cu/Cu containing manipulated large primary Cu_6Sn_5

Comparing Fig. 70 (g) and Fig. 71 (e) after complete solidification, it can be seen that the mean primary Cu_6Sn_5 size in Fig. 71 (e) is much larger which indicates that the primary Cu_6Sn_5 size can be successfully controlled by altering the solder composition and peak temperature so that the primary Cu_6Sn_5 do not fully remelt and ensuring that the primary Cu_6Sn_5 are very small in the initial solder. However, in binary SnCu/Cu joints, this requires compositions that will give a relatively high volume fraction of primary Cu_6Sn_5 which is likely to be undesirable. While this approach may not be useful in binary SnCu/Cu joints, it may be more applicable to higher order solder systems since certain transition metals can greatly steepen the Cu_6Sn_5 liquidus line/surface. For example, in the Sn-Cu-Ni system the composition Sn-0.7Cu-0.05Ni (wt%) is hypereutectic but produces only a small volume fraction of primary $(Cu,Ni)_6Sn_5$ [91].

4.4 Conclusions

The influence of Cu content and the initial size of primary Cu_6Sn_5 on primary Cu_6Sn_5 microstructure development have been studied in 10mm×10mm×100μm Sn-x wt%Cu (x=0, 0.7, 2) solder foils on Cu substrates using *in situ* synchrotron radiography.

It has been found that, during soldering, no primary Cu_6Sn_5 formed in CP Sn/Cu joints. This is due to insufficient Cu dissolved from the Cu substrate into the liquid solder which can be understood by the Nernst-Brunner parameter due to the low ratio of pad area to solder volume (A/V), and relatively short holding time (30s) and soldering peak temperature (~245-250℃). Thus, for the conditions used here, the dissolved Cu from the substrate mainly contributed to the growth of the interfacial Cu_6Sn_5 layer. This is consistent with what was shown in Chapter 3 of this work.

In Sn-0.7wt%Cu/Cu joints, although it is originally hypo-eutectic, primary Cu_6Sn_5 were observed during soldering, indicating that the Cu dissolved from the substrate into the liquid solder increased the Cu content into the hyper-eutectic region. These primary Cu_6Sn_5 have been observed to either nucleate and grow in the bulk solder or grow from the pre-existing Cu_6Sn_5 crystals in the interfacial Cu_6Sn_5 layer. Two morphologies of primary Cu_6Sn_5, needle-like and X-shaped, were observed.

In Sn-2Cu/Cu joints, the pre-existing primary Cu_6Sn_5 did not fully remelt during soldering at a peak temperature of ~250℃. The interfacial Cu_6Sn_5 layer was clearly observed, and pre-existing small primary Cu_6Sn_5 contained in Sn-2wt%Cu settled down to the Cu_6Sn_5 layer due to gravity, while the pre-existing large primary Cu_6Sn_5 did not. Instead, large pre-existing primary Cu_6Sn_5 underwent remelting and growth in both the

longitudinal and lateral directions and maintained their original morphologies. Primary Cu_6Sn_5 also nucleated and grew in the bulk solder into long rods often with a hollow center. Newly nucleated primary Cu_6Sn_5 rods did not settle down to the layer in joints containing small and large pre-existing primary Cu_6Sn_5, indicating that they may be attached to the surface oxide of the solder foil.

This Chapter shows that the mean primary Cu_6Sn_5 size in solder joints can be controlled by using a hyper-eutectic solder composition whose Cu_6Sn_5 liquidus is higher that the peak reflow temperature so that the primary Cu_6Sn_5 does not fully remelt during soldering. While, in binary SnCu/Cu joints, this requires compositions that will give a relatively high volume fraction of primary Cu_6Sn_5 which is likely to be undesirable, the approach may be more applicable in higher order systems with steeper Cu_6Sn_5 liquidus line/surface. The ability to control the Cu_6Sn_5 size is also useful for studies on the effects of microstructure on solder joint reliability. This is considered in the next Chapter.

Chapter 5. The influence of primary Cu_6Sn_5 size on the shear impact properties of Sn-Cu/Cu BGA joints

5.1 Introduction

In the previous Chapter, solder joint microstructure development under the influence of Cu content and the size of pre-existing primary Cu_6Sn_5 was observed and analysed by *in situ* real time synchrotron radiography. It was shown that the mean primary Cu_6Sn_5 size could be controlled by the combined effects of the selected Cu content in the initial solder and the peak soldering temperature. Cu_6Sn_5 has been shown to be important in the reliability of solder joints; however, the majority of research has focused on the interfacial Cu_6Sn_5 layer [40-48] and much less has considered the primary Cu_6Sn_5 crystals [43, 49, 50]. This Chapter applies the method of manipulating the mean primary Cu_6Sn_5 size in 500μm Sn-2wt%Cu/Cu BGA joint while keeping the remaining microstructure near constant, and applies ball shear testing on a DAGE-4000 bond-tester with 10mm/s to fracture the BGA joints through the bulk solder and research the influence of primary Cu_6Sn_5 size on the shear impact properties of the joints.

5.2 Experimental Methods

Sn-2wt%Cu alloy was prepared by mixing 99.9wt%Sn and Sn-10wt%Cu ingots in a graphite crucible, heating and holding at 450℃ for 4 hours, and then pouring into a steel mould. The composition of the alloy was analyzed by X-ray fluorescence (XRF)

spectroscopy to be 2.1wt% Cu with impurities of Pb, Ag, Sb less than 0.02wt%, and Zn, Fe, Al, As, Cd less than 0.001wt%. The as-cast alloy was then rolled to foil with thickness ~0.03mm, punched into circular discs with diameter ~1.6mm and melted with a ROL1 tacky flux (IPC J-STD- 004) at ~350℃ on a hot plate to form solder balls with diameter 500±25 μm due to surface tension.

A method was developed to manipulate the primary Cu_6Sn_5 size in the initial freestanding solder balls and then largely maintain this primary Cu_6Sn_5 size in solder joints. To obtain the 'smallest' primary Cu_6Sn_5 size, liquid Sn-2Cu solder balls were quenched in ethanol from 350°C. To obtain a 'small' primary Cu_6Sn_5 size, liquid solder balls were solidified from 350°C under an air extractor. To obtain a 'medium' primary Cu_6Sn_5 size, balls cooled with an air extractor were aged at 150℃ for 2 weeks. To obtain the 'largest' primary Cu_6Sn_5 size, balls cooled with an air extractor were aged at 210℃ for 2 weeks.

Solder balls produced by each of the four procedures were then reflowed on standard FR4 test boards with 500μm Cu-OSP pads in a LFR400HTX TORNARDO reflow oven (Surface Mount Technology, Isle of Wight, UK) with thermal profile shown in Fig. 73(a).

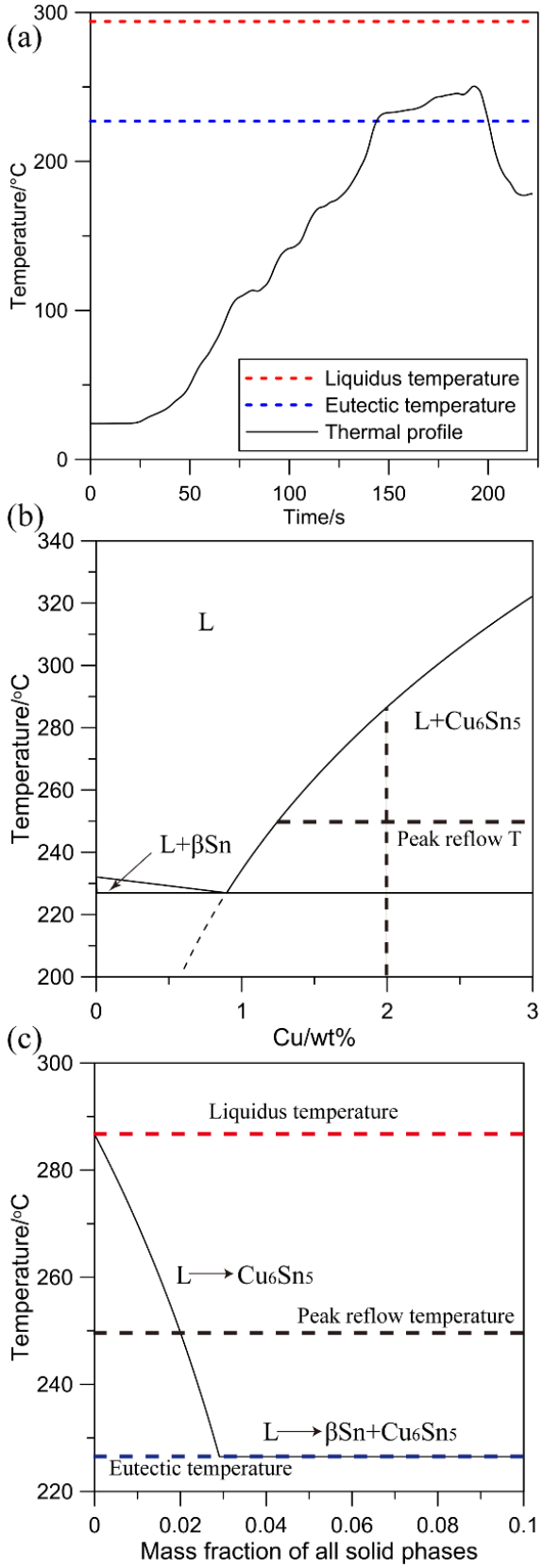


Fig. 73 (a) Thermal profile used for reflow soldering. (b) Sn-Cu phase diagram [42] highlighting the initial solder composition and the peak reflow temperature (c) Mass fraction of primary Cu_6Sn_5 as a function of temperature in Sn-2Cu [42].

From Fig. 73 (b), it can be seen that under this reflow profile, the peak temperature is lower than the Cu_6Sn_5 liquidus temperature of Sn-2wt%Cu. Thus, the primary Cu_6Sn_5 only partially remelt during reflow and the primary Cu_6Sn_5 size in the final joint retains features from the initial primary Cu_6Sn_5 in the solder ball. It can be seen from Fig. 73 (c) that partial melting of primary Cu_6Sn_5 leaves ~2 mass% primary Cu_6Sn_5 remaining at the peak temperature, while cooling to the eutectic temperature increases the amount of primary Cu_6Sn_5 to 2.8%, so that most of the Cu_6Sn_5 from the freestanding solder ball is not remelted during reflow. With this approach using Sn-2Cu, the primary Cu_6Sn_5 microstructures in the initial freestanding balls were largely maintained after soldering.

After reflow, the as-soldered joints were washed in ethanol in an ultrosonic bath to remove residual flux. BGA impact shear testing was performed on a DAGE-4000 following standard procedures in JESD22-B117B [159]. In order to investigate only the influence of primary Cu_6Sn_5 on the shear impact properties of solder joints, it is necessary to have solder joints fracture through the bulk solder and not the interfacial Cu_6Sn_5. Therefore, a 10mm/s displacement rate was selected. The hammer height was set at 50μm, the hammer speed was 10mm/s and the layout of the impact shear tester is illustrated in Fig. 74. Using $\frac{dx}{dt} \times \frac{1}{h}$ where h is the solder ball height, the global strain rate is $20s^{-1}$. Since deformation is heterogeneous, it can only be stated that the strain rate is approximately on the order of 10^1 s^{-1}. For comparison, the strain rate in creep testing is in the order of 10^{-6}~10^{-1} s^{-1} for Sn-3.5wt%Cu, Sn-3wt%Ag-0.5wt%Cu and Sn-0.7wt%Cu in the temperature range 60~130℃ [160], while in drop testing it is

typically ~ 10^2 s^{-1} [161]). At least 14 joints were tested for each of the four microstructure conditions.

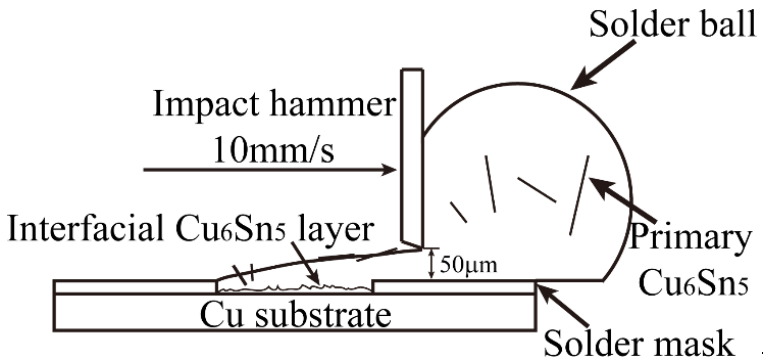


Fig. 74 Set up of shear impact testing on a DAGE4000.

The microstructures of both as-soldered joints and impact shear tested joints were studied. Cross-sections were prepared by mounting joints in Struers VersoCit resin, grinding with SiC papers and polishing with SiO_2 suspension. Some samples were deep etched in 5% NaOH and 3.5% orthonitrophenol in distilled H_2O to reveal the 3D morphology of the primary Cu_6Sn_5. Fracture surfaces were examined without sample preparation. Analytical scanning electron microscopy (SEM) was conducted in a Zeiss Auriga field emission gun (FEG) SEM equipped with a Bruker e-Flash electron backscatter diffraction (EBSD) detector and EBSD analysis was performed in Bruker Esprit 2.1. Cu_6Sn_5 was indexed and analysed as the high temperature hexagonal Cu_6Sn_5 polymorph [54, 162] since this phase is stable at the temperatures shown in Fig. 73(b) and (c).

5.3 Results and Discussion

5.3.1 Undeformed microstructures

Fig. 75 shows typical micrographs of the primary Cu_6Sn_5 in Sn-2wt%Cu/Cu joints produced from the four batches of solder balls containing Cu_6Sn_5 of different sizes. The first column are EBSD IPF-y maps of the Cu_6Sn_5 phase from typical cross-sections. It can be seen that the primary Cu_6Sn_5 have a wide range of orientations in each batch. The second column are BSE SEM images from the same cross-sections where the primary Cu_6Sn_5 appear dark grey. The number of Cu_6Sn_5 particles per unit area of cross-section was measured from EBSD maps of at least 4 samples per microstructure condition and the results are plotted in Fig. 76 (a). It can be seen that the joints with smallest primary Cu_6Sn_5 contain more than 4 times more primary Cu_6Sn_5 per unit area than the joints with largest primary Cu_6Sn_5. The number of Cu_6Sn_5 crystals were measured in Image J from BSE SEM images with information of the different Cu_6Sn_5 orientations from the EBSD maps. The third and fourth columns in

Fig. 75 are SE-SEM images after partial dissolution of the matrix βSn at two magnifications. It can be seen clearly that the mean size (e.g. width) of the faceted Cu_6Sn_5 rods increases from (a) to (d). Combining this with the decreasing number of Cu_6Sn_5 particles from (a) to (d) in

Fig. 75 and Fig. 76(a), it can be confirmed that the Cu_6Sn_5 rods are systematically larger and fewer (less numerous) from (a) to (d) in

Fig. 75, and with a similar volume fraction since they have the same composition.

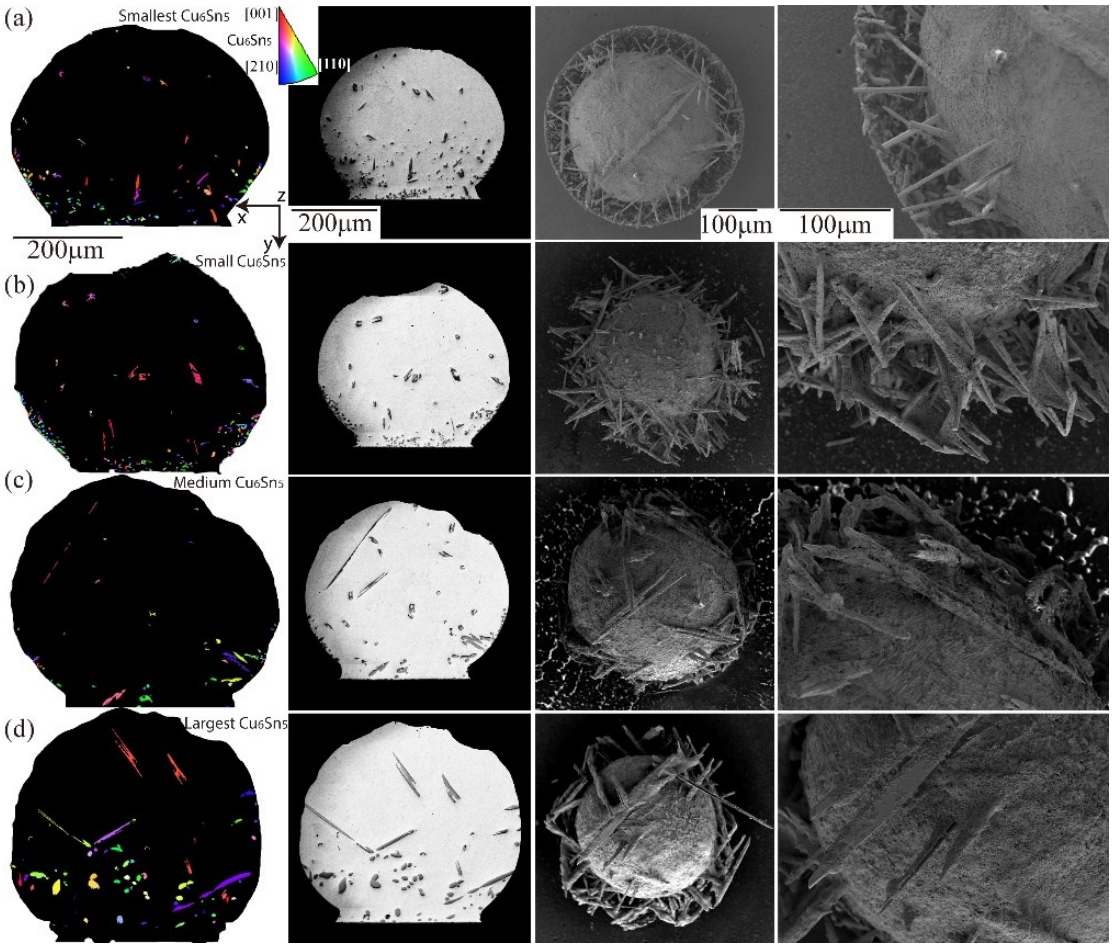


Fig. 75 Overview of primary Cu_6Sn_5 in Sn-2Cu/Cu joints made with four sizes of primary Cu_6Sn_5, with increasing size of primary Cu6Sn5 from (a) to (d). The first and second columns are EBSD IPF-y maps and BSE-SEM images. The third and fourth columns are deep etched SE-SEM images of the primary Cu_6Sn_5 at two magnifications. Each column has a common scale bar.

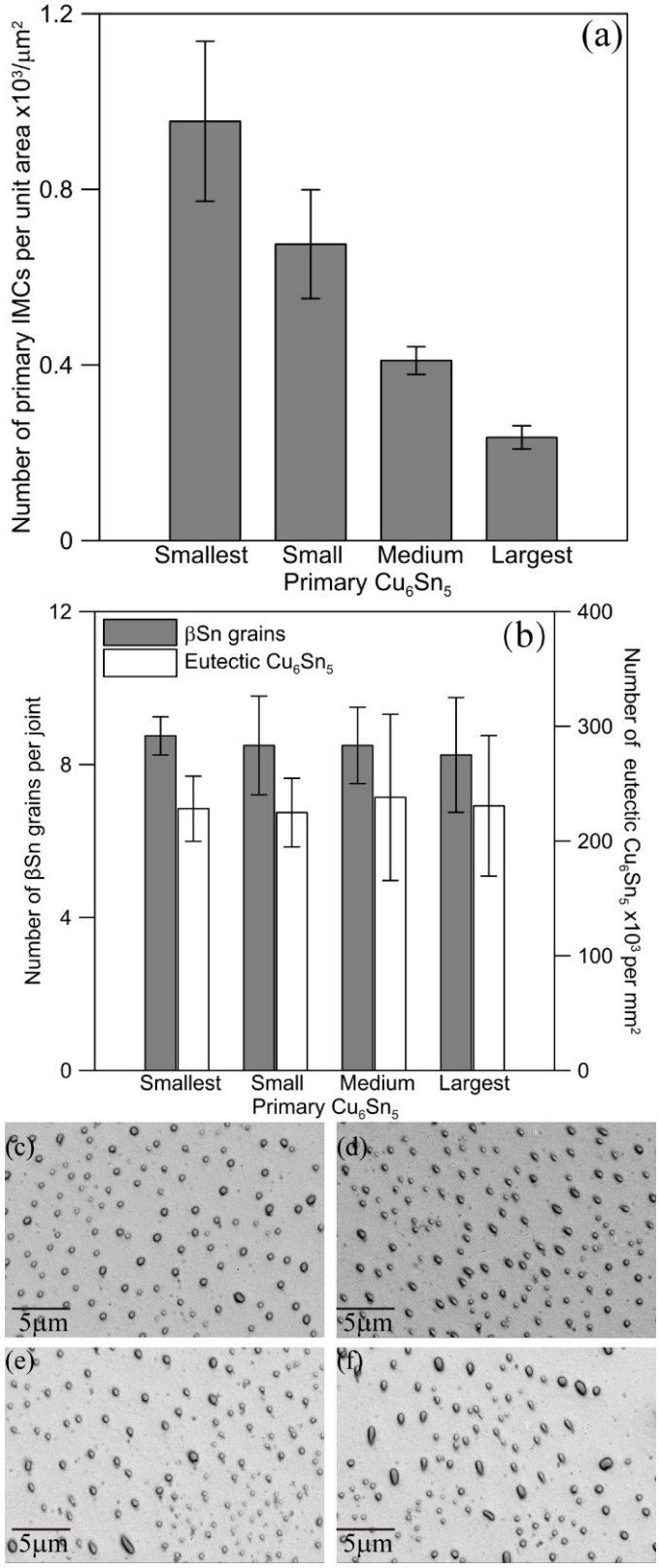


Fig. 76 Summary of microstructural measurements for each batch of Sn-2Cu/Cu joints. Bars are mean values, error bars are standard deviations. (a) Number of primary Cu6Sn5 per unit area. (b) Number of eutectic Cu6Sn5 particles per unit area, and number of βSn orientations per joint. (c)-(f) typical BS-SEM micrographs used to count eutectic Cu_6Sn_5 number in joints with increasing size of primary Cu_6Sn_5.

Fig. 77 summarises the βSn microstructure and growth texture in un-deformed solder joints from the four microstructure conditions, with increasing size of primary Cu_6Sn_5 from (a) to (d). The left column shows EBSD IPF-y maps of typical cross sections. It can be seen that, in all cases, there are multiple orientations (colours) indicating multiple βSn grains. The number of independent βSn grains was measured on EBSD IPF maps from 4 joints for each condition, where grains were considered to be independent if they were not related to other grains by twins, other special boundaries or low angle boundaries [163]. The data are plotted in Fig. 76(b) where the error bars are the standard deviations from the at least 4 samples for each condition. It can be seen that the number of independent βSn grains was similar at 7.7 ± 0.2 for each microstructure condition.

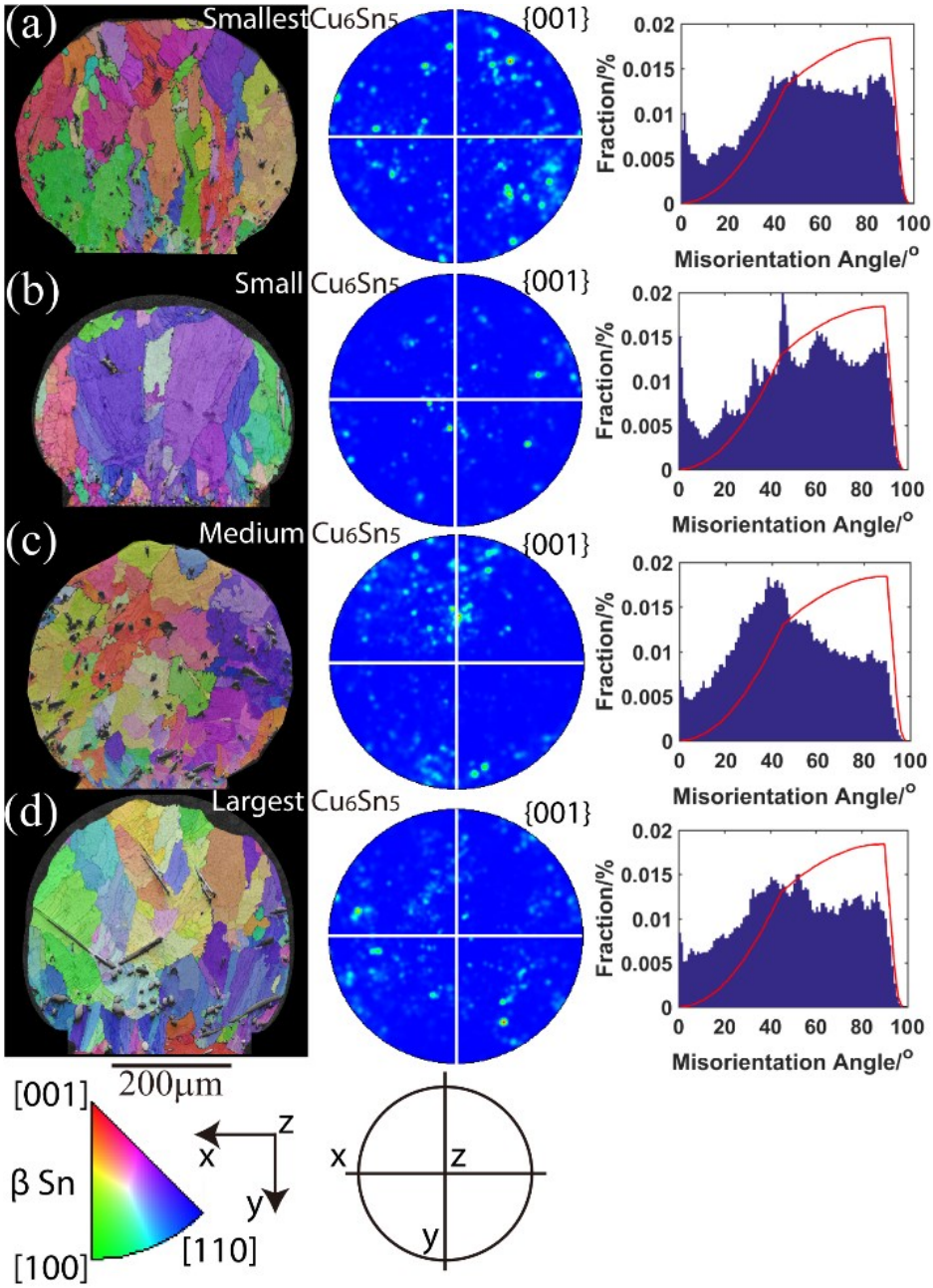


Fig. 77 Overview of βSn in Sn-2Cu/Cu joints, with increasing size of primary Cu6Sn5 from (a) to (d). The first column are EBSD IPF-y maps of typical joints. The middle column are {001} pole figures made by combining ≥4 EBSD maps for each microstructure condition. The third column are misorientation (MO) histograms, compiled from ≥4 joints for each microstructure condition. Mackenzie curves are superimposed on the MO distributions

In Fig. 77, the middle column shows <001> pole figures for βSn grains in all joints for each condition. These pole figures were made by combining all EBSD datasets

(at least 4) for each microstructure condition, ensuring that the y-direction was perpendicular to the substrate in all cases. Note that, since βSn is tetragonal, it has only one <001> direction in the northern hemisphere and, therefore, each βSn grain contributes one point to the combined <001> pole figure. While the relatively small number of grains from 4-7 samples with ~8 grains per sample precludes a meaningful study of the statistics, it can be seen that in all microstructure conditions, the grains have their c-axis oriented in a wide range directions and there is no clear texture.

The right column in Fig. 77 shows misorientation (MO) histograms which have been compiled from all datasets for each microstructure condition. This was done by summing the bins from each dataset so as to consider only misorientations within each joint and not consider misorientations between grains in different joints. Each plot also contains a Mackenzie curve which is the expected random misorientation distribution for tetragonal crystals. Each plot has the same following features: there is a peak at <10° corresponding to low angle boundaries, there are more misorientations with 10-50° than in a random distribution, and there are fewer misorientations with 50-100° than in a random distribution. It can be seen also that there are peaks in some of the MO plots, such as the 42-48° peak in Fig. 77(b); these occur because some joints had two large grains in a cross-section which gives a large MO peak in one sample. It is expected that these would not be present in the summed distributions if many more joints were added into these combined MO distributions.

By combining the number of independent grains in Fig. 76(b) with the textures and misorientation distributions in Fig. 77, it can be concluded that the number of βSn

grains and the βSn growth texture is similar for all microstructure conditions. This confirms the success of the method developed to generate different primary Cu_6Sn_5 sizes while keeping the βSn microstructure near-constant. Additionally, the number of eutectic Cu_6Sn_5 particles per unit area was measured on at least 4 BSE-SEM images (Fig. 76(c)-(f)) for each condition and the results are plotted on Fig. 76(b), where it can be seen that the number density of eutectic Cu_6Sn_5 particles is similar at each microstructure condition.

Note that the βSn texture in these Sn-2Cu/Cu joints (Fig. 77) is markedly different to that in SnAg/Cu or SnAgCu/Cu BGA joints where there are usually only 1-3 βSn orientations that are all related by solidification twinning [68, 164-167] (i.e. only one independent grain). It is also different to the texture of Sn-0.7Cu/Cu BGA joints which usually solidify with multiple columnar grains growing from the substrate[92] which leads to a strong <110> fibre texture in the y-direction [92, 168]. Examining the EBSD map in Fig. 77(d), it can be seen that there are some columnar βSn grains emanating from the substrate and that these have been blocked by near-equiaxed grains above. This suggests that βSn nucleation events have occurred ahead at the columnar front. This might indicate that the higher volume fraction of primary Cu_6Sn_5 has promoted βSn nucleation in the bulk solder in Sn-2Cu/Cu. Further work is required to prove the mechanism and explore whether this phenomenon can be used to usefully generate more βSn orientations in joints.

The typical morphologies of interfacial Cu_6Sn_5 prior to shear impact testing are shown in Fig. 78.

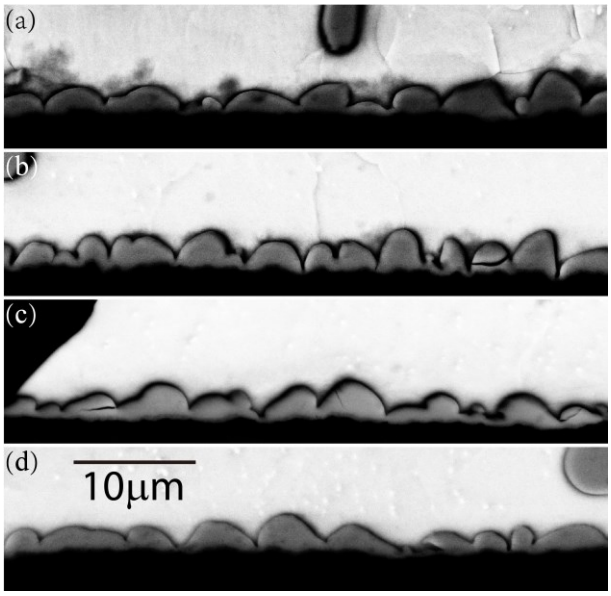


Fig. 78 Interfacial Cu_6Sn_5 in solder joints with increasing primary Cu_6Sn_5 size from (a)-(d) prior shear impact test

The mean thickness of interfacial Cu_6Sn_5 has been measured from at least 4 micrographs and were 1.37±0.16, 1.32±0.05, 1.38±0.15 and 1.40±0.11 μm for the joints containing increasing size of primary Cu_6Sn_5 and it can be seen that the interfacial layers in all the joints have similar morphology and very near mean thickness.

5.3.2 Impact shear properties

Typical examples of force-displacement curves from each microstructure condition are shown in Fig. 79. The examples shown are the median curve from the ≥14 force-displacement curves obtained for each microstructure condition. It can be seen that the impact shear curves have two peaks. One initial small peak at a displacement of ~60μm, followed by a serrated increase in force up to the main peak. The shape of the curve is similar to past work at this displacement rate [122, 169].

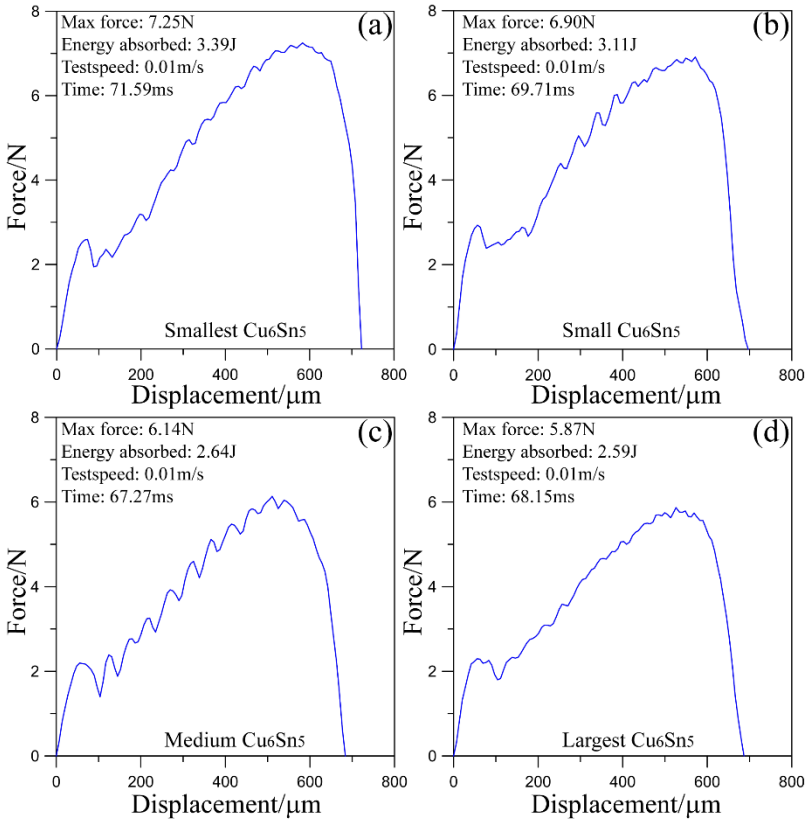


Fig. 79 Typical force-displacement curves from shear impact testing, with increasing size of primary Cu6Sn5 from (a) to (d).

Fig. 80 summarises the impact shear properties for joints with the four sizes of primary Cu6Sn5. It can be seen that both the maximum force and the energy absorbed decrease with increasing primary Cu6Sn5 size. The error bars represent the standard

deviations from at least 14 samples for each condition. Note that the error bars for the smallest and small Cu_6Sn_5 joints do not overlap with the largest Cu_6Sn_5 joints, which highlights the significance of the result. From

Fig. 75-Fig. 80, it can be seen that, for equivalent βSn, interfacial Cu_6Sn_5 layer and eutectic microstructures and primary Cu_6Sn_5 volume fraction, increasing the size of primary Cu_6Sn_5 decreased the maximum force by 28% and decreased the energy absorbed by 39%. That is to say, when other microstructural variables are held near-constant, there is a clear negative effect of larger primary Cu_6Sn_5 particles on the shear impact properties of Sn-Cu/Cu BGA joints.

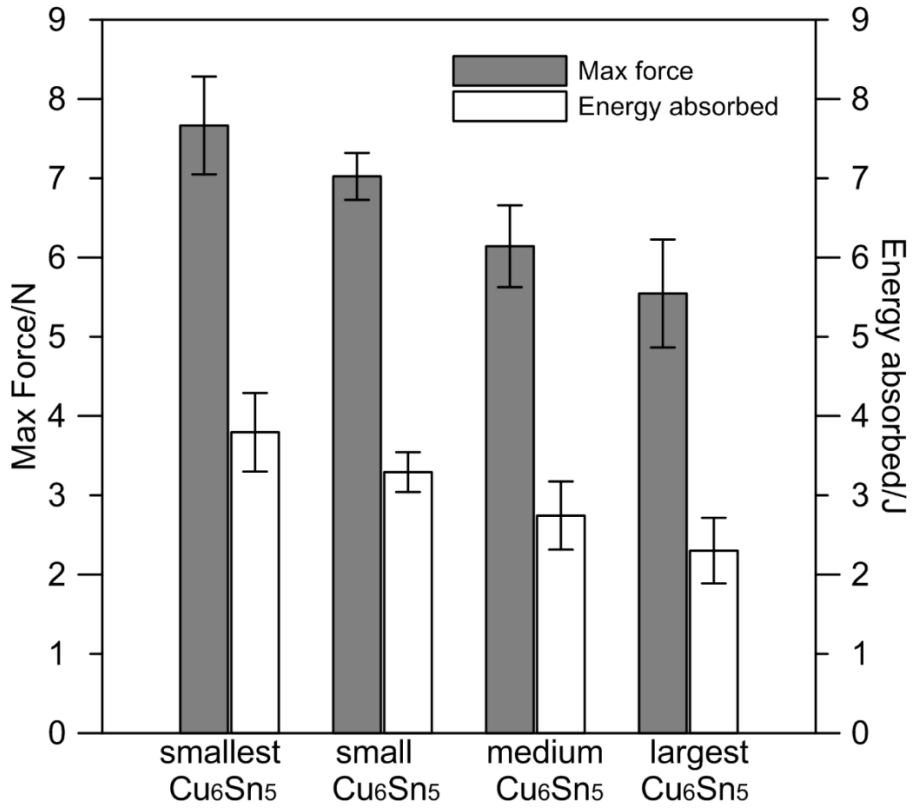


Fig. 80 Impact shear properties (maximum force and energy absorbed) of Sn-2wt%Cu/Cu with different size of primary Cu_6Sn_5.

The width of primary Cu_6Sn_5 rods was measured on SE-SEM images of the fracture

surfaces and a statistical overview of the measurements is given in Fig. 81 (a) and (b). In Fig. 81 (a), it can be seen that the standard deviation of the primary Cu_6Sn_5 width increased as the mean Cu_6Sn_5 width increased. This is thought to be because, during cooling at the end of reflow soldering, new primary Cu_6Sn_5 nucleate and grow in addition to the growth of incompletely melted primary Cu_6Sn_5, which gives a large range of primary Cu_6Sn_5 sizes in samples where the incompletely melted primary Cu_6Sn_5 are large. Fig. 81 (b) presents box plots of the Cu_6Sn_5 width data; it can be seen that the lowest width, 25th percentile, 50th percentile, 75th percentile and highest width all increase as the mean Cu_6Sn_5 width increases.

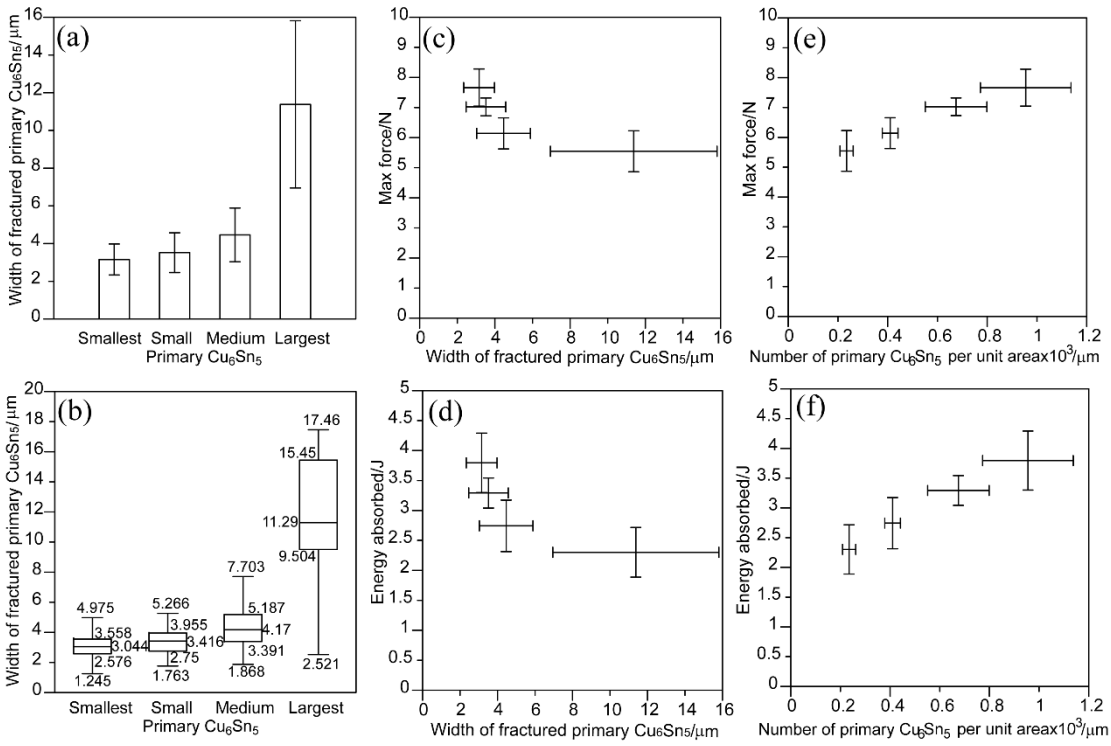


Fig. 81 (a) Width of fractured primary Cu_6Sn_5 on fracture surfaces for each microstructure condition. Bars are mean values, error bars are standard deviations. (b) The same data summarised in box plots. (c) Maximum force versus the width of fractured primary Cu_6Sn_5. (d) Energy absorbed versus the width of fractured primary Cu_6Sn_5. (e) Maximum force versus the number density of primary Cu_6Sn_5. (f) Energy absorbed versus the number density of primary Cu_6Sn_5.

Fig. 80 and Fig. 81 (a) have been combined into Fig. 81 (c) and (d) which shows the change in impact shear properties versus primary Cu_6Sn_5 width. There is a significant decrease in shear impact properties with increasing width of the primary Cu_6Sn_5. Fig. 81(e) and (f) show that the shear impact properties versus the number of primary IMCs within the joints (from Fig. 76(a)) for the four conditions. With increasing number of primary IMCs, both the maximum force and energy absorbed increase significantly.

Note that this result is specific to shear impact conditions where fracture is through the bulk solder and that different results might be expected at higher rate (e.g. 2000mm/s) where fracture typically involves the Cu_6Sn_5 layer.

5.3.3 Deformed microstructures

Typical cross sectioned micrographs of fractured solder joints are given in Fig. 82 . It can be seen that the fracture path for all joints was through the bulk solder, and that macroscopic fracture was by a combination of ductile fracture of the soft βSn matrix and brittle fracture of the hard embedded Cu_6Sn_5 rods. Thus, the Cu_6Sn_5 IMC layers did not strongly influence the fracture of the joints in this work.

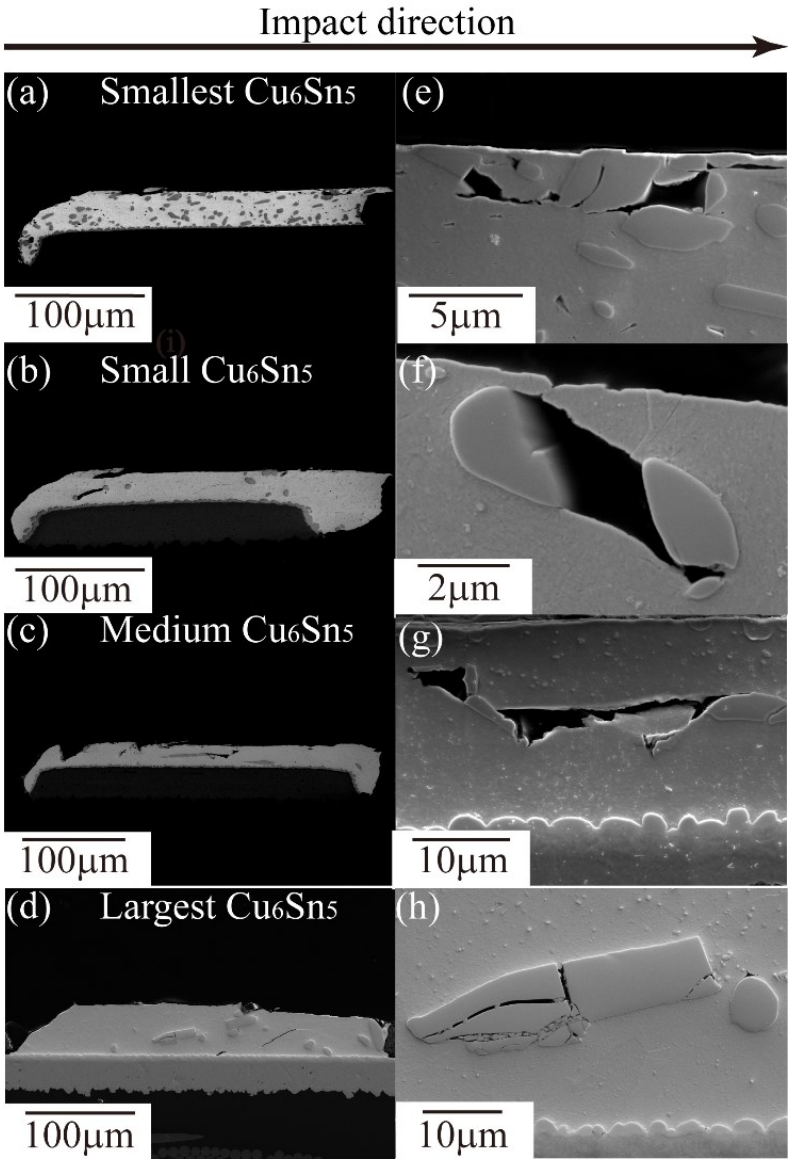


Fig. 82 Cross sections of fractured joints, with increasing size of primary Cu6Sn5 from top to bottom. (a)-(d) typical examples of the whole cross-section. (e)-(h): higher magnification images of primary Cu_6Sn_5 on and beneath the fracture surfaces.

To gain some insights into the initiation of fracture, interrupted impact tests were performed where the hammer was stopped at a certain displacement so that the microstructure could be studied and the events that occur early during impact testing could be deduced. Caution is required when interpreting interrupted tests as it was not possible to instantaneously halt the hammer motion and there may have been some βSn microstructure evolution between the time of impact and the time of EBSD measurements due to the high dislocation accumulation coupled with the high homologous temperature of ~0.6T_m at room temperature. Nevertheless, interrupted impact experiments provide useful information. Fig. 83 shows the typical results for an example where the hammer displacement was ~150 μm (~30% of the displacement of fully fractured joints) and where the impact direction was from left to right. Fig. 83(a) is a BSE-SEM image of a cross-section and Fig. 83(b) is an EBSD IPF-y map of βSn from the same area. In (b) it can be seen that βSn deformation is localized ahead of the hammer where the grains contain gradual changes in colour revealing a gradient of in-grain misorientation created by plasticity. Fig. 83(c)-(e) show typical regions where Cu_6Sn_5 particles have influenced the initiation and propagation of microcracks. In Fig. 83(c), decohesion has occurred between a Cu_6Sn_5 rod and the βSn matrix and propagated as a crack into the βSn matrix. In Fig. 83(d), brittle fracture of a Cu_6Sn_5 rod followed by the opening displacement of this crack has created a void in the ductile βSn matrix. In Fig. 83(e), a similar crack is beginning to propagate from a cracked Cu_6Sn_5 rod into the βSn matrix. Thus, it can be seen that brittle fracture of primary Cu_6Sn_5 crystals and decohesion between primary Cu_6Sn_5 and the βSn matrix both

introduce internal microcracks early during shear impact.

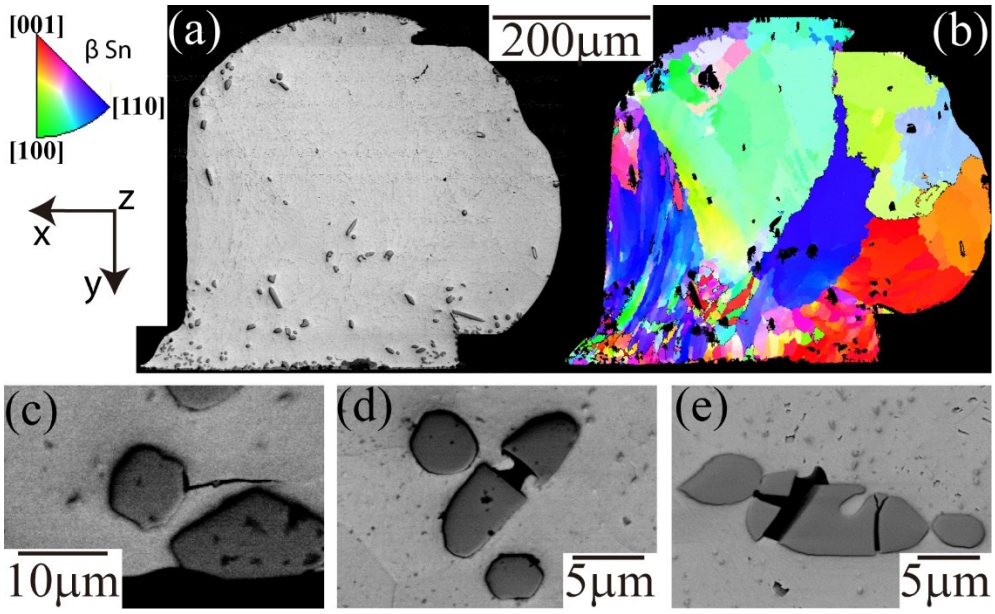


Fig. 83 Shear impact test interrupted at ~150μm. (a) BSE-SEM image of a cross-section. (b) EBSD IPF-y map of the same cross-section. (c)-(e) examples of decohesion between Cu_6Sn_5 and the βSn matrix, brittle fracture of primary Cu_6Sn_5, and the propagation of microcracks into the βSn.

Similar phenomena were observed after complete fracture. In Fig. 82 (e)-(h), it can be deduced that brittle fracture of primary Cu_6Sn_5 crystals created microcracks which opened (e.g. Fig. 82 (f)) and propagated in the βSn matrix. This is one factor behind the deterioration of impact properties with increasing primary Cu_6Sn_5 size: The brittle fracture of larger primary Cu_6Sn_5 rods creates a larger microcrack and, therefore, the energy needed to open it and extend into the Sn matrix is smaller. Another factor is that βSn plastic flow around larger Cu_6Sn_5 will open larger voids around the Cu_6Sn_5 which promotes βSn ductile tearing.

Fig. 84(a)-(d) presents typical fracture surfaces from the four microstructure conditions. For all joints, the fracture surface is rough with the characteristics of ductile tearing of βSn. Comparing Fig. 84 (a)-(d), it can be seen that the surfaces have increasingly complex roughness from (a) to (d), corresponding to the larger and fewer primary Cu_6Sn_5 from (a) to (d) as shown in the higher magnification images in Fig. 84 (e)- (h). It was found that each fracture surface has two regions with differently fractured primary Cu_6Sn_5. The region first touching the hammer is shown in Fig. 84 (i). In this region, primary Cu_6Sn_5 are more vertical and brittle fracture surfaces of numerous Cu_6Sn_5 grains can be seen, indicating that the embedded primary Cu_6Sn_5 near the impact location underwent cleavage fracture. There is also evidence of decohesion between the Cu_6Sn_5 and βSn in some regions of Fig. 84 (i). As the hammer moves on, the fractured BGA surfaces become rougher and fragments of fractured primary Cu_6Sn_5 rods are forced to be near parallel to the hammer direction and plastically gouge trenches along the βSn fracture surface (Fig. 84 (j)). Therefore, the plastic deformation of the βSn by gouging Cu_6Sn_5 fragments contributes to the plastic work of ductile fracture in these joints. Comparing rougher parts of solder joints made with each microstructure condition, it was found that the fragments in the smaller primary Cu_6Sn_5 microstructure conditions (e.g. smallest and small in Fig. 76a) tended to align better with the hammer direction (Fig. 84 (k)) and appeared to gouge the βSn fractured surface more. This extra interaction between Cu_6Sn_5 fragments and the βSn may be a further reason for the higher energy absorbed in samples with smaller primary Cu_6Sn_5.

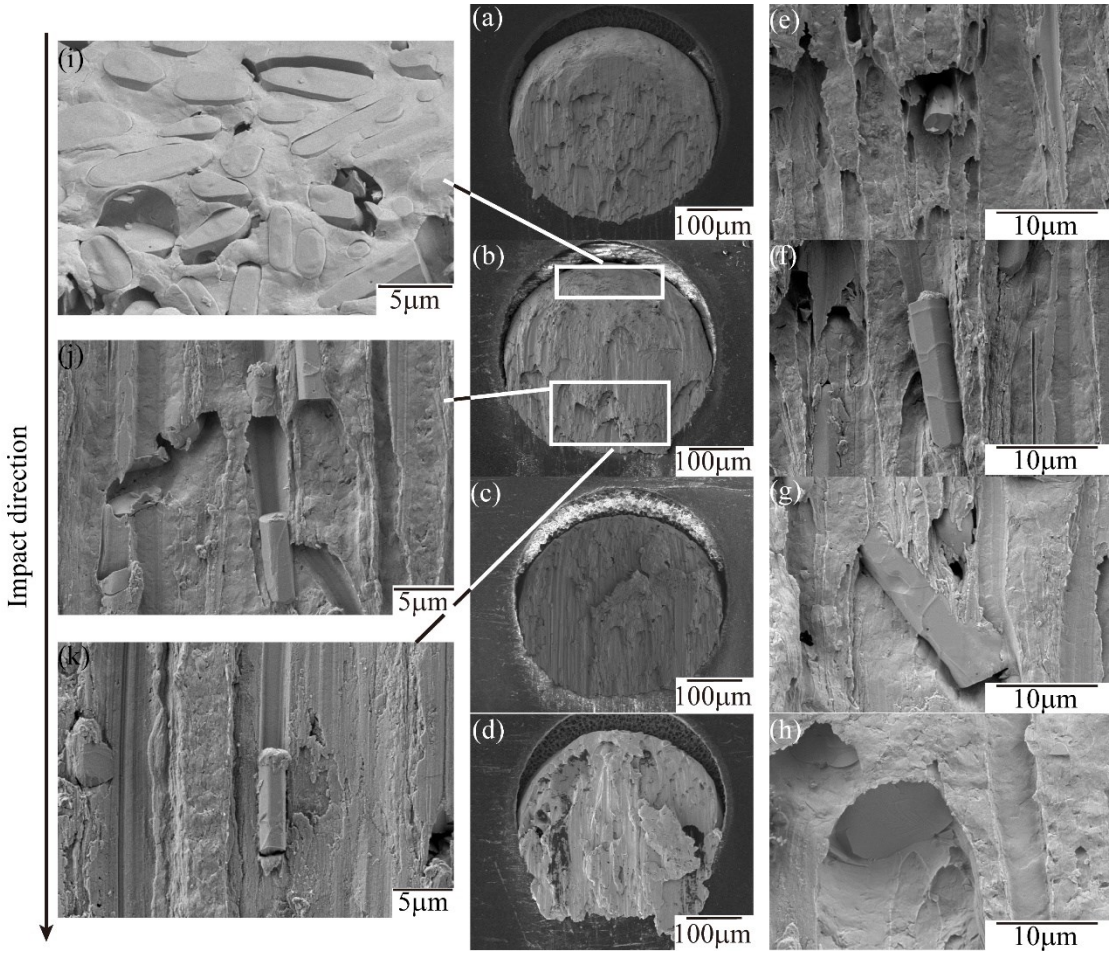


Fig. 84 Fracture surfaces of solder joints from batches with increasing size of primary Cu6Sn5 from (a) to (d). Typical examples of the varying Cu_6Sn_5 size are given in (e)-(h). (i)-(k) show typical features found at different locations of the fracture surfaces: (i) brittle fractured primary Cu_6Sn_5 at the 'front part' of the surface near to the initial hammer impact, (j)-(k) primary Cu_6Sn_5 fragments at the 'bottom part' of the surface.

The fracture surfaces of individual primary Cu_6Sn_5 crystals were explored to gain further insights in to the failure mechanisms. Primary Cu_6Sn_5 fracture surfaces which were relatively parallel to the macroscopic fracture surface were chosen for EBSD analysis.

Fig. 85(a) and (b) are SE-SEM images of typical fractured Cu_6Sn_5 rods from joints containing 'medium' size primary Cu_6Sn_5 and Fig. 85(c) is a combined EBSD IPF-z map of 11 fractured Cu_6Sn_5 where the fracture surface is near-perpendicular with the z-

direction in all cases (i.e. the normal to the fracture surfaces is approximately in the z-direction). Note that the 11 fractured Cu_6Sn_5 come from different samples and have been compiled into a single IPF-z map. The colours correspond to the hexagonal colour legend in Fig. 85(d). It can be seen that 10 out of 11 fracture surfaces have a green/blue colour and one has a red colour which corresponds to cleavage approximately along prism planes and the basal plane respectively. This result is plotted as an inverse pole figure with respect to the z-direction in Fig. 85(e). The scatter in the data is largely because the Cu_6Sn_5 fracture surfaces are not co-planar with the macroscopic fracture surface. Although only one basal fracture is shown in Fig. 85 (c) (the red grain), this cleavage plane was widespread in the samples. For example, inspection of the Cu_6Sn_5 rod fragments in Fig. 84(e)-(h) and (j)-(k) shows that most fragments in these images fractured along their basal plane (noting that Cu_6Sn_5 hexagonal rods are bounded by {10-10} facets with [0001] along the rod [8, 11, 152]). Examples of prism fracture surfaces are shown in Fig. 85(a) and (b).

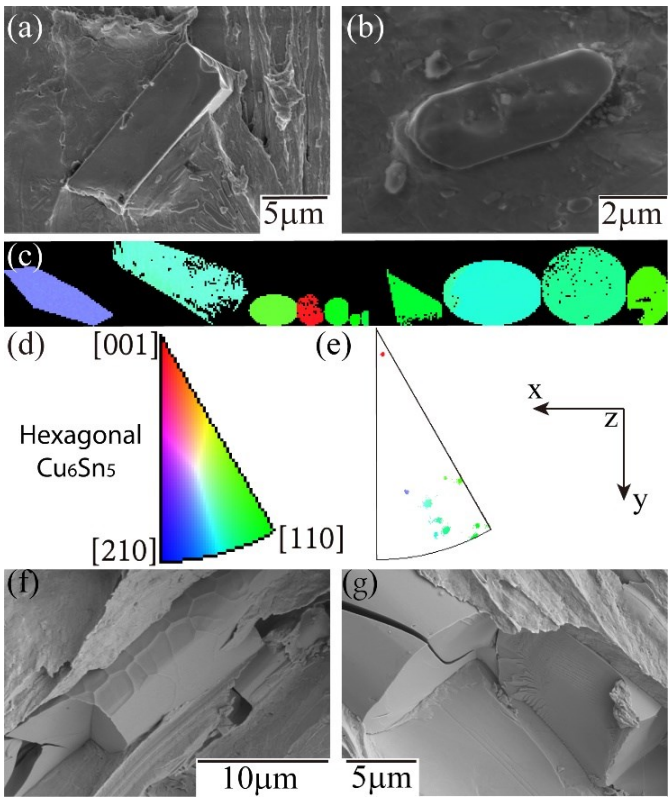


Fig. 85 (a)-(b) Typical Cu_6Sn_5 brittle fracture surfaces that are close to the plane of the macroscopic fracture surface. (c) EBSD IPF-z map of 11 Cu_6Sn_5 fracture surfaces from different samples compiled into a single map. (d) hexagonal IPF colour scale. (e) IPF-z for the 11 Cu_6Sn_5 crystals in (c). (f) and (g) examples of crack deflection from basal to prism fracture paths.

As illustrated in reference [11], the {11-20} and {1-100} (the 2nd and 1st order prism planes) are the closest-packed flat planes in hexagonal Cu_6Sn_5, and the basal plane is the next closest packed, which agrees with the theory that the closest packed planes are the preferred cleavage planes. The large number of basal fractures may also be due to the shape of the long Cu_6Sn_5 rods (i.e. bending of a prismatic rod will favour basal fracture).

In some cases, it was found that the fracture path deflected as it propagated through

a Cu_6Sn_5 crystal; either from a basal fracture to a prism fracture, from a prism fracture to a basal fracture or, sometimes, from one to the other and then back to the original fracture plane. For example, in Fig. 85 (f) and (g), the crystal orientation can be determined from the {1-100} growth facets and [0001] growth direction of the Cu_6Sn_5 rods and deflection from basal to prism fracture can be inferred. This shows more than one cleavage plane is active in Cu_6Sn_5 fracture, which agrees with [56, 143]. Crack deflections are likely to be due to the combined effects of the crystallography of Cu_6Sn_5 (e.g. close-packedness of planes) and the orientation of the crystal relative to the hammer impact direction.

5.4 Conclusions

The influence of primary Cu_6Sn_5 size on shear impact properties has been investigated in 500μm BGA-type Sn-Cu/Cu joints. An effective method for manipulating the primary Cu_6Sn_5 size while keeping the remaining microstructure near-constant has been applied in which a high Cu content is used (2wt% Cu), the primary Cu_6Sn_5 size is manipulated in the initial freestanding solder balls (either by quenching during solder ball manufacture or by aging balls after manufacture), and this primary Cu_6Sn_5 size is largely maintained in solder joints because the peak reflow temperature (250 °C) is less than the Cu_6Sn_5 liquidus temperature so that the primary Cu_6Sn_5 only partially remelt. This method was used to vary the Cu_6Sn_5 rod width from 3 - 12 μm and vary the number of primary Cu_6Sn_5 crystals per unit area of cross-section by a factor of 4. BGA shear tests were performed on a DAGE-4000 bond-tester with 10mm/s hammer speed to ensure that fracture occurred through the bulk solder.

It has been found that the shear impact properties (maximum force and energy absorbed) decrease as the size of the primary Cu_6Sn_5 increases. That is to say, when other microstructural variables are held near-constant, there is a clear negative effect of larger primary Cu_6Sn_5 particles on the shear impact properties of Sn-Cu/Cu BGA joints.

Microstructure analysis revealed that brittle fracture of primary Cu_6Sn_5 and decohesion between primary Cu_6Sn_5 and the βSn matrix both introduce microcracks early during shear impact. These microcracks then propagated into the soft βSn matrix by ductile tearing. The embedded primary Cu_6Sn_5 cleaved along (0001) and perpendicular to (0001), and Cu_6Sn_5 fragments then reoriented parallel with the

hammer direction and continued to influence ductile fracture by gouging trenches into the βSn surface.

The deterioration of shear impact properties as the primary Cu_6Sn_5 rod size increases is attributed to (i) the larger microcracks introduced by cleavage of larger Cu_6Sn_5 rods and (ii) the smaller number and wider spaced Cu_6Sn_5 rods when the rods are larger.

Chapter 6 Conclusions and Future Work

6.1 Conclusions

This thesis has built a deeper understanding of the factors affecting primary Cu_6Sn_5 morphology evolution in solder joints, using the binary system of Sn-x wt% Cu (x=0-2) on Cu substrates as an example, and of the influence of primary Cu_6Sn_5 on the shear impact properties of BGA-type solder joints.

For the Cu_6Sn_5 morphology, the majority of prior research focussed on the interfacial Cu_6Sn_5 [8, 86, 89, 111, 170, 171] The smaller portion on primary Cu_6Sn_5 observed and reported hollow type [9, 49, 50], grooved type [8], needle type [28, 49], X-like [9, 67], Y-like [13, 67], and dendritic Cu_6Sn_5 [125, 153], the formation of which were due to several factors e.g. Cu content, trace elements etc. This thesis has systematically investigated the influence of soldering process parameters i.e. peak soldering temperature, holding time at peak temperature and cooling rate on the volume fraction and morphology transition of primary Cu_6Sn_5 in Sn-0.7wt%Cu/Cu joints. It has been found that with longer holding time and higher peak soldering temperature, more Cu diffused from the Cu substrate which increased the mean Cu content in the bulk solder, which could be understood using the Nernst-Brunner equation. With increasing Cu dissolution, the volume fraction of Cu_6Sn_5 increased and the primary Cu_6Sn_5 morphologies transformed from faceted rods to non-faceted dendrites due to interface roughening which was also observed with faster cooling rate. Meanwhile, with the increasing of holding time at 300°C, the primary interfacial Cu_6Sn_5 layer thickness increased near linearly with the square root of holding time, indicating the growth of

the layer is controlled by volume diffusion through the layer. It has been observed that large primary Cu_6Sn_5 could grow from pre-existing Cu_6Sn_5 crystals in the interfacial layer and grow to fill the whole joint. This larger primary Cu_6Sn_5 contained the morphology transition from faceted to non-faceted with increased growth distance at longer holding time and higher peak temperature. This can be understood as the growth into a negative temperature gradient. The relationship between Cu dissolution from the Cu substrate and that gained due to both the interfacial layer and primary Cu_6Sn_5 growth during changing these two factors has been quantitatively studied. A simple equation was built bridging the Cu loss from the substrate and that gained by IMCs in Chapter 3:

$$m_{Cu} = 0.36L_{Cu_6Sn_5}^{layer}A_{pad}\rho_{Cu} + 0.78L_{Cu_3Sn}^{layer}A_{pad}\rho_{Cu} + 0.36V_{solder}g_{Cu6Sn5}^{primary}\rho_{Cu}$$

The combination of this equation and measurements of IMC layer thicknesses and the fraction of primary Cu_6Sn_5 has been used to show that Cu substrate dissolution is mainly due to the growth of interfacial layer at low peak temperature and after the liquid solder is saturated with Cu whereas, at higher peak temperatures, Cu substrate dissolution is mainly due to saturating the liquid in Cu.

A primary Cu_6Sn_5 morphology map of cooling rate versus Cu content and peak reflow temperature has been built which can be useful in choosing process parameter combinations to grow primary Cu_6Sn_5 with desired morphology in solder joints.

Synchrotron radiography has been used to observe primary Cu_6Sn_5 formation in solder joint of Sn-x wt% Cu (x= 0, 0.7, 2) on Cu with a common industrial peak reflow

temperature. It has been found that no primary Cu_6Sn_5 solidified in CP-Sn/Cu joints even though Cu dissolution happened during soldering which can be understood from Nernst-Brunner effect: the low area to volume ratio requires a longer time for Cu dissolution into bulk solder than occurs in BGA-type geometries. For Sn-0.7wt%Cu which is also a hypoeutectic composition, primary Cu_6Sn_5 formation was observed during cooling from the peak temperature. due to the dissolution Cu increasing the Cu content in the bulk solder into the hypereutectic region. Primary Cu_6Sn_5 either nucleated in the bulk solder or grow from the pre-existing crystals on the interfacial layer. Two types of Sn-2wt%Cu were investigated: containing small or large pre-existing primary Cu_6Sn_5 in the initial preform. The peak soldering temperature used was lower than its liquidus temperature (~287℃), therefore the pre-existed primary Cu_6Sn_5 did not fully remelt. It has been found that during soldering the small pre-existing primary Cu_6Sn_5 would settle down to the interfacial layer under gravity, while the large ones did not. The mean primary Cu_6Sn_5 size in the joint with small pre-existing primary Cu_6Sn_5 was substantially smaller, indicating that by altering the combination of solder composition and the peak soldering temperature, the mean primary Cu_6Sn_5 size can be manipulated.

While a large body of research has considered how the interfacial Cu_6Sn_5 reaction layer [36-48] affects the performance of solder joints, this work explored the role of primary Cu_6Sn_5 on the shear impact properties of 500μm BGA-type Sn-2wt%Cu/Cu joints. The method of manipulating the primary Cu_6Sn_5 size while keeping the

remaining microstructure near constant was used to alter the Cu_6Sn_5 rod width from 3 - 12 μm. For the remaining microstructure: the Sn grain structures were examined by EBSD and the eutectic Cu_6Sn_5 were measured from backscattered electron micrographs. It has been found that number of independent Sn grains and eutectic Cu_6Sn_5 is similar in the joints containing different size of primary Cu_6Sn_5, however the Sn grain structure is more complex than that in joints with lower Cu content.

BGA shear impact testing was performed on a DAGE-4000 bond-tester with 10mm/s hammer speed to ensure that fracture occurred through the bulk solder. It has been found that larger primary Cu_6Sn_5 have a negative effect on the shear impact properties (maximum force and energy absorbed). Microstructure analysis revealed that microcracks were introduced at the early stage during shear impact by the primary Cu_6Sn_5 fracture and decohesion between primary Cu_6Sn_5 and βSn matrix. These microcracks then propagated into the soft βSn matrix by ductile tearing. The EBSD results revealed that the embedded primary Cu_6Sn_5 cleaved along (0001) and perpendicular to (0001), then Cu_6Sn_5 fragments reoriented parallel with the hammer direction and continued to influence ductile fracture by gouging trenches into the βSn surface. The larger primary Cu_6Sn_5 deteriorated the shear impact properties due to (i) the larger microcracks introduced by cleavage of larger Cu_6Sn_5 rods and (ii) the smaller and wider spaced Cu_6Sn_5 rods when they are larger.

To optimize reliability, previous work has identified that it is beneficial to suppress the thickness of the Cu_6Sn_5 layer and this thesis has shown that it is also desirable to minimize the volume fraction and size of primary Cu_6Sn_5. The thickness of the

interfacial Cu_6Sn_5 layer can be minimized by minimizing the peak reflow temperature and the time above liquidus. At the same time the volume fraction of primary Cu_6Sn_5 can be minimized by minimizing the peak reflow temperature. The size of primary Cu_6Sn_5 can be controlled by changing the cooling rate and minimizing the volume fraction of primary Cu_6Sn_5. However, the cooling rate cannot be significantly changed in industrial soldering and the primary Cu_6Sn_5 rods can be large even at low peak reflow temperature. The technique developed in this work of choosing the combination of solder composition and the peak reflow temperature where the primary Cu_6Sn_5 will not fully remelt during soldering requires high Cu content in the solder alloy which will result in a high volume fraction of primary Cu_6Sn_5 which is not desirable. An alternative way would be to microalloy the solder with Ni which greatly steepens the Cu_6Sn_5 liquidus and makes it possible to both retain unmelted Cu_6Sn_5 at the peak temperature while only having a small volume fraction of primary Cu_6Sn_5. Thus, to control the lengthscale of interfacial and primary Cu_6Sn_5, it is recommended to use a solder alloy containing ~0.05wt%Ni and a reflow profile that minimizes the peak reflow temperature and the time above liquidus.

6.2 Further Research

This thesis has explored primary Cu_6Sn_5 morphology development due to various soldering process parameters, observed based on both *post mortem* analysis of fully solid samples and on *in situ* real time synchrotron radiography, and the influence of changing in primary Cu_6Sn_5 size on the impact shear properties. Various questions have arisen during the research that would be interesting to explore in the future.

1. Controlling nucleation and growth of primary Cu_6Sn_5

During this work, only a binary solder system (Sn-Cu/Cu) has been used. Future work should explore how alloying additions can be used to control the nucleation and growth and manipulate the morphology of primary Cu_6Sn_5, building from past research such as [9, 12, 13, 91].

2. Distinguishing IMC formation during holding and during solidification

The interfacial IMC layer measured in this work was a combined result of the IMC layer formed during isothermal holding and that formed during cooling. Although the solidification duration is very short when the cooling rate is fast, the interfacial velocity for IMCs growth can be very large, so the IMC layer could grow to a considerable amount during solidification. Therefore, it is very interesting to use synchrotron radiography or tomography at higher resolution to quantify the component of IMC layer thickness that formed during holding and that formed during cooling.

3. Identifying the cleavage planes in primary Cu_6Sn_5

In this work, it has been found that the fracture path in primary Cu_6Sn_5 could deflect either from basal to prism plane or from prism to basal plane or from one to another then come back and the fracture path could be a curve (Fig. 86). Detailed in-situ SEM or TEM studies on the mechanisms of Cu_6Sn_5 single crystal fracture are needed to expand upon the EBSD study performed here on cleavage planes in primary Cu_6Sn_5, and the changing plane during cleavage.

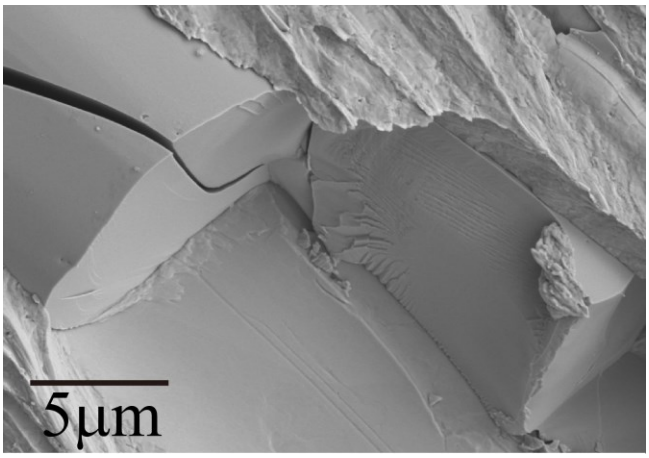


Fig. 86 deflected fracture path in primary Cu_6Sn_5 in Sn-2wt%Cu during shear impact testing

4. Deeper exploration of the mechanical properties of solder joints

The only property that has been tested in this work is the resistance to shear impact testing at one shear rate. Further work should explore a range of shear rates and then expand to consider other loading modes relevant to solder joints e.g. drop testing, thermal cycling etc.

References

1. Y. Li, K.-s. Moon, and C.P. Wong, Electronics Without Lead. Science, (2005). 308: 1419-1420.

2. EUParliament, Directive 2002/95/EC on the restriction of the use of certain hazardous substances in electrical and electronic equipment. 2003, Official J. Eur. Union. 19-23.

3. X. Lao, C. Cheng, X. Min, J. Zhao, D. Zhou, and X. Li, Leaching behaviour and environmental risk assessment of heavy metals from electronic solder in acidified soil. Environmental Science and Pollution Research, (2015). 22: 17683-17690.

4. C.G. Yedjou, H.M. Tchounwou, and P.B. Tchounwou, DNA Damage, Cell Cycle Arrest, and Apoptosis Induction Caused by Lead in Human Leukemia Cells. International Journal of Environmental Research and Public Health, (2016). 13: 56.

5. https://www.ephotozine.com/article/apple-iphone-4-camera--review-15526. [cited 2017 12.15].

6. https://jp.ifixit.com/Teardown/Apple+A4+Teardown/2204. [cited 2017 12.15].

7. C.E. Ho, S.C. Yang, and C.R. Kao, Interfacial reaction issues for lead-free electronic solders. Journal of Materials Science-Materials in Electronics, (2007). 18: 155-174.

8. Y. Tian, R. Zhang, C. Hang, L. Niu, and C. Wang, Relationship between morphologies and orientations of Cu_6Sn_5 grains in Sn3. 0Ag0. 5Cu solder joints on different Cu pads. Materials Characterization, (2014). 88: 58-68.

9. J.W. Xian, S.A. Belyakov, and C.M. Gourlay, Controlling Bulk Cu_6Sn_5 Nucleation in Sn-0.7Cu/Cu Joints with Al Micro-alloying. Journal of Electronic Materials, (2016). 45: 69-78.

10. Z. Zhang, H. Cao, H. Yang, M. Li, and Y. Yu, Hexagonal-Rod Growth Mechanism and Kinetics of the Primary Cu_6Sn_5 Phase in Liquid Sn-Based Solder. Journal of Electronic Materials, (2016). 45: 5985-5995.

11. J. Xian, S. Belyakov, M. Ollivier, K. Nogita, H. Yasuda, and C. Gourlay, Cu_6Sn_5 crystal growth mechanisms during solidification of electronic interconnections. Acta Materialia, (2017). 126: 540-551.

12. S. McDonald, K. Nogita, J. Read, T. Ventura, and T. Nishimura, Influence of Composition on the Morphology of Primary Cu_6Sn_5 in Sn-4Cu Alloys. Journal of Electronic Materials, (2013). 42: 256-262.

13. J. Xian, S. Belyakov, T. Britton, and C. Gourlay, Heterogeneous nucleation of Cu_6Sn_5 in Sn–Cu–Al solders. Journal of Alloys and Compounds, (2015). 619: 345-355.

14. F. Wang, X. Ma, and Y. Qian, Improvement of microstructure and interface structure of eutectic Sn–0.7Cu solder with small amount of Zn addition. Scripta Materialia, (2005). 53: 699-702.

15. F. Cheng, H. Nishikawa, and T. Takemoto, Microstructural and mechanical properties of Sn–Ag–Cu lead-free solders with minor addition of Ni and/or Co. Journal of Materials Science, (2008). 43: 3643-3648.

16. A.E. Hammad, Investigation of microstructure and mechanical properties of novel Sn–0.5Ag–0.7Cu solders containing small amount of Ni. Materials & Design, (2013). 50: 108-116.

17. C. Yang, F. Song, and S.W. Ricky Lee, Impact of Ni concentration on the

intermetallic compound formation and brittle fracture strength of Sn–Cu–Ni (SCN) lead-free solder joints. Microelectronics Reliability, (2014). 54: 435-446.

18. B.L. Silva, N. Cheung, A. Garcia, and J.E. Spinelli, Sn–0.7wt%Cu–(xNi) alloys: Microstructure–mechanical properties correlations with solder/substrate interfacial heat transfer coefficient. Journal of Alloys and Compounds, (2015). 632: 274-285.

19. D. Swenson, The effects of suppressed beta tin nucleation on the microstructural evolution of lead-free solder joints, in *Lead-Free Electronic Solders: A Special Issue of the Journal of Materials Science: Materials in Electronics*, K.N. Subramanian, Editor. 2007, Springer US: Boston, MA. 39-54.

20. P. Zhou, H. Kang, F. Cao, Y. Fu, T. Xiao, and T. Wang, In situ study on growth behavior of Cu_6Sn_5 during solidification with an applied DC in RE-doped Sn–Cu solder alloys. Journal of Materials Science: Materials in Electronics, (2014). 25: 4538-4546.

21. A.A. El-Daly, W.M. Desoky, T.A. Elmosalami, M.G. El-Shaarawy, and A.M. Abdraboh, Microstructural modifications and properties of SiC nanoparticles-reinforced Sn–3.0Ag–0.5Cu solder alloy. Materials & Design (1980-2015), (2015). 65: 1196-1204.

22. X. Wang, Y.C. Liu, C. Wei, H.X. Gao, P. Jiang, and L.M. Yu, Strengthening mechanism of SiC-particulate reinforced Sn-3.7Ag-0.9Zn lead-free solder. Journal of Alloys and Compounds, (2009). 480: 662-665.

23. A.A. El-Daly, G.S. Al-Ganainy, A. Fawzy, and M.J. Younis, Structural characterization and creep resistance of nano-silicon carbide reinforced Sn-1.0Ag-0.5Cu lead-free solder alloy. Materials & Design, (2014). 55: 837-845.

24. L.C. Tsao, S.Y. Chang, C.I. Lee, W.H. Sun, and C.H. Huang, Effects of nano-Al_2O_3 additions on microstructure development and hardness of Sn3.5Ag0.5Cu

solder. Materials & Design, (2010). 31: 4831-4835.

25. M.A.A. Mohd Salleh, S.D. McDonald, C.M. Gourlay, H. Yasuda, and K. Nogita, Suppression of Cu_6Sn_5 in TiO_2 reinforced solder joints after multiple reflow cycles. Materials & Design, (2016). 108: 418-428.

26. L.C. Tsao, C.H. Huang, C.H. Chung, and R.S. Chen, Influence of TiO_2 nanoparticles addition on the microstructural and mechanical properties of Sn0.7Cu nano-composite solder. Materials Science and Engineering: A, (2012). 545: 194-200.

27. M.A.A.M. Salleh, C.M. Gourlay, J.W. Xian, S.A. Belyakov, H. Yasuda, S.D. McDonald, and K. Nogita, In situ imaging of microstructure formation in electronic interconnections. Scientific Reports, (2017). 7: 40010.

28. C.M. Gourlay, K. Nogita, A.K. Dahle, Y. Yamamoto, K. Uesugi, T. Nagira, M. Yoshiya, and H. Yasuda, In situ investigation of unidirectional solidification in Sn-0.7Cu and Sn-0.7Cu-0.06Ni. Acta Materialia, (2011). 59: 4043-4054.

29. H. Yasuda, I. Ohnaka, K. Kawasaki, A. Sugiyama, T. Ohmichi, J. Iwane, and K. Umetani, Direct observation of stray crystal formation in unidirectional solidification of Sn–Bi alloy by X-ray imaging. Journal of Crystal Growth, (2004). 262: 645-652.

30. T. Schenk, H. Nguyen Thi, J. Gastaldi, G. Reinhart, V. Cristiglio, N. Mangelinck-Noël, H. Klein, J. Härtwig, B. Grushko, B. Billia, and J. Baruchel, Application of synchrotron X-ray imaging to the study of directional solidification of aluminium-based alloys. Journal of Crystal Growth, (2005). 275: 201-208.

31. C. Puncreobutr, P.D. Lee, K.M. Kareh, T. Connolley, J.L. Fife, and A.B. Phillion, Influence of Fe-rich intermetallics on solidification defects in Al–Si–Cu alloys. Acta Materialia, (2014). 68: 42-51.

32. R.H. Mathiesen, L. Arnberg, F. Mo, T. Weitkamp, and A. Snigirev, Time Resolved X-Ray Imaging of Dendritic Growth in Binary Alloys. Physical Review Letters, (1999). 83: 5062-5065.

33. E. Liotti, A. Lui, R. Vincent, S. Kumar, Z. Guo, T. Connolley, I.P. Dolbnya, M. Hart, L. Arnberg, R.H. Mathiesen, and P.S. Grant, A synchrotron X-ray radiography study of dendrite fragmentation induced by a pulsed electromagnetic field in an Al–15Cu alloy. Acta Materialia, (2014). 70: 228-239.

34. K.M. Kareh, P.D. Lee, R.C. Atwood, T. Connolley, and C.M. Gourlay, Revealing the micromechanisms behind semi-solid metal deformation with time-resolved X-ray tomography. Nature Communications, (2014). 5: 7.

35. J. Fonseca, C. O'Sullivan, T. Nagira, H. Yasuda, and C.M. Gourlay, In situ study of granular micromechanics in semi-solid carbon steels. Acta Materialia, (2013). 61: 4169-4179.

36. H.L.J. Pang, K.H. Tan, X.Q. Shi, and Z.P. Wang, Microstructure and intermetallic growth effects on shear and fatigue strength of solder joints subjected to thermal cycling aging. Materials Science and Engineering: A, (2001). 307: 42-50.

37. Q. Zhang, J. Tan, and Z. Zhang, Fracture behaviors and strength of Cu_6Sn_5 intermetallic compounds by indentation testing. Journal of Applied Physics, (2011). 110: 014502.

38. J. Wang and H. Nishikawa, Impact strength of Sn–3.0Ag–0.5Cu solder bumps during isothermal aging. Microelectronics Reliability, (2014). 54: 1583-1591.

39. L. Ching-Tsung, H. Chi-Shiung, C. Tao-Chih, and L. Ming-Kann. Solder joint strengths and interfacial reactions in various Pb-free solder joints. in *2007 International Microsystems, Packaging, Assembly and Circuits Technology*.

2007.

40. S.M. Hayes, N. Chawla, and D.R. Frear, Interfacial fracture toughness of Pb-free solders. Microelectronics Reliability, (2009). 49: 269-287.

41. H.-T. Lee, M.-H. Chen, H.-M. Jao, and T.-L. Liao, Influence of interfacial intermetallic compound on fracture behavior of solder joints. Materials Science and Engineering: A, (2003). 358: 134-141.

42. Y.C. Chan, A.C.K. So, and J.K.L. Lai, Growth kinetic studies of Cu–Sn intermetallic compound and its effect on shear strength of LCCC SMT solder joints. Materials Science and Engineering: B, (1998). 55: 5-13.

43. L. Quan, D. Frear, D. Grivas, and J.W. Morris, Tensile behavior of pb-sn solder/cu joints. Journal of Electronic Materials, (1987). 16: 203-208.

44. Y.-H. Lee and H.-T. Lee, Shear strength and interfacial microstructure of Sn–Ag–xNi/Cu single shear lap solder joints. Materials Science and Engineering: A, (2007). 444: 75-83.

45. A. Hirose, H. Yanagawa, E. Ide, and K.F. Kobayashi, Joint strength and interfacial microstructure between Sn–Ag–Cu and Sn–Zn–Bi solders and Cu substrate. Science and Technology of Advanced Materials, (2004). 5: 267-276.

46. S. Ahat, M. Sheng, and L. Luo, Microstructure and shear strength evolution of SnAg/Cu surface mount solder joint during aging. Journal of Electronic Materials, (2001). 30: 1317-1322.

47. X. Li, F. Li, F. Guo, and Y. Shi, Effect of Isothermal Aging and Thermal Cycling on Interfacial IMC Growth and Fracture Behavior of SnAgCu/Cu Joints. Journal of Electronic Materials, (2011). 40: 51-61.

48. J.-W. Yoon, S.-W. Kim, and S.-B. Jung, Interfacial reaction and mechanical properties of eutectic Sn–0.7Cu/Ni BGA solder joints during isothermal long-

term aging. Journal of Alloys and Compounds, (2005). 391: 82-89.

49. K.S. Kim, S.H. Huh, and K. Suganuma, Effects of intermetallic compounds on properties of Sn–Ag–Cu lead-free soldered joints. Journal of Alloys and Compounds, (2003). 352: 226-236.

50. D. Frear, D. Grivas, and J. Morris, The effect of Cu_6Sn_5 whisker precipitates in bulk 60Sn-40Pb solder. Journal of Electronic Materials, (1987). 16: 181-186.

51. http://www.metallurgy.nist.gov/phase/solder/cusn.html.

52. H. Baker, ASM handbook: Alloy phase diagrams. 1992: ASM International.

53. S. Fürtauer, D. Li, D. Cupid, and H. Flandorfer, The Cu–Sn phase diagram, Part I: New experimental results. Intermetallics, (2013). 34: 142-147.

54. B. Peplinski, G. Schulz, D. Schultze, and E. Schierhorn. Improved X-ray powder diffraction data for the disordered η-Cu_6Sn_5 alloy phase. in *Materials Science Forum*. 1996. Trans Tech Publ.

55. A.-K. Larsson, L. Stenberg, and S. Lidin, The superstructure of domain-twinned η'-Cu_6Sn_5. Acta crystallographica. Section B, Structural science, (1994). 50: 636-643.

56. D. Mu, S. McDonald, J. Read, H. Huang, and K. Nogita, Critical properties of Cu_6Sn_5 in electronic devices: Recent progress and a review. Current Opinion in Solid State and Materials Science, (2016). 20: 55-76.

57. A. Paul, C. Ghosh, and W.J. Boettinger, Diffusion Parameters and Growth Mechanism of Phases in the Cu-Sn System. Metallurgical and Materials Transactions A, (2011). 42: 952-963.

58. G. Ghosh and M. Asta, Phase Stability, Phase Transformations, and Elastic Properties of Cu_6Sn_5: Ab initio Calculations and Experimental Results. Journal

of Materials Research, (2011). 20: 3102-3117.

59. K.-K. Wang, D. Gan, and K.-C. Hsieh, Orientation relationships, interfaces, and microstructure of η-Cu_6Sn_5 formed in the early-stage reaction between Cu and molten Sn. Thin Solid Films, (2010). 519: 1380-1386.

60. Y.Q. Wu, J.C. Barry, T. Yamamoto, Q.F. Gu, S.D. McDonald, S. Matsumura, H. Huang, and K. Nogita, A new phase in stoichiometric Cu_6Sn_5. Acta Materialia, (2012). 60: 6581-6591.

61. S. Lidin and A.-K. Larsson, A Survey of Superstructures in Intermetallic NiAs-Ni_2In-Type Phases. Journal of Solid State Chemistry, (1995). 118: 313-322.

62. S. Lidin and S.Y. Piao, The Structure of Cu_6Sn_5 - xSb_x - Large Effects of Subtle Doping. Zeitschrift für anorganische und allgemeine Chemie, (2009). 635: 611-613.

63. K. Nogita, C.M. Gourlay, and T. Nishimura, Cracking and phase stability in reaction layers between Sn-Cu-Ni solders and Cu substrates. Jom, (2009). 61: 45-51.

64. K. Nogita and T. Nishimura, Nickel-stabilized hexagonal $(Cu,Ni)_6Sn_5$ in Sn–Cu–Ni lead-free solder alloys. Scripta Materialia, (2008). 59: 191-194.

65. C.-Y. Yu and J.-G. Duh, Stabilization of hexagonal $Cu_6(Sn,Zn)_5$ by minor Zn doping of Sn-based solder joints. Scripta Materialia, (2011). 65: 783-786.

66. Y.-W. Yen, C.-C. Jao, H.-M. Hsiao, C.-Y. Lin, and C. Lee, Investigation of the Phase Equilibria of Sn-Cu-Au Ternary and Ag-Sn-Cu-Au Quaternary Systems and Interfacial Reactions in Sn-Cu/Au Couples. Journal of Electronic Materials, (2007). 36: 147-158.

67. Z.Q. Li, S.A. Belyakov, J.W. Xian, and C.M. Gourlay, The Influence of Primary Cu_6Sn_5 Size on the Shear Impact Properties of Sn-Cu/Cu BGA Joints. Journal

of Electronic Materials, (2017).

68. T.R. Bieler, Lead free solder review, in *Encyclopedia of Materials: Science and Technology*. 2010, Elsevier Ltd. 1-12.

69. Z.L. Ma, S.A. Belyakov, K. Sweatman, T. Nishimura, T. Nishimura, and C.M. Gourlay, Harnessing heterogeneous nucleation to control tin orientations in electronic interconnections. Nature Communications, (2017). 8: 10.

70. W. Kurz and D.J. Fisher, Fundamentals of solidification. 1986: Trans Tech Publications.

71. D.A. Porter, K.E. Easterling, and M. Sherif, Phase Transformations in Metals and Alloys, Third Edition (Revised Reprint). 2009: CRC Press.

72. Y. Kaygısız, Y. Ocak, S. Aksöz, N. Maraşlı, K. Keşlioğlu, E. Çadırlı, and H. Kaya, Thermal conductivity and interfacial energies of solid Sn in the Sn–Cu alloy. Chemical Physics Letters, (2010). 484: 219-224.

73. S. Metallurgical, E. Association, U.o. Sheffield, and M. Society, Solidification and casting of metals: proceedings of an international conference on solidification. 1979: Metals Society.

74. D. Turnbull, Isothermal Rate of Solidification of Small Droplets of Mercury and Tin. The Journal of Chemical Physics, (1950). 18: 768-769.

75. D. Turnbull, The Subcooling of Liquid Metals. Journal of Applied Physics, (1949). 20: 817-817.

76. Y. Waseda and W.A. Miller, Calculation of the Crystal-Melt Interfacial Free Energy from Experimental Radial Distribution Function Data. Transactions of the Japan Institute of Metals, (1978). 19: 546-552.

77. K. Mondal and B. Murty, On the prediction of solid–liquid interfacial energy of

glass forming liquids from homogeneous nucleation theory. Vol. 454. 2007. 654-661.

78. B. Vinet, L. Magnusson, H. Fredriksson, and P.J. Desré, Correlations between Surface and Interface Energies with Respect to Crystal Nucleation. Journal of Colloid and Interface Science, (2002). 255: 363-374.

79. H.M. Lu, Z. Wen, and Q. Jiang, Nucleus–liquid interfacial energy of elements. Colloids and Surfaces A: Physicochemical and Engineering Aspects, (2006). 278: 160-165.

80. F. Meydaneri, B. Saatçi, and M. Özdemir, Experimental determination of solid–liquid interfacial energy for solid Sn in the Sn–Mg system. Applied Surface Science, (2011). 257: 6518-6526.

81. I.A. Kotzé and D. Kuhlmann‐Wilsdorf, A theory of the interfacial energy between a crystal and the melt. Applied Physics Letters, (1966). 9: 96-98.

82. R.M. Digilov, Semi-empirical model for prediction of crystal–melt interfacial tension. Surface Science, (2004). 555: 68-74.

83. J.A. Dantzig and M. Rappaz, Solidification. 2009: EFPL Press.

84. B.L. Bramfitt, The effect of carbide and nitride additions on the heterogeneous nucleation behavior of liquid iron. Metallurgical Transactions, (1970). 1: 1987-1995.

85. F. Bartels, J.W. Morris, G. Dalke, and W. Gust, Intermetallic phase formation in thin solid-liquid diffusion couples. Journal of Electronic Materials, (1994). 23: 787-790.

86. H.K. Kim and K.N. Tu, Kinetic analysis of the soldering reaction between eutectic SnPb alloy and Cu accompanied by ripening. Physical Review B, (1996). 53: 16027-16034.

87. R.A. Gagliano, G. Ghosh, and M.E. Fine, Nucleation kinetics of Cu_6Sn_5 by reaction of molten tin with a copper substrate. Journal of Electronic Materials, (2002). 31: 1195-1202.

88. K.N.T. J.O. Suh, N. Tamura, Dramatic morphological change of scallop-type Cu_6Sn_5 formed on (001) single crystal copper in reaction between molten SnPb solder and Cu. Applied Physics Letters, (2007).

89. H.F. Zou, H.J. Yang, and Z.F. Zhang, Morphologies, orientation relationships and evolution of Cu_6Sn_5 grains formed between molten Sn and Cu single crystals. Acta Materialia, (2008). 56: 2649-2662.

90. M.A.A. Mohd Salleh, S.D. McDonald, H. Yasuda, A. Sugiyama, and K. Nogita, Rapid Cu_6Sn_5 growth at liquid Sn/solid Cu interfaces. Scripta Materialia, (2015). 100: 17-20.

91. M.A.A. Mohd Salleh, S.D. McDonald, C.M. Gourlay, S.A. Belyakov, H. Yasuda, and K. Nogita, Effect of Ni on the Formation and Growth of Primary Cu_6Sn_5 Intermetallics in Sn-0.7 wt.%Cu Solder Pastes on Cu Substrates During the Soldering Process. Journal of Electronic Materials, (2016). 45: 154-163.

92. J. Xian, Z. Ma, S. Belyakov, M. Ollivier, and C. Gourlay, Nucleation of tin on the Cu_6Sn_5 layer in electronic interconnections. Acta Materialia, (2017). 123: 404-415.

93. Z.L. Ma, J.W. Xian, S.A. Belyakov, and C.M. Gourlay, Nucleation and twinning in tin droplet solidification on single crystal intermetallic compounds. Acta Materialia, (2018). 150: 281-294.

94. Y. Tian, W. Liu, R. An, W. Zhang, L. Niu, and C. Wang, Effect of intermetallic compounds on fracture behaviors of Sn3. 0Ag0. 5Cu lead-free solder joints during in situ tensile test. Journal of Materials Science: Materials in Electronics, (2012). 23: 136-147.

95. C.M.Gourlay, MSE 305 Solidification Processing, Department of Materials, Imperial College London. (2012).

96. K.A. Jackson, Kinetic Processes: Crystal Growth, Diffusion, and Phase Transitions in Materials. 2010: John Wiley & Sons.

97. Thermo-Calc, TCSLD Database version 3.0, (2015).

98. H.F. Zou, H.J. Yang, and Z.F. Zhang, Coarsening mechanisms, texture evolution and size distribution of Cu_6Sn_5 between Cu and Sn-based solders. Materials Chemistry and Physics, (2011). 131: 190-198.

99. J.O. Suh, K.N. Tu, G.V. Lutsenko, and A.M. Gusak, Size distribution and morphology of Cu_6Sn_5 scallops in wetting reaction between molten solder and copper. Acta Materialia, (2008). 56: 1075-1083.

100. Q.Q. Li and Y.C. Chan, Growth kinetics of the Cu_3Sn phase and void formation of sub-micrometre solder layers in Sn-Cu binary and Cu-Sn-Cu sandwich structures. Journal of Alloys and Compounds, (2013). 567: 47-53.

101. M.S. Park and R. Arroyave, Formation and growth of intermetallic compound Cu_6Sn_5 at early stages in lead-free soldering. Journal of Electronic Materials, (2010). 39: 2574-2582.

102. R. Gagliano and M. Fine, Thickening kinetics of interfacial Cu_6Sn_5 and Cu_3Sn layers during reaction of liquid tin with solid copper. Journal of Electronic Materials, (2003). 32: 1441-1447.

103. J. Gorlich, G. Schmitz, and K.N. Tu, On the mechanism of the binary Cu/Sn solder reaction. Applied Physics Letters, (2005). 86: 3.

104. J. Gong, C. Liu, P.P. Conway, and V.V. Silberschmidt, Evolution of CuSn intermetallics between molten SnAgCu solder and Cu substrate. Acta Materialia, (2008). 56: 4291-4297.

105. R.A. Lord and A. Umantsev, Early stages of soldering reactions. Journal of Applied Physics, (2005). 98: -.

106. M. Schaefer, R.A. Fournelle, and J. Liang, Theory for intermetallic phase growth between Cu and liquid Sn-Pb solder based on grain boundary diffusion control. Journal of Electronic Materials, (1998). 27: 1167-1176.

107. L. Qu, N. Zhao, H.J. Zhao, M.L. Huang, and H.T. Ma, In situ study of the real-time growth behavior of Cu_6Sn_5 at the Sn/Cu interface during the soldering reaction. Scripta Materialia, (2014). 72-73: 43-46.

108. M. Yang, Y. Cao, S. Joo, H.T. Chen, X. Ma, and M.Y. Li, Cu_6Sn_5 precipitation during Sn-based solder/Cu joint solidification and its effects on the growth of interfacial intermetallic compounds. Journal of Alloys and Compounds, (2014). 582: 688-695.

109. Y. Yang, Y. Li, H. Lu, C. Yu, and J. Chen, Interdiffusion at the interface between Sn-based solders and Cu substrate. Microelectronics Reliability, (2013). 53: 327-333.

110. M.E. Alam, S.M.L. Nai, and M. Gupta, Effect of Amount of Cu on the Intermetallic Layer Thickness Between Sn-Cu Solders and Cu Substrates. Journal of Electronic Materials, (2009). 38: 2479-2488.

111. J.O. Suh, K.N. Tu, and N. Tamura, Preferred orientation relationship between Cu_6Sn_5 scallop-type grains and Cu substrate in reactions between molten Sn-based solders and Cu. Journal of Applied Physics, (2007). 102: 7.

112. Satyanarayan and K.N. Prabhu, Reactive wetting, evolution of interfacial and bulk IMCs and their effect on mechanical properties of eutectic Sn-Cu solder alloy. Advances in Colloid and Interface Science, (2011). 166: 87-118.

113. H.K. Kim and K.N. Tu, rate of consumption of cu in soldering accompanied by

ripening. Applied Physics Letters, (1995). 67: 2002-2004.

114. A.M. Gusak and K.N. Tu, Kinetic theory of flux-driven ripening. Physical Review B, (2002). 66: 115403.

115. M. Yang, M. Li, and C. Wang, Interfacial reactions of eutectic Sn3.5Ag and pure tin solders with Cu substrates during liquid-state soldering. Intermetallics, (2012). 25: 86-94.

116. J. Liang, N. Dariavach, P. Callahan, and D. Shangguan, Metallurgy and kinetics of liquid-solid interfacial reaction during lead-free soldering. Materials Transactions, (2006). 47: 317-325.

117. M. Schaefer, W. Laub, J.M. Sabee, and R.A. Fournelle, A numerical method for predicting intermetallic layer thickness developed during the formation of solder joints. Journal of Electronic Materials, (1996). 25: 992-1003.

118. S. Bader, W. Gust, and H. Hieber, Rapid formation of intermetallic compounds by interdiffusion in the Cu-Sn and Ni-Sn systems. Acta Metallurgica Et Materialia, (1995). 43: 329-337.

119. I.E. Anderson, J.C. Foley, B.A. Cook, J. Harringa, R.L. Terpstra, and O. Unal, Alloying effects in near-eutectic Sn-Ag-Cu solder alloys for improved microstructural stability. Journal of Electronic Materials, (2001). 30: 1050-1059.

120. J. Shen, Y.C. Liu, and H.X. Gao, Formation of bulk Cu_6Sn_5 intermetallic compounds in Sn-Cu lead-free solders during solidification. Journal of Materials Science, (2007). 42: 5375-5380.

121. K. Suganuma, S.J. Kim, and K.S. Kim, High-Temperature Lead-Free Solders: Properties and Possibilities. Jom, (2009). 61: 64-71.

122. H. Tsukamoto, T. Nishimura, S. Suenaga, and K. Nogita, Shear and tensile impact strength of lead-free solder ball grid arrays placed on Ni (P)/Au surface-

finished substrates. Materials Science and Engineering: B, (2010). 171: 162-171.

123. D. Mu, H. Huang, and K. Nogita, Anisotropic mechanical properties of Cu_6Sn_5 and $(Cu,Ni)_6Sn_5$. Materials Letters, (2012). 86: 46-49.

124. T. Ventura, S. Terzi, M. Rappaz, and A.K. Dahle, Effects of Ni additions, trace elements and solidification kinetics on microstructure formation in Sn–0.7Cu solder. Acta Materialia, (2011). 59: 4197-4206.

125. S. Chada, R.A. Fournelle, W. Laub, and D. Shangguan, Copper substrate dissolution in eutectic Sn-Ag solder and its effect on microstructure. Journal of Electronic Materials, (2000). 29: 1214-1221.

126. M. Li, Z. Zhang, and J. Kim, Polymorphic transformation mechanism of η and η′ in single crystalline Cu_6Sn_5. Applied Physics Letters, (2011). 98: 201901.

127. J.E. Spinelli and A. Garcia, Microstructural development and mechanical properties of hypereutectic Sn-Cu solder alloys. Materials Science and Engineering a-Structural Materials Properties Microstructure and Processing, (2013). 568: 195-201.

128. S.-Y. Hwang, J.-W. Lee, and Z.-H. Lee, Microstructure of a lead-free composite solder produced by an in-situ process. Journal of Electronic Materials, (2002). 31: 1304-1308.

129. M. Kuna, Finite elements in fracture mechanics. Vol. 10. 2013: Springer.

130. B. Shollock, MSE 203 fracture notes, Department of Materials, Imperial College London. (2011).

131. J. Pokluda and P. Šandera, Micromechanisms of fracture and fatigue: in a multi-scale context. 2010: Springer Science & Business Media.

132. J.J. Gilman, 'cleavage, ductility and tenacity in crystals' in Fracture in *International Conference on Atomic Mechanisms of Fracture*, B.L.Averback, Editor. 1959, Technology Press and John Wiley&Sons, Inc.: Swampscott, Massachusetts. 193.

133. T. Lindley, MSE 203 Mechanical Behaviour notes, Department of Materials, Imperial College London. (2016).

134. T.L. Anderson, Fracture mechanics: fundamentals and applications. 2017: CRC press.

135. M.-S. Pham, MSE 203 Mechanical Behaviour notes, Department of Materials, Imperial College London. (2017).

136. A.A. Griffith and M. Eng, VI. The phenomena of rupture and flow in solids. Phil. Trans. R. Soc. Lond. A, (1921). 221: 163-198.

137. G.R. Irwin, Onset of fast crack propagation in high strength steel and aluminum alloys. 1956, NAVAL RESEARCH LAB WASHINGTON DC.

138. F.M. Ashby and D.R.H. Jones, engineering materials 1 an introduction to properties applications and design. 2012.

139. L. Jiang and N. Chawla, Mechanical properties of Cu_6Sn_5 intermetallic by micropillar compression testing. Scripta Materialia, (2010). 63: 480-483.

140. J. Yu, J. Wu, L. Yu, and C. Kao. In situ observations of micromechanical behaviors of intermetallic compounds for structural applications in 3D IC micro joints. in *proceedings of the Electronic Packaging and iMAPS All Asia Conference*. 2015. IEEE.

141. J. Yu, J. Wu, L. Yu, and C. Kao. Choice of Intermetallic Compounds for Structural Applications in Near Submicron Joints. in *proceedings of the 66th Electronic Components and Technology Conference (ECTC), 2016 IEEE*. 2016.

IEEE.

142. L. Jiang, H. Jiang, and N. Chawla, The Effect of Crystallographic Orientation on the Mechanical Behavior of Cu_6Sn_5 by Micropillar Compression Testing. Journal of Electronic Materials, (2012). 41: 2083-2088.

143. D. Mu, H. Huang, S.D. McDonald, J. Read, and K. Nogita, Investigating the mechanical properties, creep and crack pattern of Cu_6Sn_5 and $(Cu,Ni)_6Sn_5$ on diverse crystal planes. Materials Science and Engineering, (2013). 566: 126-133.

144. Y. Tian, W. Liu, R. An, W. Zhang, L. Niu, and C. Wang, Effect of intermetallic compounds on fracture behaviors of Sn3.0Ag0.5Cu lead-free solder joints during in situ tensile test. Journal of Materials Science-Materials in Electronics, (2012). 23: 136-147.

145. D.W. Henderson, T. Gosselin, A. Sarkhel, S.K. Kang, W.-K. Choi, D.-Y. Shih, C. Goldsmith, and K.J. Puttlitz, Ag_3Sn plate formation in the solidification of near ternary eutectic Sn–Ag–Cu alloys. Journal of Materials Research, (2002). 17: 2775-2778.

146. I.E. Anderson, J.W. Walleser, J.L. Harringa, F. Laabs, and A. Kracher, Nucleation control and thermal aging resistance of near-eutectic Sn-Ag-Cu-X solder joints by alloy design. Journal of Electronic Materials, (2009). 38: 2770-2779.

147. J. Gong, C. Liu, P.P. Conway, and V.V. Silberschmidt, Formation of Ag_3Sn plates in SnAgCu solder bumps. Materials Science and Engineering: A, (2010). 527: 2588-2591.

148. Z. Ma and C. Gourlay, Nucleation, grain orientations, and microstructure of Sn-3Ag-0.5 Cu soldered on cobalt substrates. Journal of Alloys and Compounds, (2017). 706: 596-608.

149. M. Wang, J. Wang, H. Feng, and W. Ke, In-situ observation of fracture behavior of Sn–3.0Ag–0.5Cu lead-free solder during three-point bending tests in ESEM. Materials Science and Engineering: A, (2012). 558: 649-655.

150. K. Kim, S. Huh, and K. Suganuma, Effects of cooling speed on microstructure and tensile properties of Sn–Ag–Cu alloys. Materials Science and Engineering: A, (2002). 333: 106-114.

151. F. Ochoa, J. Williams, and N. Chawla, The effects of cooling rate on microstructure and mechanical behavior of Sn-3.5 Ag solder. JOM, (2003). 55: 56-60.

152. Z.H. Zhang, M.Y. Li, Z.Q. Liu, and S.H. Yang, Growth characteristics and formation mechanisms of Cu_6Sn_5 phase at the liquid Sn-0.7Cu/(111)Cu and liquid Sn-0.7Cu/(001)Cu joint interfaces. Acta Materialia, (2016). 104: 1-8.

153. B. Liu, Y. Tian, C. Wang, R. An, and Y. Liu, Extremely fast formation of CuSn intermetallic compounds in Cu/Sn/Cu system via a micro-resistance spot welding process. Journal of Alloys and Compounds, (2016). 687: 667-673.

154. R. Gagliano and M.E. Fine, Growth of η phase scallops and whiskers in liquid tin-solid copper reaction couples. JOM, (2001). 53: 33-38.

155. T. Wang, P. Zhou, F. Cao, H. Kang, Z. Chen, Y. Fu, T. Xiao, W. Huang, and Q. Yuan, Growth behavior of Cu_6Sn_5 in Sn–6.5 Cu solders under DC considering trace Al: In situ observation. Intermetallics, (2015). 58: 84-90.

156. A.G. Murphy, D.J. Browne, W.U. Mirihanage, and R.H. Mathiesen, Combined in situ X-ray radiographic observations and post-solidification metallographic characterisation of eutectic transformations in Al–Cu alloy systems. Acta Materialia, (2013). 61: 4559-4571.

157. D. Casari, W.U. Mirihanage, K.V. Falch, I.G. Ringdalen, J. Friis, R. Schmid-

Fetzer, D. Zhao, Y. Li, W.H. Sillekens, and R.H. Mathiesen, α-Mg primary phase formation and dendritic morphology transition in solidification of a Mg-Nd-Gd-Zn-Zr casting alloy. Acta Materialia, (2016). 116: 177-187.

158. A. Bjurenstedt, D. Casari, S. Seifeddine, R.H. Mathiesen, and A.K. Dahle, In-situ study of morphology and growth of primary α-Al(FeMnCr)Si intermetallics in an Al-Si alloy. Acta Materialia, (2017). 130: 1-9.

159. JESD22-B111 Board Level Drop Test Method of Components for Handheld Electronic Products. JULY 2013.

160. H.G. Song, J.W. Morris, and F. Hua, The creep properties of lead-free solder joints. JOM, (2002). 54: 30-32.

161. E.H. Wong, S.K.W. Seah, W.D. van Driel, J.F.J.M. Caers, N. Owens, and Y.S. Lai, Advances in the drop-impact reliability of solder joints for mobile applications. Microelectronics Reliability, (2009). 49: 139-149.

162. K. Nogita, C. Gourlay, and T. Nishimura, Cracking and phase stability in reaction layers between Sn-Cu-Ni solders and Cu substrates. JOM Journal of the Minerals, Metals and Materials Society, (2009). 61: 45-51.

163. A. Telang and T. Bieler, The orientation imaging microscopy of lead-free Sn-Ag solder joints. JOM Journal of the Minerals, Metals and Materials Society, (2005). 57: 44-49.

164. L. Lehman, Y. Xing, T. Bieler, and E. Cotts, Cyclic twin nucleation in tin-based solder alloys. Acta Materialia, (2010). 58: 3546-3556.

165. C.M. Gourlay, S.A. Belyakov, Z.L. Ma, and J.W. Xian, Nucleation and Growth of Tin in Pb-Free Solder Joints. JOM, (2015). 67: 2383-2393.

166. B. Arfaei, N. Kim, and E. Cotts, Dependence of Sn grain morphology of Sn-Ag-Cu solder on solidification temperature. Journal of Electronic Materials,

(2012). 41: 362-374.

167. Z.L. Ma, S.A. Belyakov, and C.M. Gourlay, Effects of cobalt on the nucleation and grain refinement of Sn-3Ag-0.5Cu solders. Journal of Alloys and Compounds, (2016). 682: 326-337.

168. S. Belyakov, J. Xian, K. Sweatman, T. Nishimura, T. Akaiwa, and C. Gourlay, Influence of bismuth on the solidification of Sn-0.7 Cu-0.05 Ni-xBi/Cu joints. Journal of Alloys and Compounds, (2017). 701: 321-334.

169. H. Tsukamoto, T. Nishimura, S. Suenaga, S.D. McDonald, K.W. Sweatman, and K. Nogita, The influence of solder composition on the impact strength of lead-free solder ball grid array joints. Microelectronics Reliability, (2011). 51: 657-667.

170. L.C. Tsao, Evolution of nano Ag_3Sn particle formation on Cu–Sn intermetallic compounds of Sn3.5Ag0.5Cu composite solder/Cu during soldering. Journal of Alloys and Compounds, (2011). 509: 2326-2333.

171. W. Liu, Y. Tian, C. Wang, X. Wang, and R. Liu, Morphologies and grain orientations of Cu–Sn intermetallic compounds in Sn3.0Ag0.5Cu/Cu solder joints. Materials Letters, (2012). 86: 157-160.